Selective Catalytic Reduction (SCR) Mechanistic Model Development and Application over a Cu-CHA Catalyst

by

Michelle Bendrich

A thesis submitted in partial fulfillment of the requirements for the degree of

Doctor of Philosophy

in

Chemical Engineering

Department of Chemical & Materials Engineering

University of Alberta

Abstract

Mechanistic proposals for the different selective catalytic reduction (SCR) subreactions are integrated into one surface reaction mechanism that describes the main SCR reactions (Standard SCR, Fast SCR, NO_2 SCR), transient effects due to nitrate storage, as well as the production of the side product N_2O over a copper chabazite (Cu-CHA) catalyst. The mechanism is parameterized to steady state and transient experiments, and is shown to predict the behaviour of the catalyst during a driving cycle, without any refitting of kinetic parameters.

Surprisingly, although a significant amount of inhibitive ammonium nitrate is modelled to form during low temperature Fast and NO_2 SCR steady state experiments, almost no ammonium nitrate is predicted to form during a hot and cold driving cycle, thus allowing for a higher reaction activity than predicted based on steady state data. To validate whether the minimal formation of ammonium nitrate during transient driving cycles holds true, an experimental method and simulations are applied to compare the amount of ammonium nitrate stored during steady state and transient tests over the Cu-CHA catalyst. The results demonstrate that little ammonium nitrate accumulates on the catalyst surface during multiple cold world harmonized transient cycles (WHTCs) with a high cumulated NO_2/NO_x ratio owing to the slow accumulation of ammonium nitrate and rapidly fluctuating inlet conditions.

Finally, the Cu-CHA mechanistic model, as well as an Fe-zeolite global model, are used as the SCR washcoat for an SCR and ammonia slip catalyst (ASC)

configuration, to investigate whether the ASC's ability to minimize ammonia slip can result in a more aggressive dosing strategy during a driving cycle, which can help increase the NO_x conversion. Overall, it is shown that the true value of an ASC is its ability to limit ammonia slip when an error in dosing occurs, rather than allow for a more aggressive ammonia dosing strategy to increase the overall NO_x conversion of the catalytic converter system.

Preface

Chapter 2 of this thesis has been published as: M. Bendrich, A. Scheuer, R. E. Hayes, M. Votsmeier, "Unified mechanistic model for Standard SCR, Fast SCR, and NO_2 SCR over a copper chabazite catalyst", *Applied Catalysis B: Environmental* 222 (2018) 76-87.

Chapter 3 of this thesis will be submitted to a journal as: M. Bendrich, A. Scheuer, R. E. Hayes, M. Votsmeier, "Impact of ammonium nitrate formation on SCR over a Cu-CHA catalyst."

Chapter 4 of this thesis will be submitted to a journal as: M. Bendrich, A. Scheuer, R. E. Hayes, M. Votsmeier, "Comparison of SCR and SCR + ASC performance: a simulation study." A portion of this chapter has been published in my Master's thesis, and has been included in this work for the completeness of the manuscript. The new material includes the content and discussions related to Figure 4.5, Table 4.2, and Figure 4.8 as well as the entire material found in Section 4.4.5. The Master's thesis was published as: M. Bendrich, "A Systematic Approach for Performance Comparisons of NO_x Converter Designs", University of Alberta Thesis (2014).

For all three chapters, I used the laboratory test benches and in-house catalytic converter simulation software from Umicore AG & Co. KG. All Cu-CHA experiments, kinetic model development, parameterization, analysis of results, and writing of the manuscripts were performed by myself. A. Scheuer, R. E. Hayes, and

M. Votsmeier were supervisory authors, involved in the experimental design, analysis of the results, and writing of the manuscripts.

This work was funded by the Natural Sciences and Engineering Research Council of Canada (NSERC) Collaborative Research and Development (CRD) program and Umicore AG & Co. KG.

To my family – thank you for your constant love and support.

"Only those who risk going too far can possibly find out how far one can go."

- T. S. Eliot

Acknowledgements

I am extremely grateful to have had the opportunity and support to complete my PhD at the University of Alberta with the industrial collaboration of Umicore AG & Co. KG. The past four years have been very valuable, and have not only helped further my academic knowledge, but have also helped me grow more as an individual.

This thesis would have not been possible without the continuous support of my university supervisor, Dr. Robert E. Hayes, and my supervisors at Umicore, Dr. Martin Votsmeier and Dr. Alexander Scheuer. I am extremely thankful for their guidance, enthusiasm, and insightful discussions. Additionally, I would like to thank Christof Siegl and Rebecca Schilling for their dedication to helping make the experiments presented in this work possible, as well as the many wonderful individuals I had the pleasure of working with during my studies.

Thank you to both Umicore AG & Co. KG and the Natural Sciences and Engineering Research Council of Canada's (NSERC) Collaborative Research and Development (CRD) program for funding of this work – it is greatly appreciated.

Finally, I would like to thank my family and boyfriend for always being there for me, for believing in me, and teaching me to never give up.

Table of Contents

List of Tables

List of Figures

Nomenclature

Symbols

$c_{gas,i}$	concentration of species *i* in the gas phase (mol/m^3)
c_i	concentration of species *i* (mol/m^3)
$c_{p,gas}$	specific heat capacity of the gas phase (J/kg·K)
$c_{p,s}$	specific heat capacity of the solid phase (J/kg·K)
$c_{wc,i}$	concentration of species *i* in the washcoat (mol/m^3)
$D_{eff,i}$	effective diffusivity of species *i* in a catalyst (m^2/s)
D_H	hydraulic diameter (m)
E_A	activation energy (J/mol)
ΔH_j	heat of reaction for reaction *j* (J/mol)
$k_{f,b}$	forwards (f) or backwards (b) reaction rate constant (various units)
r_j	reaction rate of reaction j (mol/m^3·s)
R	universal gas constant (8.314 J/mol·K)
t	time (s)
T	temperature (K)
T_{gas}	temperature of the gas phase (K)
T_{wc}	temperature of the gas phase of the washcoat (K)
v_{gas}	average gas velocity (m/s)
$v_{i,j}$	stoichiometric coefficient of species *i* in reaction *j* (unitless)
V	catalytic converter volume (m^3)

x	radial coordinate in cylindrical coordinate system (m)
z	axial coordinate in cylindrical coordinate system (m)

Greek Letters

α	reaction order of species (unitless) or heat transfer coefficient ($W/m^2 \cdot K$)
β_i	mass transfer coefficient of species *i* (m/s)
ε	number of active sites per reactor volume ($1/m^3$)
φ	surface area between gas and solid phase per washcoat volume (m^{-1})
σ_i	surface coverage of species *i* on copper site (unitless)
θ_i	surface coverage of species *i* on ammonia storage site (unitless)
ρ_{gas}	density of the gas phase (kg/m^3)
ρ_s	density of the solid phase (kg/m^3)

Abbreviations

AOC	Ammonia Oxidation Catalyst
ASC	Ammonia Slip Catalyst
CHA	Chabazite
CDPF	Catalyzed Diesel Particulate Filter
DOC	Diesel Oxidation Catalyst
ETC	European Transient Cycle
LNT	Lean NO_x Trap
SCR	Selective Catalytic Reduction
TPD	Temperature Programmed Desorption

TPSR Temperature Programmed Surface Reaction

WHTC World Harmonized Transient Cycle

Chapter 1 – Introduction

1.1 Exhaust aftertreatment and SCR

Since the 1970's, government-imposed emission regulations have been in place to limit the amount of harmful gases exiting automotive vehicles. While the focus was initially on restricting the carbon monoxide and hydrocarbons, this was later extended to include oxides of nitrogen and particulate matter [1]. These pollutants can all be reduced *via* after-treatment systems, e.g. catalytic converters. Regulations have also placed a significant emphasis on the reduction of carbon dioxide due to its global warming potential [2]. Since carbon dioxide cannot be destroyed using an after-treatment system, the emission of carbon dioxide is decreased *via* the use of lower carbon intensity fuels or reducing fuel consumption *via* advances in engine technology. With this regard, diesel-powered vehicles have been an attractive choice compared to gasoline vehicles owing to their higher fuel economy, allowing for a greater CO_2-reduction potential; however, they typically emit more particulate matter (PM) and oxides of nitrogen (NO_x) [3, 4].

The advancement of more efficient engines, which results in increasingly lower exhaust gas temperatures, as well as stricter government regulations, challenges the automotive industry to improve the after-treatment systems further [5]. Gasoline engines limit emissions using a three-way catalyst and now a gasoline particulate filter; however, emissions from diesel engines require a more complex mixture of technologies. An example of a catalytic converter configuration for a diesel vehicle

would first consist of a diesel oxidation catalyst (DOC) that oxidizes the hydrocarbons and carbon monoxide, which is then followed by a diesel particulate filter (DPF), and then finally either a lean NO_x trap (LNT) or a selective catalytic reduction (SCR) to reduce NO_x compounds.

The SCR catalytic converter is the most widespread technology for NO_x elimination in diesel vehicles. It uses ammonia as the reducing agent, which is generated onboard *via* the hydrolysis of urea, which occurs above 180 °C [5]. The ammonia can then react with the NO_x via one of the three main SCR reactions, which are Standard SCR (1), Fast SCR (2), and NO_2 SCR (3), with the Fast SCR reaction being the fastest of the three [5].

$$4NH_3 + 4NO + O_2 \rightarrow 4N_2 + 6H_2O \quad (1)$$

$$2NH_3 + NO + NO_2 \rightarrow 2N_2 + 3H_2O \quad (2)$$

$$4NH_3 + 3NO_2 \rightarrow 3.5\ N_2 + 6H_2O \quad (3)$$

Since the SCR catalyst can adsorb and desorb the ammonia, a sharp increase in engine load can result in an undesired amount of ammonia slip. As a result, an ammonia slip catalyst (ASC) is added as a short-zone after the SCR to eliminate any excess ammonia leaving the SCR-brick [6].

Various catalysts are used successfully for SCR. Vanadium catalysts were first selected because of their use in stationary deNO_x (reduction of NO_x) applications [7]. Cu- and Fe- (beta and ZSM-5) ion-exchanged zeolite catalysts appeared later and also exhibit excellent activity and nitrogen selectivity [8, 9]. Recently, the smaller pore-structured copper chabazite (Cu-CHA) has been focused on closely in literature.

1.2 Cu-CHA catalysts

The Cu-CHA catalyst is an attractive choice for SCR owing to its improved activity at low temperatures, hydrothermal stability, and hydrocarbon resistance. These improvements are owing to its smaller pore opening, where the largest pore opening of the Cu-CHA catalyst is 3.8 Å, compared to Cu-ZSM-5, which has a pore opening of 5.5 Å [10]. Thus, there is an improved hydrothermal stability because the dealumination product $Al(OH)_3$, with a kinetic diameter of 5.03 Å, cannot escape the zeolite easily [10]. Additionally, the Cu-CHA catalyst is less susceptible to hydrocarbon poisoning, as its larger pore opening is smaller than the kinetic diameter of the hydrocarbons (i.e., 4.5 Å for C_3H_6). Furthermore, the smaller pores have also allowed for a greater stability of ammonium nitrate, resulting in less N_2O formation [11].

To better understand these catalysts for further development, a significant amount of research is being conducted on the structure-activity relationships and reaction pathways across Cu-CHA. During wet conditions, it has been proposed that the copper ion is found just outside of the chabazite structure's 6-membered ring [10, 12, 13], with the copper being mobile under certain conditions owing to the adsorption of species such as ammonia [14, 15, 16]. Literature has shown that ammonia can be stored on the copper as $[Cu(NH_3)_4]^{2+}$ complexes, as well as on the extra framework aluminum and Brønsted acid sites [17, 18], where the Brønsted sites mainly act as ammonia storage sites, and the ammonia stored on copper participates in the SCR reaction [12].

The mechanistic steps of the various SCR reactions remain unclear. While it is generally agreed upon that the redox of copper plays a role in the Standard SCR reaction, different re-oxidation mechanisms have been proposed [19, 15, 16] and the reaction's rate limiting step has not been settled [20, 21]. The elementary steps for the Fast and NO_2 SCR reaction are also not been agreed upon, with different mechanisms published [19, 22]. More research is necessary in understanding N_2O formation during in the Standard SCR, Fast SCR, and NO_2 SCR conditions, with literature providing speculation which is limited to [23, 11].

1.3 SCR models

Modelling is a beneficial tool as it not only reduces the time and cost in the design and development of after-treatment systems [24, 5], but it also allows for the proposed mechanisms to be tested at an early stage, contributing to the discussion and importance of individual reactions and submechanisms. Examples of practical simulation studies include the influence of geometrical properties on $deNO_x$ performance [25, 6], the optimal combination of an SCR catalysts (i.e., Fe- and Cu-zeolite) for a dual architecture [26, 27], and catalyst screening with optimized ammonia dosing operating strategies during driving cycles [28].

Completing meaningful simulations requires models that describe the catalyst behaviour dependent on the stored surface species. To date, many global models have been published that capture the steady state and transient dynamics related to ammonia storage for the vanadium, Fe-, and Cu-zeolite technologies [5]. Two different Cu-CHA models have been published, both taking global approaches and

only accounting for ammonia as a surface species [26, 29]. One challenge with this approach is that the models do not capture nitrate and ammonium nitrate storage, which may lead to additional transient effects that have been observed over a Cu-zeolite catalyst [23]. This issue is particularly relevant for Cu-CHA, as ammonium nitrate is more stable compared to larger pore Cu-zeolites [11]. Thus, low temperature conditions with a large ratio and amount of NO_2/NO_x are viewed as undesirable, as these conditions allow for the inhibitive ammonium nitrate to form [29].

1.4 Thesis objectives

The objective of this thesis was to develop and fit the parameters of a kinetic model for the Cu-CHA catalyst that captures both ammonia and nitrate storage, describes the main SCR and side reactions, and predicts driving cycle behaviour. The model can then be used to investigate and understand the influence of ammonium nitrate formation during steady state and transient conditions (i.e., cold driving cycles with high NO_2/NO_x). Finally, the developed Cu-CHA model, as well as an Fe-zeolite model, was applied to investigate SCR and ASC configurations.

As a whole, the work described in this thesis demonstrates the value of including simulations during the mechanism development and after-treatment system design stages. Implementing proposed sub-mechanisms into comprehensive models at an early stage contributes to the discussion of the individual mechanisms and helps understand their role and importance in the overall reaction system during steady state and transient tests. Additionally, inclusion of simulations with optimized operating strategies in the early catalyst design and system configuration phase assists in

conducting meaningful catalyst screenings, allowing the true potential of each catalytic converter to be observed and appropriate decisions to be made.

1.5 Thesis outline

Chapter 2 presents the surface reaction mechanism that describes the main SCR reactions (Standard SCR, Fast SCR, NO_2 SCR), transient effects due to nitrate storage, as well as the production of the side product N_2O over a Cu-CHA catalyst. The kinetic parameters of the mechanism are fit to steady state and transient experiments, and the model is shown to predict the behaviour of the catalyst during a driving cycle, without any refitting of kinetic parameters. Surprisingly, although a significant amount of inhibitive ammonium nitrate is modelled to form during low temperature Fast and NO_2 SCR steady state experiments, almost no ammonium nitrate is predicted to form during the hot driving cycle, thus allowing for a higher reaction activity than predicted based on steady state data.

To validate whether the minimal formation of ammonium nitrate during transient driving cycles holds true, Chapter 3 uses an experimental method and simulations to compare the amount of ammonium nitrate stored during steady state and transient tests over the Cu-CHA catalyst. Here it is observed that the length of time that the feed conditions are held significantly influences the ammonium nitrate stored, as well as the NO_x conversion. Experimental and simulated results demonstrate that little ammonium nitrate accumulates on the catalyst surface during multiple, consecutive cold world harmonized transient cycles (WHTCs) with a high cumulated NO_2/NO_x ratio compared to low temperature, high NO_2/NO_x steady state experiments, owing to

the slow accumulation of ammonium nitrate and rapidly fluctuating inlet conditions. From a modelling and catalyst testing perspective, this shows the importance of capturing the catalyst's transient behaviour rather than only steady state conditions, since steady state is not necessarily reached during practical driving scenarios.

Finally, Chapter 4 emphasizes the importance of investigating catalyst systems (i.e., SCR and ASC) together during the design process. The simulation study mainly focuses on an Fe-zeolite catalyst for the SCR washcoat, but also includes comparisons using the Cu-CHA catalyst model presented in this work. A large portion of the publication is taken from my Master's thesis [30] and is extended to include the Cu-CHA catalyst as part of the investigation and to complete a design parameter study on the ASC SCR's washcoat loading and ASC length on the NO_x conversion of driving cycles.

1.6 References

[1] H. Klingenberg, Automobile Exhaust Emission Testing, Springer (1996).

[2] S. Solomon, D. Qin, M. Manning, Z. Chen, M. Marquis, K. B. Averyt, M. Tignor, H. L. Miller (Eds.), Climate Change 2007: The Physical Science Basis, Cambridge University Press (2007).

[3] J. L. Sullivan, R. E. Baker, R. H. Hammerle, T. E. Kennex, L. Muniz, T. J. Wallington, 2004. CO2 emission benefit of diesel (versus gasoline) powered vehicles. Environmental Science & Technology 38, 3217 – 3223.

[4] T.J. Wallington, C.K. Lambert, W.C. Ruona, Diesel vehicles and sustainable mobility in the U.S., Energy Policy 54 (2013) 47-53.

[5] I. Nova, E. Tronconi (Eds.), Urea-SCR Technology for deNOx After Treatment of Diesel Exhausts, Springer (2014).

[6] A. Scheuer, W. Hauptmann, A. Drochner, J. Gieshoff, H. Vogel, M. Votsmeier, Dual layer automotive ammonia oxidation catalysts: Experiments and computer simulation, Appl. Catal. B 111–112 (2012) 445-455.

[7] J. Jansson, Vanadia-Based Catalysts for Mobile SCR in Urea-SCR Technology for deNOx After Treatment of Diesel Exhausts, Springer (2014) 65-96.

[8] M. P. Harold, P. Metkar, Lean NOx Reduction by NH3 on Fe-Exchanged Zeolite and Layered Fe/Cu Zeolite Catalysts: Mechanisms, Kinetics, and

Transport Effects in Urea-SCR Technology for deNOx After Treatment of Diesel Exhausts, Springer (2014) 311-356.

[9] M. Colombo, I. Nova, E. Tronconi, A comparative study of the NH3-SCR reactions over a Cu-zeolite and a Fe-zeolite catalyst, Catal. Today 151 (2010) 223-230.

[10] F. Gao, J. H. Kwak, J. Szanyi, C. H. F. Peden, Current Understanding of Cu-Exchanged Chabazite Molecular Sieves for Use as Commercial Diesel Engine DeNOx Catalysts, Top. Catal. 56 (2013) 1441-1459.

[11] H.-Y. Chen, Z. Wei, M. Kollar, F. Gao, Y. Wang, J. Szanyi, C. H. F. Peden, A comparative study of N2O formation during the selective catalytic reduction of NOx with NH3 on zeolite supported Cu catalysts, J. Catal. 329 (2015) 490-498.

[12] S. A. Bates, A. A. Verma, C. Paolucci, A. A. Parekh, T. Anggara, A. Yezerets, W. F. Schneider, J. T. Miller, W. N. Delgass, F. H. Ribeiro, Identification of the active Cu site in standard selective catalytic reduction with ammonia on Cu-SSZ-13, J. Catal. 312 (2014) 87-97.

[13] J.-S. McEwen, T. Anggara, W.F. Schneider, V.F. Kispersky, J.T. Miller, W.N. Delgass, F.H. Ribeiro, Integrated operando X-ray absorption and DFT characterization of Cu-SSZ-13 exchange sites during the selective catalytic reduction of NOx with NH3, Catal. Today 184 (2012) 129-144.

[14] F. Gao, E. D. Walter, M. Kollar, Y. Wang, J. Szanyi, C. H. F. Peden, Understanding ammonia selective catalytic reduction kinetics over Cu/SSZ-13 from motion of Cu ions, J. Catal. 319 (2014) 1-14.

[15] F. Gao, D. Mei, Y. Wang, J. Szanyi, C. H. F. Peden, Selective Catalytic Reduction over Cu/SSZ-13: Linking Homo- and Heterogeneous Catalysis, J. Am. Chem. Soc. 139 (2017) 4935-4942.

[16] C. Paolucci, I. Khurana, A. Parekh, S. Li, A. J. Shih, H. Li, J. R. Di Orio, J. D. Albarracin-Caballero, A. Yezerets, J. T. Miller, W. N. Delgass, F. H. Ribeiro, W. F. Schneider, R. Gounder, Dynamic multinuclear sites formed by mobilized copper ions in NOx selective catalytic reduction, Science 357 (2017) 898-903.

[17] H. Zhu, J. H. Kwak, C. H. F. Peden, J. Szanyi, In situ DRIFTS-MS studies on the oxidation of adsorbed NH3 by NOx over a Cu-SSZ-13 zeolite, Catal. Today 205 (2013) 16–23.

[18] I. Lezcano-Gonzalez, U. Deka, B. Arstad, A. Van Yperen-De Deyne, K. Hemelsoet, M. Waroquier, V. Van Speybroeck, B. M. Weckhuysen, A. M. Beale, Determining the storage, availability, and reactivity of NH3 within Cu-Chabazite-based Ammonia Selective Catalytic Reduction systems, Phys. Chem. Chem. Phys. 16 (2014) 1639–1650.

[19] T. V. W. Janssens, H. Falsig, L. F. Lundegaard, P. N. R. Vennestrom, S. B. Rasmussen, P. G. Moses, F. Giordanino, E. Borfecchia, K. A. Lomachenko, C. Lamberti, S. Bordiga, A. Godiksen, S. Mossin, P. Beato, A Consistent Reaction

Scheme for the Selective Catalytic Reduction of Nitrogen Oxides with Ammonia, ACS Catal. 5 (2015) 2832-2845.

[20] M. P. Ruggeri, T. Selleri, M. Colombo, I. Nova, E. Tronconi, Identification of nitrites/HONO as primary products of NO oxidation over Fe-ZSM-5 and their role in the Standard SCR mechanism: A chemical trapping study, J. Catal. 311 (2014) 266-270.

[21] A. M. Beale, F. Gao, I. Lezcano-Gonzalez, C. H. F. Peden, J. Szanyi, Recent advances in automotive catalysts for NOx emission control by small-pore microporous materials, Chem. Soc. Rev. 44 (2015) 7371.

[22] M. P. Ruggeri, A. Grossale, I. Nova, E. Tronconi, H. Jirglova, Z. Sobalik, FTIR in situ mechanistic study of the NH3-NO/NO2 “Fast SCR” reaction over a commercial Fe-ZSM-5 catalyst, Cat. Today 184 (2012) 107-114.

[23] M. Colombo, I. Nova, E. Tronconi, Detailed kinetic modeling of the NH3-NO/NO2 SCR reactions over a commercial Cu-zeolite catalyst for Diesel exhausts after treatment, Catal. Today 197 (2012) 243-255.

[24] A. Güthenke, D. Chatterjee, M. Weibel, B. Krutzsch, P. Kočí, M. Marek, I. Nova, E. Tronconi, Current status of modeling lean exhaust gas aftertreatment catalysts, in: Guy B. Marin (Ed.), Advances in Chemical Engineering, Academic Press (2007) 103-283.

[25] I. Nova, D. Bounechada, R. Maestri, E. Tronconi, Influence of the Substrate Properties on the Performances of NH3-SCR Monolithic Catalysts for the

Aftertreatment of Diesel Exhaust: An Experimental and Modeling Study, Ind. Eng. Chem. Res. 50 (2011) 299-309.

[26] P. Metkar, M. P. Harold, V. Balakotaiah, Experimental and kinetic modeling study of NH3-SCR of NOx on Fe-ZSM-5, Cu-chabazite and combined Fe- and Cu-zeolite monolithic catalysts, Chem. Eng. Sci. 87 (2013) 51-66.

[27] B. Shakya, M. P. Harold, V. Balakotaiah, Simulations and optimization of combined Fe- and Cu-zeolite SCR monolith catalysts, Chem. Eng. J. 278 (2015) 374-384.

[28] B. Opitz, M. Bendrich, A. Drochner, H. Vogel, R. E. Hayes, J. F. Forbes, M. Votsmeier, Simulation study of SCR catalysts with individually adjusted ammonia dosing strategies, Chem. Eng. J. 264 (2015) 936-944.

[29] L. Olsson, K. Wijayanti, K. Leistner, A. Kumar, S. Y. Joshi, K. Kamasamudram, N. W. Currier, A. Yezerets, A multi-site kinetic model for NH3-SCR over Cu/SSZ-13, Appl. Cat. B 174-175 (2015) 212-224.

[29] Y. Zha, Cummins Sustained Low Temperature NOx Reduction, https://energy.gov/sites/prod/files/2016/06/f33/pm068_zha_2016_o_web.pdf.

[30] M. Bendrich, A Systematic Approach for Performance Comparisons of NO_x Converter Designs, University of Alberta Thesis (2014).

Chapter 2 – Unified mechanistic model for standard SCR, fast SCR, and NO_2 SCR over a copper chabazite catalyst

A version of this chapter has been published as: M. Bendrich, A. Scheuer, R. E. Hayes, M. Votsmeier, Unified mechanistic model for Standard SCR, Fast SCR, and NO_2 SCR over a copper chabazite catalyst, Appl. Catal. B 222 (2018) 76-87.

2.1 Introduction

Selective catalytic reduction (SCR) is used in the automotive industry to reduce NO_x gases. In the SCR process, ammonia, the reducing agent, is generated onboard through the hydrolysis of urea. The ratio of NO to NO_2 in the exhaust gas entering the SCR catalytic converter affects the selectivity of the main reactions, which are Standard SCR (1), Fast SCR (2), and NO_2 SCR (3) [1, 2].

$$4NH_3 + 4NO + O_2 \rightarrow 4N_2 + 6H_2O \quad (1)$$

$$2NH_3 + NO + NO_2 \rightarrow 2N_2 + 3H_2O \quad (2)$$

$$4NH_3 + 3NO_2 \rightarrow 3.5\ N_2 + 6H_2O \quad (3)$$

Side reactions such as ammonia oxidation (4) and NO oxidation/NO_2 decomposition (5) at high temperatures (i.e., > 400 °C) [3, 4], or ammonium nitrate formation at low temperatures (i.e., < 200 °C), leading to N_2O formation [5, 6], can also occur.

$$4NH_3 + 3O_2 \rightarrow 2N_2 + 6H_2O \quad (4)$$

$$NO + 0.5O_2 \leftrightarrow NO_2 \quad (5)$$

$$2NH_3 + 2NO_2 \rightarrow N_2 + N_2O + 3H_2O \quad (6)$$

Several catalysts have been used for the automotive SCR. Vanadium catalysts were first implemented because of their use in stationary deNO_x applications [7], however, Fe- and Cu-zeolite catalysts became a popular choice owing to requirements for a higher activity at low temperatures and a greater stability at higher temperatures [3]. Recently, catalysts based on copper chabazite (CHA) structures have been commercialized, which have a smaller pore-structure compared to Cu-ZSM-5 and Cu-BEA [8].

As a result, there has been a significant amount of research published on Cu-CHA catalysts, which led to the identification of possible active sites and the development of mechanisms for the different reactions [9]. The purpose of the current work is to integrate this existing knowledge into a comprehensive model that captures the different subreactions as well as transient effects due to nitrate storage.

In terms of research on the active sites, it has been proposed that Cu^{2+} is found in the CHA's 6-membered ring and at higher loadings, Cu species can be found in some form of Cu_xO_y in the 8-membered ring [10, 11, 12]. Both the copper sites and Brønsted acid sites are responsible for ammonia adsorption, but ammonia adsorbed on copper is significantly more reactive in SCR [13, 14], whereas the Brønsted sites mainly act as ammonia storage sites [11].

Various mechanistic pathways have been proposed to describe the main SCR reactions (1, 2, 3). While it was originally believed that the oxidation of NO to NO_2 (5) is the rate limiting step that connects Standard SCR (1) to Fast SCR (2) [15], evidence by Ruggeri et al. points to nitrite-like species being the linking intermediate between NO oxidation and Standard SCR over zeolites [16, 17, 18]. Kwak et al. also proposed that NO^+ and not NO_2 is an intermediate over a chabazite catalyst, and presented a catalytic cycle for Standard SCR where NO is responsible for the reduction of Cu^{2+}, and oxygen is responsible for the re-oxidation [19]. Several catalytic cycles have been proposed for Standard SCR only [20, 21, 22] or Standard and Fast SCR [23] over Cu-CHA. NO_2 SCR is not captured by these proposed cycles. Nevertheless, there have been separate mechanisms proposed to describe Fast SCR [24, 25] and NO_2 SCR [26] on Fe-zeolite catalysts.

Fewer papers have focused on the simulation of SCR over Cu-CHA catalysts. A global Cu-CHA model by Olsson et al. [27] used three active sites to predict the behaviour of ammonia adsorption, ammonia oxidation, Standard SCR to N_2, and Standard SCR to N_2O; the study focused on NH_3-NO feeds, thus no NO_2 was included. To compare Cu-CHA to Fe-ZSM-5 and combined Fe- and Cu- catalysts, Metkar et al. [28], implemented a global, single site model for Cu-CHA that could predict the steady state conversions for different NO_2/NO_x ratios. One active site was used for ammonia adsorption. The model could simulate the steady state conversions for ammonia oxidation to N_2, NO oxidation, Standard SCR to N_2, Fast SCR to N_2, NO_2 SCR to N_2, and NO_2 SCR to N_2O, with ammonium nitrate gas species as an intermediate.

The formation of nitrates and nitrites may lead to additional transient effects that are not captured in models that use ammonia as the only stored species [6]. For instance, ammonium nitrate formation leads to significant low temperature dynamics. This issue is particularly important for Cu-CHA, since owing to the smaller pore size, ammonium nitrate is more stable on Cu-CHA compared to its larger-pore counterparts (i.e., Cu-BEA) [5]. In this work, we integrated mechanistic information and pathways published in the literature to develop a surface reaction mechanism that captures the transients related to mixed NH_3-NO/NO_2 feeds for Cu-CHA. The mechanism relies on a dual site approach, where one active site is responsible for ammonia adsorption, while the other accounts for the formation of nitrites and nitrates. The kinetic parameters of the reactions were fit to steady state and transient experiments, and model Standard SCR, Fast SCR, and NO_2 SCR conditions as well as side reactions such as ammonia oxidation and ammonium nitrate formation, storage, and decomposition. In a final step, the model is used to simulate a driving cycle without refitting of the kinetic parameters. Comparison of the simulated surface species formed during the driving cycle versus steady state experiments indicates that the steady state conditions are not reached during the driving cycle, and emphasizes the importance of modelling transients rather than only steady state activity.

2.2 Methods

2.2.1 Laboratory reactor measurements

The experiments were completed with a commercial, state-of-the-art, copper chabazite catalyst with a commercial copper loading supported on a cordierite

substrate. The monolith samples had the following properties: 2.5 cm diameter, 5.1 cm length, cell density of 400 cpsi, and a wall thickness of 109 μm. The samples were aged in a flow of 10 % O_2 and 10 % H_2O with N_2 as the balance gas for 16 hours at 750 °C. Additionally, a Cu-free, zeolite catalyst sample was used. This sample had 78 % of the zeolite content of the Cu-CHA sample, and it was aged for 16 hours at 700 °C; a slightly lower aging temperature was selected to prevent damage to the zeolite structure.

The monolith sample was placed inside a quartz tube through which the feed gas of selected composition and temperature was passed. A thermocouple monitored the inlet gas temperature, which was recorded and is used throughout this paper; outlet temperatures were not recorded, however investigations on the experimental set-up show a maximum temperature difference of 4 °C. The outlet gas composition was measured by an FTIR. The tubing from the reactor to the FTIR was heated to 185 °C to avoid ammonium nitrate deposition.

Three experiment types were used: steady state, transient temperature programmed desorption (TPD), and temperature programmed surface reaction (TPSR). All experiments had 5 % H_2O and 6 % O_2, with N_2 as the balance gas, and began with a pre-treatment to ensure that no species were adsorbed on the catalyst. Likewise, the gas hourly space velocity (GHSV) for all experiments was 50,000 h^{-1} at STP, with the exception of the Fast SCR experiments being completed at 125,000 h^{-1} at STP.

For the steady state experiments, the gas of desired composition and temperature was passed over the monolith until steady state was reached, at which point the steady

state outlet composition and temperature were recorded. To capture the transient dynamics, TPD experiments were used to determine the ammonia and NO_2 adsorption/desorption properties. In this experiment, the desired species were added at a given temperature. As the species were adsorbed by the catalyst, a dead-time was first exhibited, followed by a rapid increase in the outlet concentration after the active sites have been filled. Once the outlet concentration had reached steady state, the species were no longer added to the feed, allowing for any desorption of loosely bound species. A temperature ramp followed, allowing for the desorption of the remaining species. The transient TPSR experiments were similar to the TPD experiments, only multiple species were added in various orders, to allow for a reaction between desired species.

2.2.2 Engine test bench measurements

A WHTC driving cycle was performed on an engine test bench using a Cu-CHA catalyst. The Cu-CHA monolith used at the engine test bench had the following properties: 24.1 cm diameter, 34.3 cm length, cell density of 400 cpsi, and a wall thickness of 74 μm. The catalytic converter samples were aged in 10 % O_2 and 10 % H_2O, with N_2 as the balance gas for 16 hours at 750 °C.

The engine test bench catalytic converter system consisted of a diesel oxidation catalyst (DOC), a diesel particle filter (DPF), and the SCR catalyst. There was no ammonia initially stored on the SCR catalyst. The aqueous urea solution was injected between the DPF and SCR based on an NH_3/NO_x constant dosing strategy ratio of 1.2. No urea dosing restriction was in place since the temperature of the WHTC

driving cycle, which started at an initial temperature of 200 °C rather than a cold start, was always above 180 °C. An FTIR, CLD, and oxygen sensor measured the outlet composition.

2.3 Models

2.3.1 Reactor model

The reactor model assumes that all channels, their washcoat distribution, and the inlet conditions to each channel are identical, allowing one to model a single channel. 1D mass and energy balances are solved for the species in the gas phase and washcoat, where axial advection in the gas phase, mass and heat transfer from the gas phase to washcoat, and source terms from the reactions in the washcoat are included. The position dependent mass and heat transfer coefficients are calculated *via* a Nu and Sh correlation for laminar flow [30]. Internal mass transfer in the washcoat is not explicitly accounted for, and therefore the kinetic parameters may include diffusion effects. The channel was discretized axially, and the mass and energy balances were integrated using DASSL [31]. For a detailed description of the 1D mass and energy balances used, please refer to Opitz et al. [32].

2.3.2 Kinetic model

The model incorporates mechanistic pathways proposed in literature, including the NO_2 disproportionation/oxidation mechanism [33, 29, 17], ammonium nitrate formation on both Brønsted and Cu^{2+} sites [34, 29], Standard SCR and NO oxidation mechanism *via* a nitrite route [19, 16], Fast SCR [25, 24], and NO_2 SCR [26]. No reaction is a linear combination of others, and each global SCR reaction can only be

described by one linear combination of the mechanistic equations. One exception arises with NO oxidation, which is explained later. The linear combination of the proposed reactions required to model the main global reactions are presented in the Results & Discussions section.

It is assumed that the mechanism takes place on two different active sites: a site where all adsorbed ammonia is stored (*) and a copper site (Cu^{2+}-OH/Cu^{+}) that interacts with NO_2 and NO. Although it has been proposed that ammonia adsorbs on at least both Brønsted acid and copper sites [13, 14], for simplicity, all adsorbed ammonia has been grouped and it was assumed that ammonia adsorption only occurs on one site type; nevertheless, the addition of a Temkin isotherm to describe ammonia desorption reaction equation accounts for the ammonia desorption behaviour on multiple sites [27]. Additionally, rather than distinguishing between monomeric and dimeric copper, it is assumed that the 5 % H_2O present in all experiments would cause the monomeric Cu^{2+} and dimers to form Cu^{2+}-OH [10, 17]. Finally, given that the H_2O (5 %) and O_2 (6 %) added throughout all laboratory reactor experiments was constant, the kinetic dependence of H_2O and O_2 is not always included in the rate expressions. The reaction scheme implemented is listed in Table 2.1, as well as shown as a catalytic cycle in Figure 2.1, and the reactions and their role in the mechanism are described in the Results & Discussions section.

Table 2.1 – Reaction mechanism, where k_f and k_b have a different value based on the reaction.

	Reaction	**Rate Expression**
R1	$NH_3 + * \leftrightarrow NH_3*$	$A_f \cdot c_{NH3} \cdot \theta_V - A_b \exp\left(\frac{-E(1-\gamma \cdot \theta_{NH3})}{RT}\right) \cdot \theta_{NH3}$
R2	$2NO_2 + Cu^{2+} - OH \leftrightarrow Cu^{2+} - ONO + HNO_3$	$k_f \cdot {c_{NO2}}^2 \cdot \sigma_{OH} - k_b \cdot c_{HNO3} \cdot \sigma_{ONO}$
R3	$HNO_3 + Cu^{2+} - OH \leftrightarrow Cu^{2+} - NO_3 + H_2O$	$k_f \cdot c_{HNO3} \cdot \sigma_{OH} - k_b \cdot \sigma_{NO3}$
R4	$NO_2 + Cu^{2+} - ONO \leftrightarrow Cu^{2+} - NO_3 + NO$	$k_f \cdot c_{NO2} \cdot \sigma_{ONO} - k_b \cdot c_{NO} \cdot \sigma_{NO3}$
R5	$Cu^{2+} - NO_3 + H_2O \rightarrow NO_2 + ¼O_2 + Cu^{2+} - OH$	$k_f \cdot \sigma_{NO3}$
R6	$Cu^{2+} - ONO + NH_3* \rightarrow N_2 + H_2O + Cu^{2+} - OH + *$	$k_f \cdot \sigma_{ONO} \cdot \theta_{NH3}$
R7	$Cu^{2+} - ONO + NH_3* + ½O_2 \rightarrow N_2O + H_2O + Cu^{2+} - OH + *$	$k_f \cdot \sigma_{ONO} \cdot \theta_{NH3}$
R8	$3Cu^{2+} - NO_3 + 2NH_3* \rightarrow 3Cu^{2+} - ONO + N_2 + 3H_2O + 2*$	$k_f \cdot \sigma_{NO3} \cdot \theta_{NH3}$
R9	$Cu^{2+} - NO_3 + NH_3* \leftrightarrow Cu^{2+} - NO_3[NH_3] + *$	$k_f \cdot \sigma_{NO3} \cdot \theta_{NH3} - k_b \cdot \sigma_{NO3NH3} \cdot \theta_V$
R10	$Cu^{2+} - NO_3[NH_3] \rightarrow N_2O + H_2O + Cu^{2+} - OH$	$k_f \cdot \sigma_{NO3NH3}$
R11	$Cu^{2+} - NO_3[NH_3] + * + H_2O \leftrightarrow NH_4NO_3* + Cu^{2+} - OH$	$k_f \cdot \sigma_{NO3NH3} \cdot \theta_V - k_b \cdot \theta_{NH4NO3} \cdot \sigma_{OH}$

R12	$2Cu^{2+} - OH + NO \leftrightarrow Cu^{2+} - ONO + H_2O + Cu^{+}$	$k_f \cdot c_{NO} \cdot \sigma_{OH} - k_b \cdot \sigma_{ONO} \cdot \sigma_{Cu+}$
R13	$Cu^{+} + ½H_2O + ¼O_2 \rightarrow Cu^{2+} - OH$	$k_f \cdot {c_{O2}}^{\alpha} \cdot \sigma_{Cu+}$
R14	$Cu^{2+} - ONO + ½H_2O + ¼O_2 \leftrightarrow NO_2 + Cu^{2+} - OH$	$k_f \cdot \sigma_{ONO} - k_b \cdot c_{NO2} \cdot \sigma_{OH}$
R15	$4NH_3* + 5O_2 \rightarrow 4NO + 6H_2O + 4*$	$k_f \cdot {c_{O2}}^{\alpha} \cdot \theta_{NH3}$
R16	$2NH_3* + 2O_2 \rightarrow N_2O + 3H_2O + 2*$	$k_f \cdot {c_{O2}}^{\alpha} \cdot \theta_{NH3}$
R17	$2Cu^{2+} - NO_3 + 2NH_3* \rightarrow N_2 + 2NO + 2H_2O + 2Cu^{2+} - OH + 2*$	$k_f \cdot \sigma_{ONO} \cdot \theta_{NH3}$
R18	$2NH_3* + 2NO_2 \rightarrow 2N_2 + 3H_2O + ½O_2 + 2*$	$k_f \cdot c_{NO2} \cdot \theta_{NH3}$

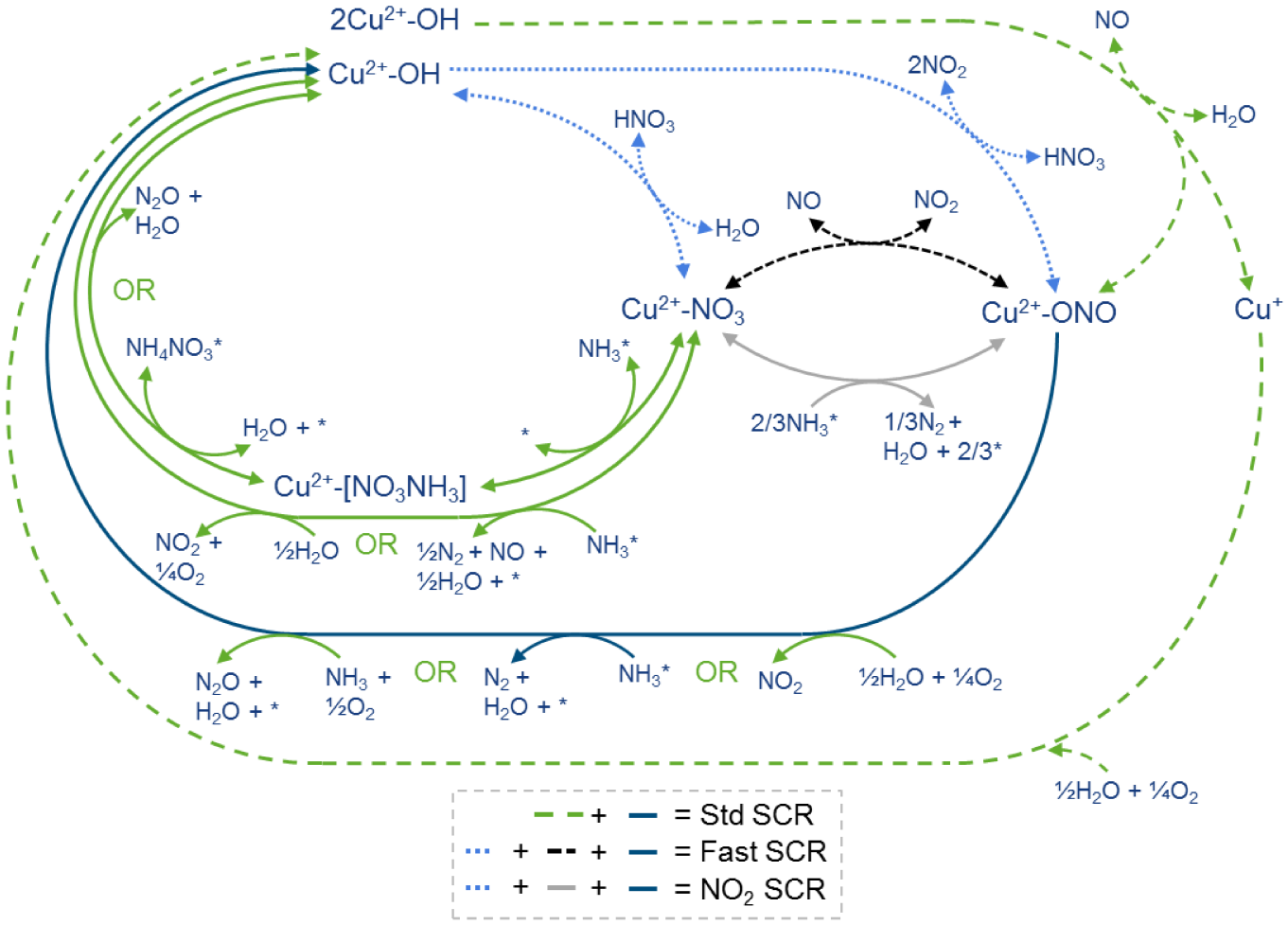

Figure 2.1 – Reaction mechanism as catalytic cycle.

The rate expressions are also included in Table 2.1, where k_f and k_b represent the forward and reverse rate constants, respectively, which take on different values based on the reaction. The variables k_f and k_b are described by the Arrhenius equation (7), where A is the pre-exponential factor, E is the activation energy, R is the gas constant and T is the temperature.

$$k = A \exp(-E/RT) \tag{7}$$

The surface coverages related to the ammonia storage site (*) include θ_V (vacant sites), θ_{NH3} (ammonia), θ_{NH4NO3} (ammonium nitrate); the surface coverages related to the copper site (Cu^{2+}/Cu^{+}) include σ_{OH} (Cu^{2+}-OH), σ_{ONO} (nitrites), σ_{NO3} (nitrates), σ_{NO3NH3} (blocking species), σ_{Cu+} (reduced copper). The sum of the surface coverages on each site equals one.

The pre-exponential factors and activation energies of each reaction were fitted to the steady state and transient experiments. The optimization algorithm used was gradient-based algorithm for a constrained, non-linear problem and the starting points were user defined.

2.4 Results & discussions

2.4.1 Adsorption of ammonia

Ammonia TPD experiments were completed to capture the ammonia adsorption-desorption dynamics. Adsorption temperatures of 150, 200, and 250 °C were used, with the results from the experiment at a constant adsorption temperature of 150 °C being shown in Figure 2.2. A feed of 500 ppm NH_3 with 5 % H_2O and 6 % O_2, with

N_2 as the balance gas was passed through the catalytic converter. Initially, ammonia was adsorbed, followed by ammonia breakthrough after the active sites have been filled to their equilibrium amount (time: 0 to 3400 s). Once steady state was reached, ammonia was discontinued in the feed, resulting in the desorption of ammonia (time: 3400 to 4400 s). Starting at 4400 s, the temperature was gradually increased (10 K/min), which resulted in the further desorption of ammonia (time: 4400 to 6600 s).

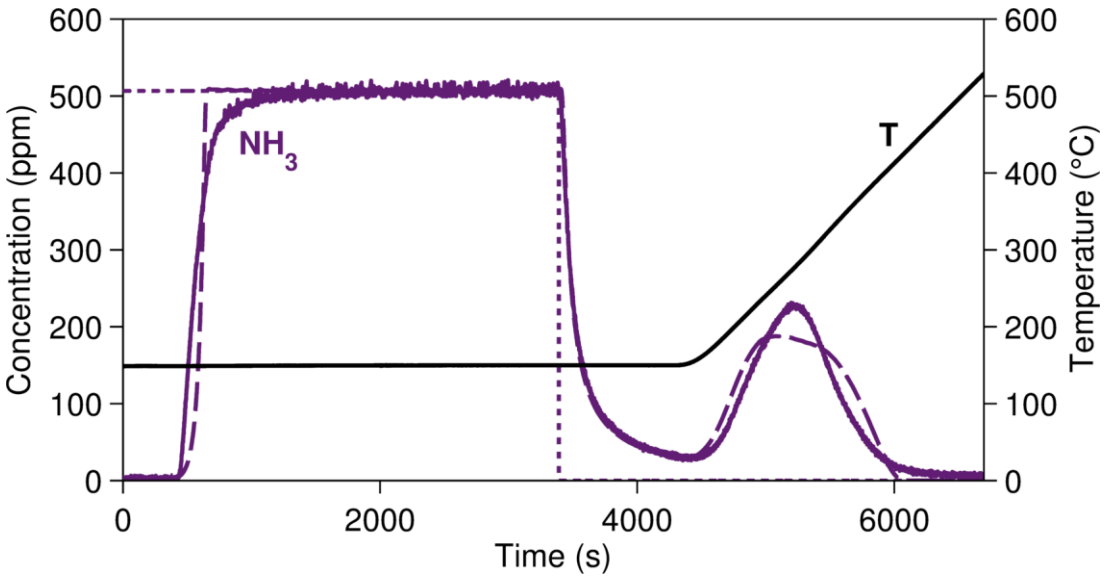

Figure 2.2 – Ammonia TPD experiment (solid line) and simulation (dashed line) with adsorption temperature of 150 °C; Feed (dotted line) = 0/500 ppm NH_3, 5 % H_2O, 6 % O_2, N_2 as Balance Gas; GHSV at STP = 50,000 h^{-1}.

For the experiments conducted at a constant adsorption temperature of 150 °C and 200 °C, all of the adsorbed ammonia was recovered during the desorption, within an error tolerance. The experimental percent difference between the amount of ammonia adsorbed and desorbed (physical desorption and during temperature ramp) was 2 % for the experiment with a constant adsorption temperature of 150 °C and 3 % at for

the experiment with a constant adsorption temperature of 200 °C. The percent difference increased at higher adsorption temperatures due to ammonia oxidation, and thus the nitrogen balance could no longer be closed at 250 °C (22 % nitrogen deficit).

The pre-exponential factor and activation energy of Equation R1r (r = reverse reaction), along with the ammonia site density, was fit using the three ammonia TPD experiments; the resulting fit is shown in Figure 2.2. The adsorption and physical desorption is well-predicted, whereas there is a slight discrepancy between the experimental and simulated ammonia desorption during the temperature ramp. The addition of a second ammonia adsorption site would help improve this fit, which has been avoided here for simplicity.

2.4.2 Formation of nitrites and nitrates *via* NO_2 adsorption

In oxidative conditions, NO_2 adsorption is understood to proceed *via* a disproportionation/oxidation mechanism [33, 29, 17]. This mechanism has been included in this model as R2 to R4, whose linear combination describes the global NO_2 adsorption equation (Table 2.2), and R5 accounting for the desorption of NO_2 at higher temperatures.

Table 2.2 – Linear reaction combination for NO_2 adsorption.

R2	$2NO_2 + Cu^{2+} - OH \leftrightarrow Cu^{2+} - ONO + HNO_3$
R3	$HNO_3 + Cu^{2+} - OH \leftrightarrow Cu^{2+} - NO_3 + H_2O$
R4	$NO_2 + Cu^{2+} - ONO \leftrightarrow Cu^{2+} - NO_3 + NO$
Sum:	$\mathbf{3NO_2 + 2Cu^{2+} - OH \leftrightarrow 2Cu^{2+} - NO_3 + NO + H_2O}$

To investigate NO_2 adsorption, NO_2 TPD experiments were completed with adsorption temperatures of 150, 200, and 250 °C. The experiments performed at 150 and 250 °C, and the simulations are shown in Figure 2.3. At the beginning of the experiment, 500 ppm NO_2 passed through the catalytic converter sample (Figure 2.3A, C). During this stage, NO_2 was adsorbed as nitrates and nitrites (R2 and R3), where nitrites were oxidized *via* NO_2 to produce NO and nitrates (R4). Thereafter, the NO_2 approached equilibrium conditions with the nitrates, NO, and HNO_3, owing to R2, R3r, and R4. Thus, the NO_2 consumption, NO produced (6 ppm at 150 °C; 3 ppm at 250 °C), and nitric acid (HNO_3) produced (9 ppm at 150 °C; 5 ppm at 250 °C) reached steady state. More nitrates were stored at lower temperatures, which also resulted in more NO and HNO_3 being produced. The nitrites acted as a steady state intermediate, where the nitrites produced were always automatically consumed. Once NO_2 had reached steady state, NO_2 was eliminated from the feed (not shown); the temperature of the feed gas was then increased, where HNO_3 and NO_2 were produced from the stored nitrates *via* R3r (r = reverse reaction) and R5 (Figure 2.3B, D). Throughout the entire experiment, 5 % H_2O, 6 % O_2, and N_2 as the balance gas was included in the feed.

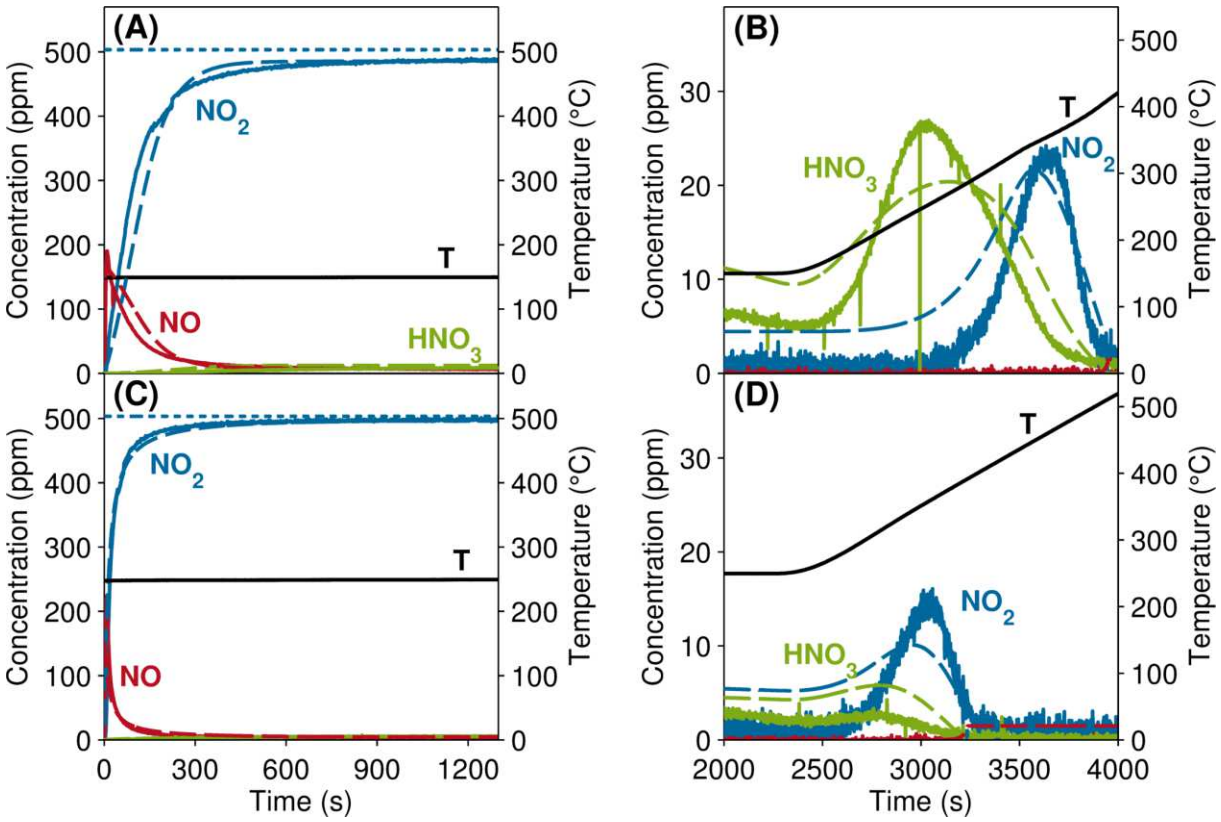

Figure 2.3 – NO_2 TPD experiment (solid lines) and simulation (dashed lines) with adsorption temperature of 150 °C (A, B) and 250 °C (C, D); Feed (dotted lines) = 0/500 ppm NO_2, 5 % H_2O, 6 % O_2, N_2 as Balance Gas; GHSV at STP = 50,000 h^{-1}.

The stoichiometry of the global NO_2 adsorption equation (Table 2.2), shows that for every three NO_2 consumed, two nitrates and one NO are produced. This ratio of NO_2 to NO was observed during the adsorption phase of all the NO_2 adsorption experiments (3.3:1 at 150 °C, 3.2:1 at 200 °C, 3.0:1 at 250 °C). Nitrogen balances were completed over the length of the three NO_2 TPD experiments, with NO_2, NO, and HNO_3 species being accounted for; HNO_3, which is rarely reported, was crucial to closing the nitrogen balance. The nitrogen balances resulted in higher errors at

lower temperatures, where more nitrogen was adsorbed than desorbed. The percent differences were 14 % at 150 °C, 6 % at 200 °C, and -3 % at 250 °C.

The Cu^{2+}-OH site density, pre-exponential factors, and activation energies of R2 to R5 were fit using the three NO_2 TPD experiments. The resulting kinetic fit shown in Figure 2.3 describes the reactions well. To validate the NO_2 adsorption kinetic fit, an NO_2 – NO TPSR experiment was completed at an adsorption temperature of 150 °C, where the experiment is shown in Figure 2.4. In this experiment, NO was added after NO_2 adsorption, where the addition of NO removes the nitrates from the catalyst surface and produces NO_2 (R4r, R3r, R2r). Thereafter, NO was eliminated from the feed, and the temperature of the feed gas was increased at a rate of 20 K/min (not shown); no NO_2, NO, or HNO_3 was detected, indicating that all nitrates had been removed from the surface during the NO addition. The kinetic model captured these effects *via* the reverse reaction shown in Table 2.2; however, the experimental ratio of NO_2 to NO was 2.2:1 rather than 3:1. This observation is similar to Grossale et al. [34], indicating that the oxidation-reduction of copper may play a role [6], which is not investigated in detail here.

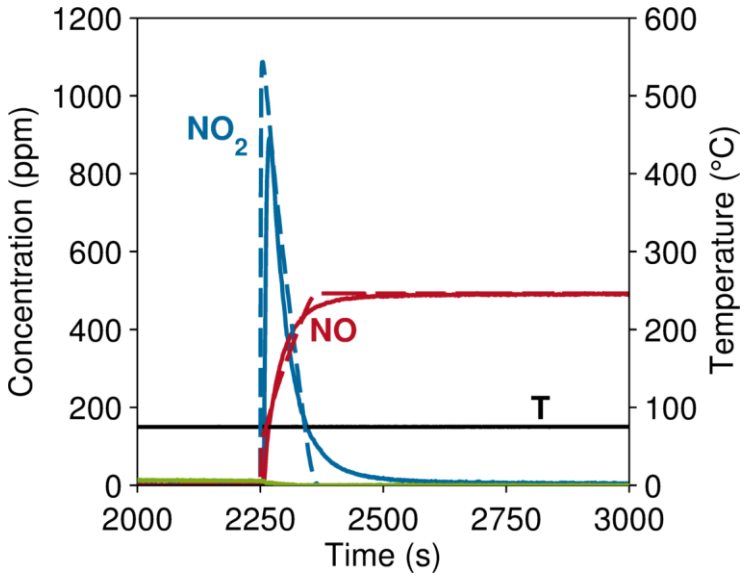

Figure 2.4 – NO_2 – NO TPSR experiment (solid lines) and simulation (dashed lines) with adsorption temperature of 150 °C; Feed (dotted lines) = 0 ppm NO_2, 500 ppm NO, 5 % H_2O, 6 % O_2, N_2 as Balance Gas; GHSV at STP = 50,000 h^{-1}. Catalyst was pretreated with 500 ppm NO_2 for 25 minutes beforehand to allow for nitrate storage.

2.4.3 NO oxidation, NO_2 decomposition, and Standard SCR *via* a nitrite pathway

The Standard SCR mechanism has yet to be agreed upon, where points of debate have been well-documented in a copper chabazite review by Beale et al. [9]. Beale et al. summarizes these points as: (1) whether SCR takes place as a redox reaction, (2) the role of ammonia stored on Brønsted acid versus copper sites, (3) the role of NO_2 in the SCR mechanism, (4) monomeric versus dimeric copper [9]. Recent literature published for Cu-CHA shows that redox of Cu^{2+}/Cu^{+} plays a role in Standard SCR [35, 21], and that ammonia stored on copper is significantly more reactive in SCR than on the Brønsted acid sites, which are responsible for ammonia storage [14, 13,

11]. Although NO_2 was initially proposed as an intermediate in Standard SCR over zeolites [15], there has been a significant amount of support showing that this is not possible. Rather, a nitrite-like species is proposed to be the intermediate [19, 18, 16]. Such a nitrite-like species has also been suggested to be the linking intermediate to NO oxidation [18, 16].

Given the evidence of Cu^{2+}/Cu^{+} cycling and the linking intermediate in SCR and NO oxidation being nitrite-like species, the main reactions implemented here for Standard SCR and NO oxidation account for these features. Likewise, although all ammonia stored in this mechanism is assumed to be on a single site, ammonia adsorption on the copper and Brønsted acid sites has been captured *via* the addition of the Temkin isotherm in the ammonia desorption rate equation (R1). No distinction has been made between the copper species (monomeric versus dimeric); however, since 5 % H_2O is always present in the feed, it is possible that monomeric Cu^{2+} would be of the form Cu^{2+}-OH [10] while the equilibrium of a copper dimer in a water feed would shift to also form Cu^{2+}-OH [17].

The implemented reactions for Standard SCR and NO oxidation are based on nitrite-pathways proposed by Ruggeri et al. and Kwak et al. [16, 19]. Although many Standard SCR mechanisms have been published as catalytic cycles with various intermediate species [23, 20, 21, 22], we opted to maintain as simple of a mechanism as possible with few intermediates, and found our current implementation simulates Standard SCR well. In this work, Standard SCR is described *via* a combination of R1,

R12, R6, and R13 (Table 2.3). The global unselective Standard SCR to N_2O can be described by replacing R6 in the mechanism above with R7.

Table 2.3 – Linear reaction combination for Standard SCR.

4*R1	$4NH_3 + 4^* \leftrightarrow 4NH_3^*$
4*R12	$8Cu^{2+} - OH + 4NO \leftrightarrow 4Cu^{2+} - ONO + 4H_2O + 4Cu^{+}$
4*R6	$4Cu^{2+} - ONO + 4NH_3^* \rightarrow 4N_2 + 4H_2O + 4Cu^{2+} - OH + 4^*$
4*R13	$4Cu^{+} + 2H_2O + O_2 \rightarrow 4Cu^{2+} - OH$
Sum:	$\mathbf{4NH_3 + 4NO + O_2 \rightarrow 4N_2 + 6H_2O}$

In Table 2.3, Reaction R12 represents the reduction of Cu^{2+} by NO, resulting in Cu^{+} and a nitrite species on Cu^{2+}. The nitrites react with ammonia to produce nitrogen and water *via* an ammonium nitrite route (R6) while the reduced Cu^{+} sites become re-oxidized *via* oxygen (R13). While recent DFT-based mechanistic proposals suggest the re-oxidation of Cu^{+} proceeds *via* both NO and O_2 [21, 23], for simplicity, Cu^{+} is modelled to only be re-oxidized using O_2 and H_2O. Since re-oxidation mechanisms were not investigated here, the re-oxidation of Cu^{+} *via* oxygen (R13) was parameterized so that it is never rate limiting, and despite this simplifying assumption, simulates the Standard SCR steady state points well. Additionally, the influence of different oxygen concentrations was not investigated in this work and a constant 6 % oxygen was used in all experiments.

NO oxidation is proposed to proceed *via* a nitrite intermediate (Table 2.4): R12, the linking reaction between NO oxidation and Standard SCR, is first responsible for the

formation of nitrites; this is followed by the oxidation of nitrites to NO_2 (R14) and the re-oxidation of Cu^+ (R13) [16].

Table 2.4 – Linear reaction combination added for NO oxidation.

R12	$2Cu^{2+} - OH + NO \leftrightarrow Cu^{2+} - ONO + H_2O + Cu^+$
R14	$Cu^{2+} - ONO + \frac{1}{2}H_2O + \frac{1}{4}O_2 \leftrightarrow NO_2 + Cu^{2+} - OH$
R13	$Cu^+ + \frac{1}{2}H_2O + \frac{1}{4}O_2 \rightarrow Cu^{2+} - OH$
Sum:	**$NO + \frac{1}{2}O_2 \rightarrow NO_2$**

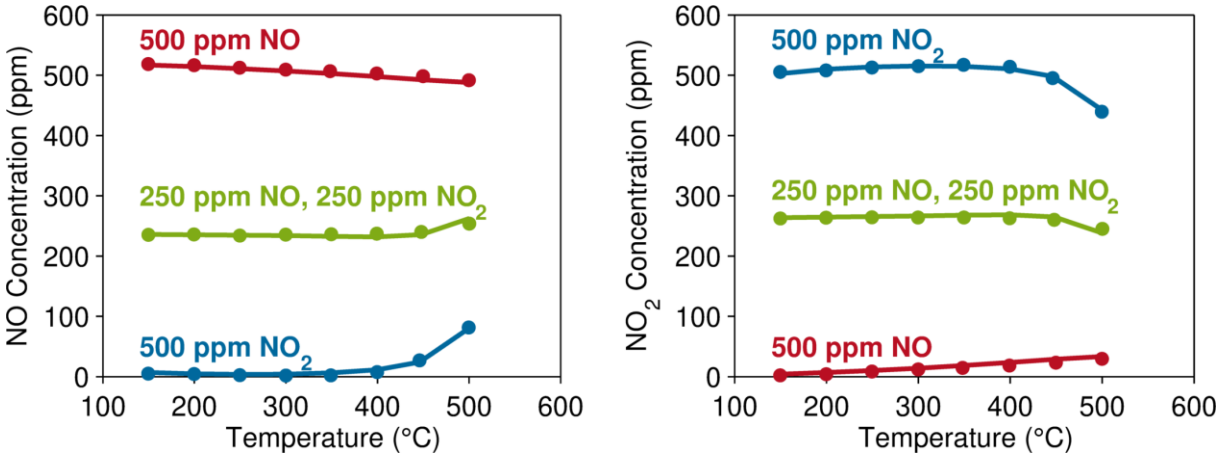

Figure 2.5 – Comparison of experimental (dots) and simulated (lines) concentrations for NO oxidation, NO_2 decomposition, and NO/NO_2 reaction studies; Feed = varying NO/NO_2, 5 % H_2O, 6 % O_2, N_2 as Balance Gas; GHSV at STP = 50,000 h^{-1}.

The pre-exponential factors and activation energies of reactions R12, R6, and R14, were fit using steady state Standard SCR and NO oxidation experiments; the experimental data and resulting kinetic fit for NO oxidation, NO_2 decomposition, and a mixed feed of NO and NO_2 are shown in Figure 2.5. Surprisingly, the reaction

mechanism in Table 2.4 was not solely responsible for the simulation of NO oxidation, where an alternative active linear combination of reactions describing NO oxidation is shown in Table 2.5. The difference between the mechanisms in Table 2.4 and Table 2.5 is how the nitrites are oxidized, where the nitrites are oxidized *via* nitrates in Table 2.5 (R2r + R3r), rather than oxygen in Table 2.4 (R14). While the mechanism in Table 2.5 was found to be dominant for NO oxidation, it required NO_2 to proceed, which is first formed *via* the NO oxidation reaction in Table 2.4.

Table 2.5 – Linear reaction combination that simulates NO oxidation.

2*R12	$4Cu^{2+} - OH + 2NO \leftrightarrow 2Cu^{2+} - ONO + 2H_2O + 2Cu^{+}$
R2r + R3r	$Cu^{2+} - ONO + Cu^{2+} - NO_3 + H_2O \leftrightarrow 2NO_2 + 2Cu^{2+} - OH$
R4	$NO_2 + Cu^{2+} - ONO \leftrightarrow Cu^{2+} - NO_3 + NO$
2*R13	$2Cu^{+} + H_2O + ½O_2 \rightarrow 2Cu^{2+} - OH$
Sum:	**$NO + ½O_2 \rightarrow NO_2$**

Since the oxidation of Cu^{+} (R13) is assumed to be irreversible, the mechanistic pathways shown in Table 2.4 and Table 2.5 do not describe NO_2 decomposition. Nevertheless, NO_2 decomposition is described by a different linear combination of reactions in Table 2.6, where copper always remains in its oxidized form (Cu^{2+}).

Table 2.6 – Linear reaction combination that simulates NO_2 decomposition.

2*R14r	$2NO_2 + 2Cu^{2+} - OH \leftrightarrow 2Cu^{2+} - ONO + H_2O + ½O_2$
R2r + R3r	$Cu^{2+} - ONO + Cu^{2+} - NO_3 + H_2O \leftrightarrow 2NO_2 + 2Cu^{2+} - OH$
R4	$NO_2 + Cu^{2+} - ONO \leftrightarrow Cu^{2+} - NO_3 + NO$
Sum:	**$NO_2 \leftrightarrow NO + ½O_2$**

Figure 2.6 shows the experimental data and resulting kinetic fit for the Standard SCR experiment, where a constant feed gas of 550 ppm NH_3, 500 ppm NO, 5 % H_2O, and 6 % O_2, with N_2 balance gas flowed through the catalytic converter sample. The catalyst allows for complete NO conversion and 90 % ammonia conversion between 250 and 300 °C; as the temperature is increased further, the ammonia conversion continues to increase while the NO conversion decreases, owing to ammonia oxidation (discussed in Section 4.4). N_2O formation increases until 225 °C, where it then starts to decrease, followed by an increase at 500 °C.

The model captures the Standard SCR light-off and ammonia oxidation above 400 °C. The N_2O formation below 400 °C is accounted by R7; however, the high temperature N_2O formation due to unselective Standard SCR to N_2O is not modelled. The addition of a second ammonia adsorption site would help capture such an increase. The reaction parameters of R6, R7, R12, and R14 were optimized to steady state NO oxidation, NO_2 decomposition, and Standard SCR data points simultaneously.

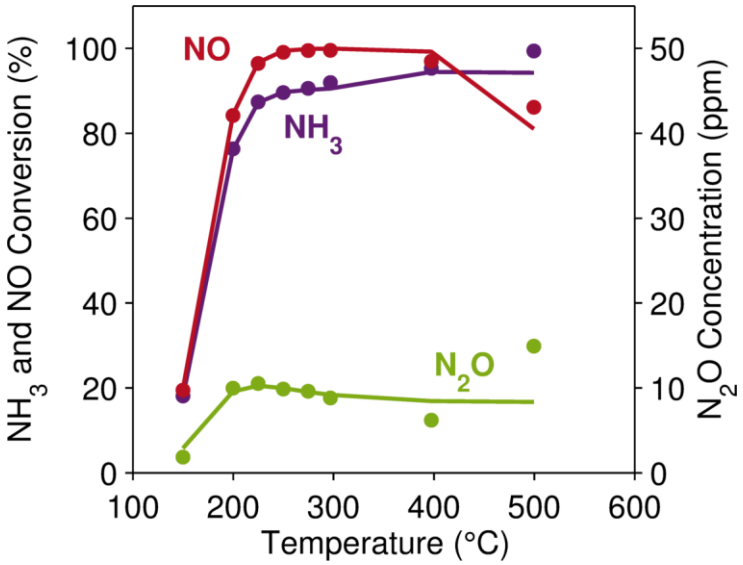

Figure 2.6 – Comparison of experimental (dots) and simulated (lines) concentrations for Standard SCR; Feed = 550 ppm NH_3, 500 ppm NO, 5 % H_2O, 6 % O_2, and N_2 balance gas; GHSV at STP = 50,000 h^{-1}.

2.4.4 Ammonia oxidation

Steady state measurements with a feed of 500 ppm NH_3 were completed to collect ammonia oxidation steady state data points. The resulting experimental points and modelling fit are shown in Figure 2.7.

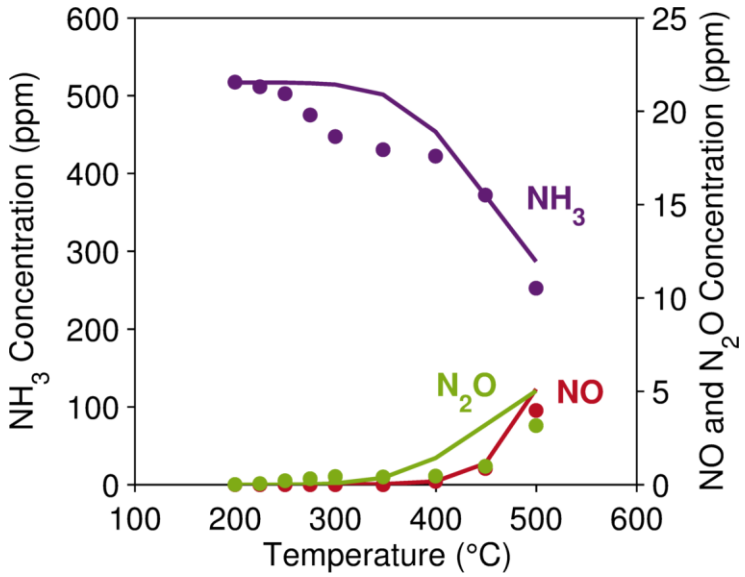

Figure 2.7 – Comparison of experimental (dots) and simulated (lines) concentrations for ammonia oxidation; Feed = 550 ppm NH_3, 5 % H_2O, 6 % O_2, and N_2 balance gas; GHSV at STP = 50,000 h^{-1}.

As seen in Figure 2.7, ammonia oxidation over the catalyst is almost completely selective to nitrogen, with only minor amounts of NO and N_2O being produced. To describe the ammonia oxidation selectivity to NO and N_2O, reactions R15 and R16 were implemented.

$$4NH_3* + 5O_2 \rightarrow 4NO + 6H_2O + 4* \quad \text{(R15)}$$

$$2NH_3* + 2O_2 \rightarrow N_2O + 3H_2O + 2* \quad \text{(R16)}$$

The need to implement a reaction for ammonia oxidation to N_2 was unnecessary, as it is already being described through the combination of Standard SCR (1) and ammonia oxidation to NO (R15). Additionally, like in the work of Olsson et al. [27] and Gao et al. [36], the chabazite catalyst displayed two regions of active ammonia oxidation. Gao et al. [36] suggests this could either be a change in rate limiting

mechanism or a change in Cu catalytic centres. Olsson et al. [27] successfully modelled this effect with two active sites. Given that only one active site is being used for ammonia storage in this work, ammonia oxidation was only fit to the higher temperature points (≥ 400 °C), resulting in ammonia oxidation not being modelled at lower temperatures (< 400 °C).

2.4.5 Fast SCR

To fit the reaction mechanism to model Fast SCR, steady state experiments were completed for these reactions. A feed of 550 ppm NH_3, 250 ppm NO, 250 ppm NO_2, 5 % H_2O, 6 % O_2, and N_2 balance gas were passed through the catalytic converter, while the temperature was held constant at the desired points until the system had reached steady state. The steady state points are shown in Figure 2.8A.

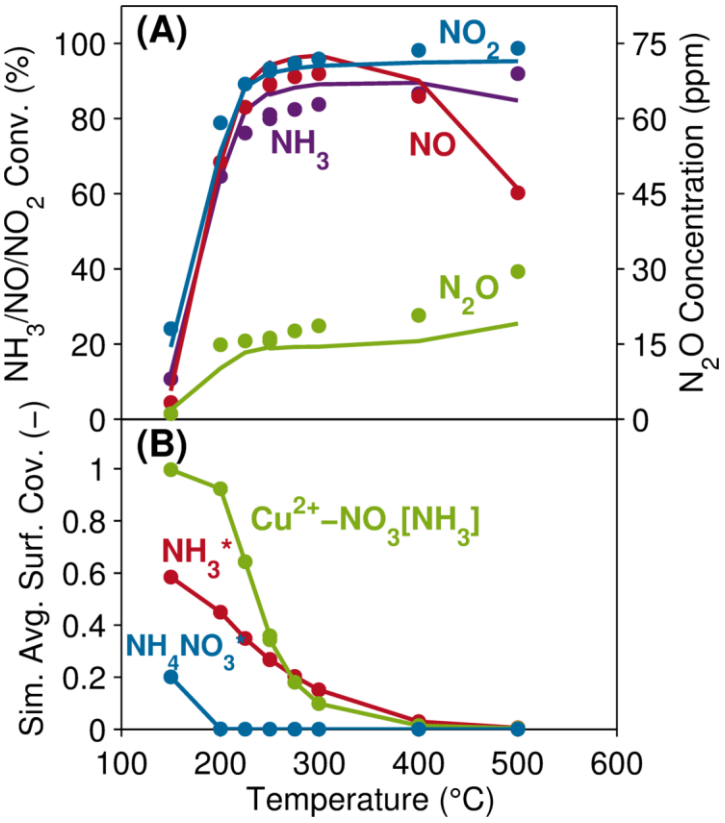

Figure 2.8 – (A) Comparison of experimental (dots) and simulated (lines) concentrations for Fast SCR; Feed = 550 ppm NH_3, 250 ppm NO, 250 ppm NO_2, 5 % H_2O, 6 % O_2, and N_2 balance gas; GHSV at STP = 125,000 h^{-1}. (B) Simulated average surface coverage of species.

In this work, Fast SCR is modelled using the mechanism proposed by Grossale et al. [24, 25, 6]; according to the mechanism, the active centre (i.e., Fe^{3+} or Cu^{2+}) does not change oxidation state. This agrees with the work of McEwan et al. [35], who concluded that only Cu^{2+} is present under Fast and NO_2 SCR conditions. Fast SCR mechanisms have been proposed where the active centre changes oxidation state [23, 37], but were not tested in this work. The global Fast SCR mechanism is implemented *via* the linear combination of reactions in Table 2.7.

Table 2.7 – Linear reaction combination for Fast SCR.

2*R1	$2NH_3 + 2^* \leftrightarrow 2NH_3^*$
R2+R3	$2NO_2 + 2Cu^{2+} - OH \leftrightarrow Cu^{2+} - ONO + Cu^{2+} - NO_3 + H_2O$
R4r	$Cu^{2+} - NO_3 + NO \leftrightarrow NO_2 + Cu^{2+} - ONO$
2*R6	$2Cu^{2+} - ONO + 2NH_3^* \rightarrow 2N_2 + 2H_2O + 2Cu^{2+} - OH + 2^*$
Sum:	$\mathbf{2NH_3 + NO + NO_2 \rightarrow 2N_2 + 3H_2O}$

Since the kinetic parameters of these equations have already been fit to the NO_2 adsorption and Standard SCR experiments, they were applied directly to simulate the steady state Fast SCR data. However, applying the above mechanism directly with the aforementioned tuned parameters initially resulted in the Fast SCR activity being too high at 150 °C and 200 °C (not shown here), despite R4r being the rate limiting step, indicating that another reaction or effect must be hindering the mechanism. Research by Grossale et al. [34] found that the addition of ammonia at low temperatures hinders nitrates from reacting with NO *via* R4r, and explained the decrease of Fast SCR activity through "ammonia blocking" species, which represent the strong interaction between adsorbed nitrates and ammonia at low temperatures. This effect was later included in a model for NO_2 SCR related chemistry by Colombo et al. [6] as Cu^{2+}-$NO_3[NH_3]$ species, and was partially responsible for N_2O formation, along with ammonium nitrate.

Inclusion of Cu^{2+}-$NO_3[NH_3]$ species in our mechanism *via* R9 allows for the simulation of the experimental activity at 150 and 200 °C, and is also responsible for the N_2O formation during Fast SCR (R10) shown in Figure 2.8A. The simulation

predicts the experimental steady state conversions well, however, the NH_3 and NO conversions are overpredicted between 225 and 300 °C during Fast SCR, because R12 (for Standard SCR) is too active. Figure 2.8B shows the simulated average surface coverage of the Cu^{2+}-$NO_3[NH_3]$, NH_3*, and NH_4NO_3* species. The NH_4NO_3* species formation, resulting from a Cu^{2+}-$NO_3[NH_3]$ spill-over effect on ammonia storage sites (*) *via* R11, will be described in detail in Section 4.7.

2.4.6 NO_2 SCR over Cu-free Chabazite

Interestingly, during the model development process, it was observed that the zeolite itself, and not copper, is mainly responsible for the low temperature (T < 250 °C) NO_2 SCR steady state conversion over Cu-CHA. This conclusion was drawn based on the comparison of NO_2 SCR steady state experiments over a Cu-free CHA (Figure 2.9) catalyst versus a Cu-CHA catalyst (Figure 2.12A), where the Cu-free CHA had 78 % of the zeolite content of the Cu-CHA catalyst, and was aged at a slightly different temperature. The catalysts showed a similar conversion below 250 °C, while Cu-CHA was more active than Cu-free CHA above 250 °C, indicating that the copper played an active role in the steady state NO_2 SCR conversion at higher temperatures.

The reason for the low temperature activity over Cu-free CHA could be owing to a reaction between adsorbed NO_2 and NH_3. Our NO_2 adsorption experiments over Cu-free CHA (not shown) indicated that NO_2 is adsorbed by the zeolite, which has also been observed over Cu-free ZSM-5 [Ols2008], and is supported by the possible formation of NO^+ on zeolites [38, 39]. However, as the detailed investigation of reaction mechanisms on the zeolite is out of the scope of this work, R18 was added as

a global reaction to describe the high conversion of ammonia and NO_2 to N_2 at low temperatures.

$$2NH_3* + 2NO_2 \rightarrow 2N_2 + 3H_2O + \tfrac{1}{2}O_2 + 2* \quad \text{(R18)}$$

Reaction R18 was fit to the transient experiments shown in Section 4.7. However, the importance of this reaction is already seen during Fast SCR experiments (Figure 2.8), where R18 ensures that the NH_3 and NO_2 conversion is captured, although the copper sites are completely blocked with Cu^{2+}-$NO_3[NH_3]$.

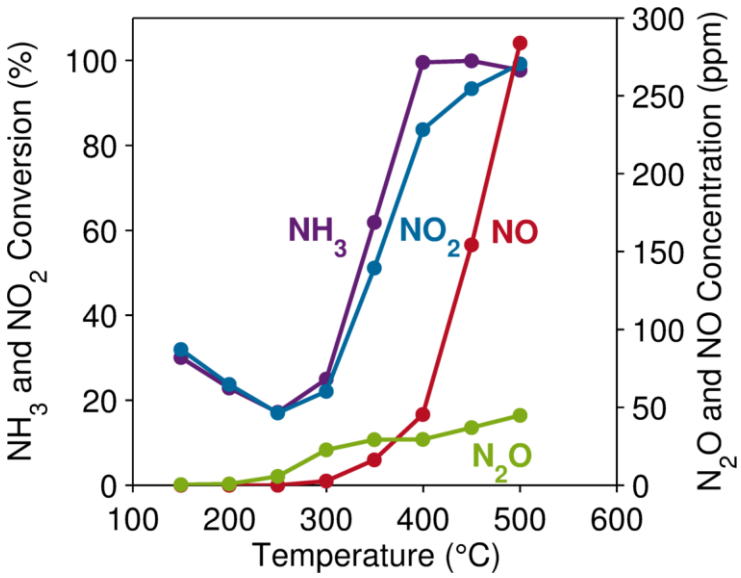

Figure 2.9 – Experimental concentrations for NO_2 SCR over Cu-free chabazite (78 % of the zeolite of Cu-CHA, aged 50 °C lower than Cu-CHA); Feed = 550 ppm NH_3, 500 ppm NO_2, 5 % H_2O, 6 % O_2, and N_2 balance gas; GHSV at STP = 50,000 h^{-1}.

Finally, it is important to note that, throughout all experiments shown in this work, the tubing from the reactor to the FTIR was heated to prevent ammonium nitrate deposition in the tubes. When adding ammonia and NO_2 at a constant temperature of

150 °C with an empty reactor, an approximate 3-4 % constant steady state conversion is seen (not shown), indicating that the NH_3 and NO_2 experimental conversion with a reactor may be minimally overpredicted at this temperature.

2.4.7 NO_2 SCR over Cu-CHA

The NO_2 SCR reaction mechanism was investigated *via* both transient temperature programmed surface reaction (TPSR) and stationary experiments. The TPSR experiments were completed at 150 and 200 °C, where the experimental and simulated results, along with simulated surface coverages, are shown in Figure 2.10 and Figure 2.11. In these experiments, NO_2 SCR conditions (500 ppm NH_3 and 500 ppm NO_2) were first passed through the catalytic converter at a fixed adsorption temperature, to investigate transients that occur when NH_3 and NO_2 are added simultaneously at low temperatures. The significant transients seen during the ammonia and NO_2 addition can be explained as follows:

1. NO_2 storage and breakthrough (Figure 2.10, 0 to 200 s): Initially, NO_2 is consumed and stored in the form of nitrates (Cu^{2+}-NO_3), leading to NO production, owing to the NO_2 adsorption dynamics (R2-R4, Section 4.2). The NO_2 breakthrough increases and NO production decreases because the NO_2 and nitrates reach an equilibrium.
2. Consumption of NO_2 owing to availability of stored ammonia (Figure 2.10, 200 to 800 s): Once the stored ammonia becomes available, it reacts with the nitrites and nitrates formed *via* NO_2 adsorption, resulting in a decrease in the NO_2 outlet concentration. The reaction between ammonia and nitrates allows

for the formation of Cu^{2+}-$NO_3[NH_3]$ (R9), which allows for the subsequent formation of NH_4NO_3* discussed momentarily (R11), while the reaction between ammonia and nitrites (R6) causes a peak in nitrogen production.

3. Breakthrough of NO_2 and NH_3 (Figure 2.10, 800 to 6800 s): As the surface species NH_4NO_3* slowly approaches steady state, the consumption of the Cu^{2+}-$NO_3[NH_3]$ intermediate decreases (R11), resulting in less ammonia and NO_2 consumption. Therefore, the outlet concentration of ammonia and NO_2 increases and slowly reaches steady state. Despite the complete blocking of the copper sites with Cu^{2+}-$NO_3[NH_3]$, a constant conversion of ammonia and NO_2 is seen during steady state conditions owing to the reaction between ammonia and NO_2 taking place on the ammonia adsorption sites (R18, Section 4.6).

From a modelling perspective, we have already added the reactions responsible for describing the NO_2 adsorption dynamics required for Step #1, along with the reactions occurring between ammonia and nitrates to build Cu^{2+}-$NO_3[NH_3]$ (R9) and ammonia and nitrites to produce nitrogen (R6) for Step #2. However, if no further reactions were to be implemented, and Cu^{2+}-$NO_3[NH_3]$ were the only inhibiting species formed *via* R9 in Step #2, all copper sites would be blocked with Cu^{2+}-$NO_3[NH_3]$ too quickly ($\sigma_{NO3NH3} = 1$). As a result, ammonia and NO_2 would break through immediately, because no more NO_2 could adsorb on the copper *via* nitrates and nitrates (R2/R3), and react with the stored ammonia (R9/R11). Thus, the slow, transient breakthrough of NO_2 and ammonia in Step #3 would not be modelled. To avoid this and capture the slow dynamics of ammonia and NO_2 at low temperatures,

an ammonium nitrate spill-over effect was included as R11; during this reaction, the ammonium nitrate-like species formed on the copper site can be adsorbed on the ammonia storage site as ammonium nitrate (NH_4NO_3*), freeing a copper site for further reaction.

$$Cu^{2+} - NO_3[NH_3] + * + H_2O \leftrightarrow NH_4NO_3* + Cu^{2+} - OH \quad \text{(R11)}$$

Interestingly, it does not appear that the Cu^{2+}-$NO_3[NH_3]$ and NH_4NO_3* species play a significant inhibitive role during a transient driving cycle. The simulation of an 1800 s WHTC driving cycle with a high NO_2/NO_x ratio in Section 4.8 will show that only a maximum predicted 6 % Cu^{2+}-$NO_3[NH_3]$ species, and no NH_4NO_3* species, are formed on the catalyst surface. From a modelling perspective, this indicates the importance of capturing the dynamics at the beginning of the TPSR experiments (i.e., Steps #1, 2), compared to the steady state conditions at the end (Step #3).

It is well-known that the addition of NO allows for ammonium nitrate decomposition [5, 29, 34]. To investigate this effect, and see whether it is described by our model, ammonia and NO_2 was eliminated from the feed in the experiments shown in Figures 2.10 and Figure 2.11, while 500 ppm NO was added to allow for ammonium nitrate decomposition. The addition of NO allowed for minimal decomposition of Cu^{2+}-$NO_3[NH_3]$ (R9) and NH_4NO_3* (R11) at 150 °C (Figure 2.10, 6800 to 8000 s), while all ammonium nitrate-likes species decomposed through the NO addition at 200 °C (Figure 2.11, 5500 to 6500 s), in line with observations over a Cu-zeolite [29] and Fe-zeolite catalyst [34]. Thereafter, NO was removed from the feed and was followed by a 10 K/min temperature ramp, which was completed to verify whether any species

remained on the catalyst surface (Figure 2.10, 8000 to 10,000 s). Species desorbed during the TPSR at 150 °C, owing to Cu^{2+}-$NO_3[NH_3]$, NH_4NO_3*, and ammonia storage, whereas no surface species were left to desorb during the 200 °C experiment.

The decomposition of Cu^{2+}-$NO_3[NH_3]$ and NH_4NO_3* through the addition of NO to the feed is modelled well, without the need of any additional reactions added to the mechanism. The decomposition reaction has been proposed to proceed *via* the global reaction shown in Table 2.8 [5], and is modelled by a linear combination of our mechanistic reactions. This mechanism largely reflects the mechanism proposed in reference [29], apart from the "spill-over" reaction (R11) used to capture the inhibiting formation of ammonium nitrate on the ammonia adsorption sites.

Table 2.8 – Linear reaction combination for decomposition of NH_4NO_3 *via* NO.

R11r	NH_4NO_3* + Cu^{2+} – OH ←→ Cu^{2+} – $NO_3[NH_3]$ + * + H_2O
R9r	Cu^{2+} – $NO_3[NH_3]$ + * ←→ Cu^{2+} – NO_3 + NH_3*
R4r	Cu^{2+} – NO_3 + NO ←→ NO_2 + Cu^{2+} – ONO
R6	Cu^{2+} – ONO + NH_3* → N_2 + H_2O + Cu^{2+} – OH + *
Sum:	**NH_4NO_3* + NO → NO_2 + N_2 + 2H_2O + ***

Following an adsorption temperature of 150 °C (Figure 2.10), the amount of the species desorbed during the TPD is simulated to be too high, despite the correct qualitative trends, indicating that too much ammonium nitrate is predicted to be stored. Both the experiments and simulation did not have any species available to desorb during the TPD following an adsorption temperature of 200 °C.

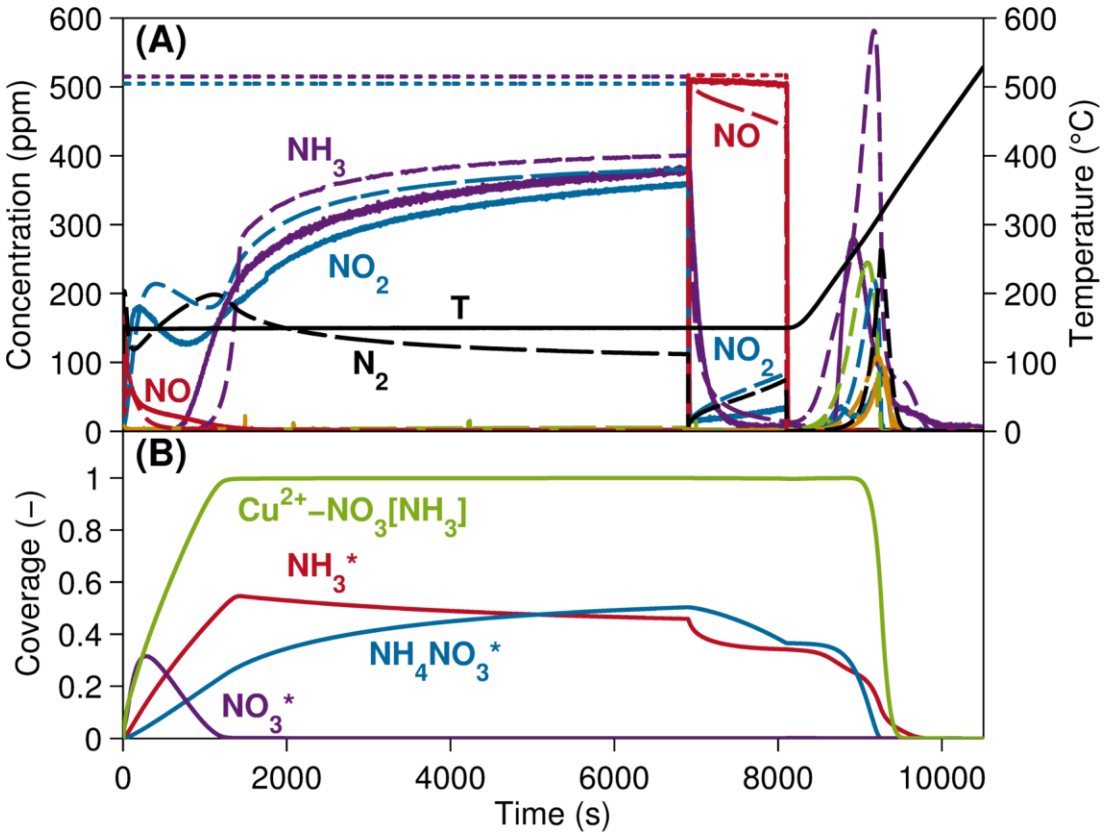

Figure 2.10 – (A) Comparison of experimental (solid lines) and simulated (dashed lines) concentrations for NH_3 + NO_2 then NO during constant adsorption temperature of 150 °C; Feed (dotted lines) = 500 ppm NH_3 and NO_2, followed by 500 ppm NO. 5 % H_2O, 6 % O_2, and N_2 balance gas always present in feed; GHSV at STP = 50,000 h^{-1}. (B) Simulated average surface coverage of species.

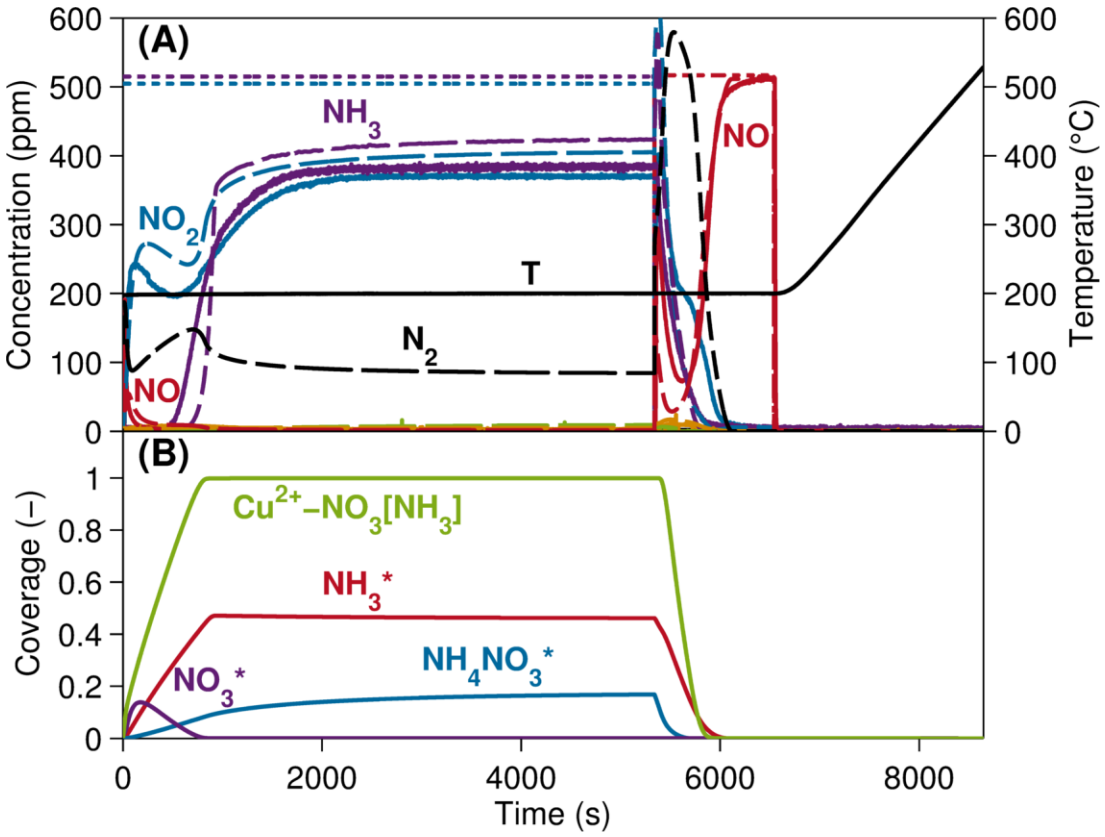

Figure 2.11 – (A) Comparison of experimental (solid lines) and simulated (dashed lines) concentrations for NH_3 + NO_2 then NO during constant adsorption temperature of 200 °C; Feed (dotted lines) = 500 ppm NH_3 and NO_2, followed by 500 ppm NO. 5 % H_2O, 6 % O_2, and N_2 balance gas always present in feed; GHSV at STP = 50,000 h^{-1}. (B) Simulated average surface coverage of species.

For the stationary NO_2 SCR experiments, 550 ppm NH_3 and 500 ppm NO_2 were passed through the monolith, with the experimental results and simulated fit appearing in Figure 2.12A. In this experiment, the presented mechanism thus far would already predict the low temperature NH_3 and NO_2 conversions (< 250 °C), owing to the addition of R18 taking place on the zeolite, along with the N_2O formation due to Cu^{2+}-$NO_3[NH_3]$ species decomposition (R10). However, the reaction mechanism presented until now would incorrectly predict the light-off curve,

as a reaction between nitrates and ammonia, leading to nitrogen formation, needs to be added to describe the main NO_2 SCR reaction. Therefore, R8 was added, allowing us to model NO_2 SCR according to a mechanism proposed by Grossale et al. that is presented in Table 2.9 [26, 6]. Additionally, since a significant amount of NO forms at high temperatures, an unselective NO_2 SCR to NO reaction has also been added and its linear combination is shown in Table 2.10.

Table 2.9 – Linear reaction combination for NO_2 SCR.

8*R1	$8NH_3 + 8^* \leftrightarrow 8NH_3^*$
3*(R2+R3)	$6NO_2 + 6Cu^{2+} - OH \leftrightarrow 3Cu^{2+} - ONO + 3Cu^{2+} - NO_3 + 3H_2O$
6*R6	$6Cu^{2+} - ONO + 6NH_3^* \rightarrow 6N_2 + 6H_2O + 6Cu^{2+} - OH + 6^*$
R8	$3Cu^{2+} - NO_3 + 2NH_3^* \rightarrow 3Cu^{2+} - ONO + N_2 + 3H_2O + 2^*$
Sum:	$\mathbf{8NH_3 + 6NO_2 \rightarrow 7N_2 + 12H_2O}$

Table 2.10 – Linear reaction combination for NO_2 SCR to NO.

2*R1	$2NH_3 + 2^* \leftrightarrow 2NH_3^*$
R2+R3	$2NO_2 + 2Cu^{2+} - OH \leftrightarrow Cu^{2+} - ONO + Cu^{2+} - NO_3 + H_2O$
R4	$NO_2 + Cu^{2+} - ONO \leftrightarrow Cu^{2+} - NO_3 + NO$
R17	$2Cu^{2+} - NO_3 + 2NH_3^* \rightarrow N_2 + 2NO + 2H_2O + 2Cu^{2+} - OH + 2^*$
Sum:	$\mathbf{2NH_3 + 3NO_2 \rightarrow N_2 + 3NO + 3H_2O}$

Reactions R8, R9, R10, and R17 were fit to both the Fast SCR and NO_2 SCR experiments simultaneously. The NO_2 SCR fit (Figure 2.12) is excellent, with the

exception that the NO produced at 500 °C during NO_2 SCR is underpredicted. Increasing the activity of NO_2 SCR to NO *via* R17 with the current parameter set causes over-production of NO at 500 °C during Fast SCR.

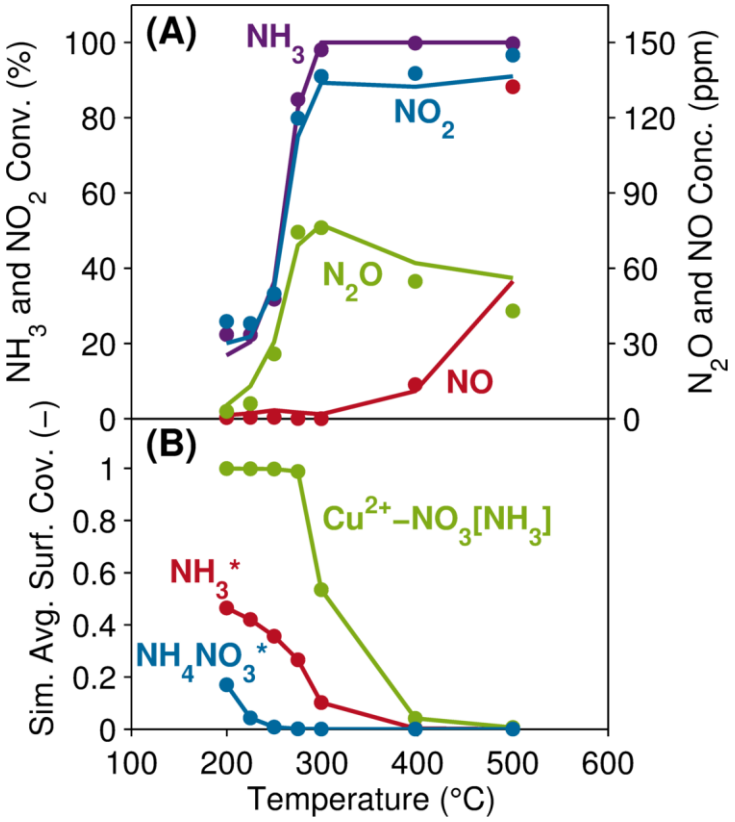

Figure 2.12 – (A) Comparison of experimental (dots) and simulated (lines) concentrations for NO_2 SCR; Feed = 550 ppm NH_3, 500 ppm NO_2, 5 % H_2O, 6 % O_2, and N_2 balance gas; GHSV at STP = 50,000 h^{-1}. (B) Simulated average surface coverage of species.

2.4.8 Predictive simulation of driving cycle

In a final step, we applied the kinetic model to a driving cycle without refitting of parameters, verified its performance, and looked at the simulated surface species formed. A WHTC driving cycle with a high NO_2/NO_x ratio, i.e. a high rate of NO_2

formation in the DOC, was selected since it had the potential for a greater ammonium nitrate formation and activity inhibition. No ammonia was initially stored on the catalyst and, rather than a cold start, the initial temperature of the WHTC driving cycle was 200 °C. The inlet conditions, along with the experimental and simulated output for NO_x and N_2O are shown in Figure 2.13. The simulation of the driving cycle using the presented mechanistic model allowed for the prediction of the NO, NO_2, and N_2O cumulated emissions.

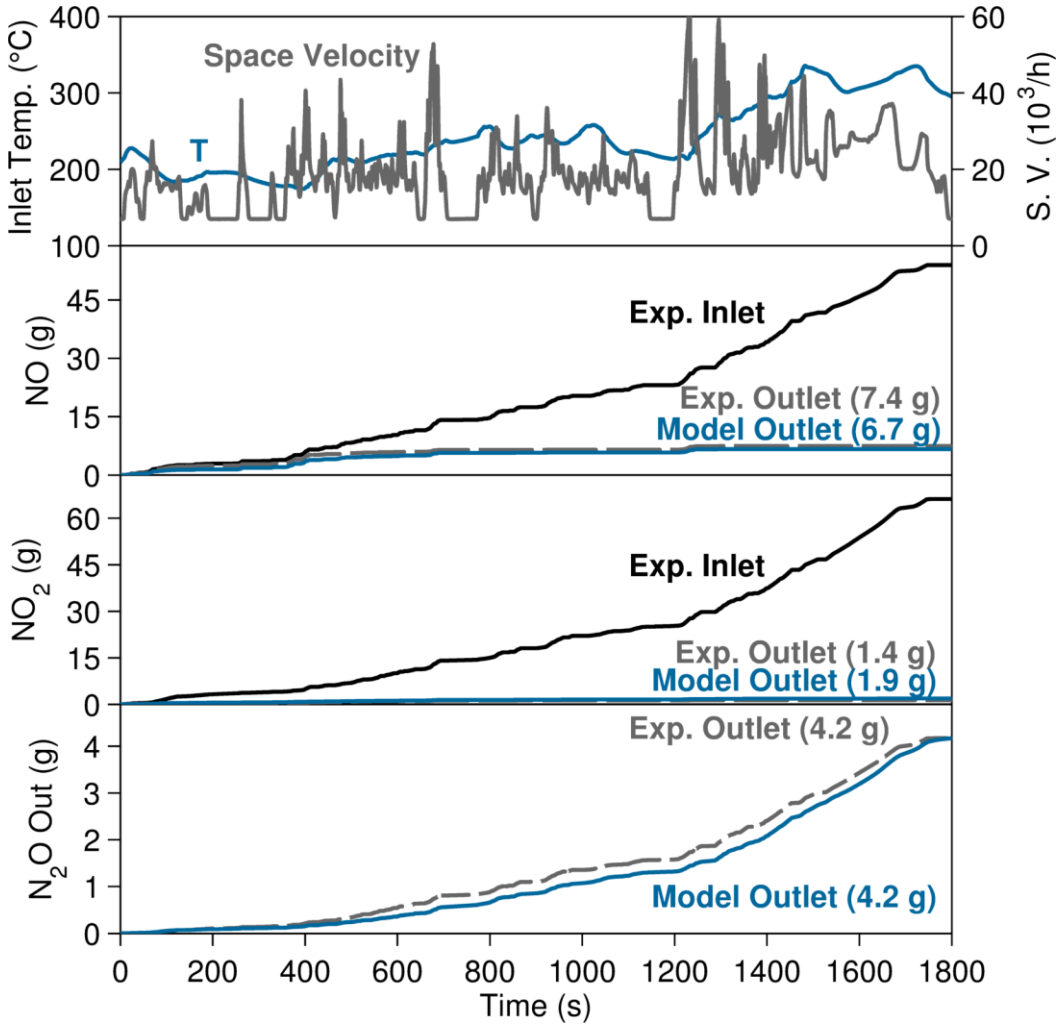

Figure 2.13 – Predictive simulation of WHTC driving cycle.

A plot of the simulated surface coverage is shown in Figure 2.14. Here, it is seen that only a maximum of 8 % ammonium blocking species (Cu^{2+}-$NO_3[NH_3]$) are predicted to inhibit the copper active sites over the driving cycle. No nitrates (Cu^{2+}-NO_3) and no ammonium nitrate (NH_4NO_3*) on the ammonia storage sites are predicted to form. As the temperature increases towards the end of the driving cycle, the ammonium blocking species decreases, meaning they will no longer play an inhibitive role at the end of the cycle.

The surface coverages throughout the driving cycle (Figure 2.14) vary significantly from the predicted surface coverages at steady state conditions (Figure 2.8B, Figure 2.12B). Clearly, a model that assumes steady state for the nitrate species and is calibrated based on only steady state data, would not be able to predict the transient conversion correctly. This emphasizes the importance of modelling transient effects (i.e., ammonia storage, nitrites, and nitrates) to capture the dynamics during driving cycles, since steady state conditions are not reached.

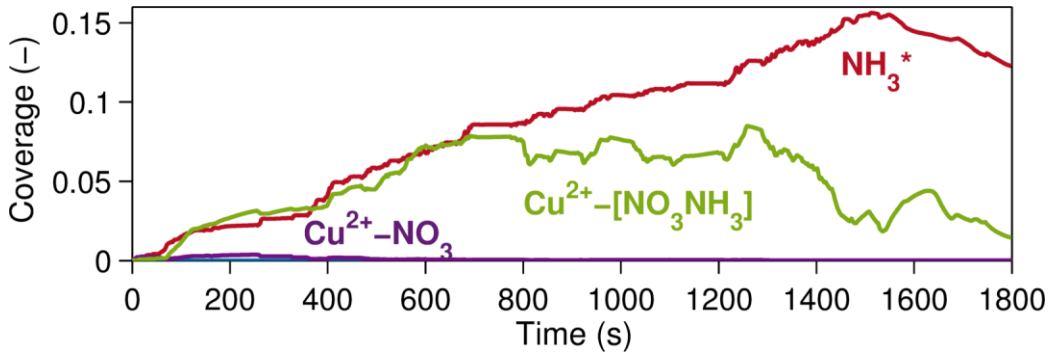

Figure 2.14 – Predicted surface coverage for WHTC driving cycle.

2.5 Conclusions

In this work, a surface reaction mechanism was developed by integrating various mechanistic pathways proposed in literature. The presented mechanism describes the main SCR reactions (Standard SCR, Fast SCR, NO_2 SCR) as well as transient effects due to nitrate storage. A dual site approach was used, where site 1 accounts for the adsorbed ammonia on Brønsted acid and copper ions, while site 2 represents a copper ion (Cu^{2+}-OH) where nitrates and nitrites could form.

All main SCR reactions proceed *via* a reaction between ammonia and nitrites (ammonium nitrite pathway) to produce nitrogen; the nitrites are also modelled to be the linking species between the Standard SCR and NO oxidation reactions. Ammonium nitrate formation and decomposition effects were included in the model, in addition to a low temperature (< 250 °C) global reaction that was observed to take place between NH_3 and NO_2 on the zeolite catalyst.

The reaction parameters were fit to steady state and transient experiments and predict the behaviour of the catalyst during a driving cycle, without any refitting of kinetic parameters required. The surface coverages of ammonium nitrate-like species (Cu^{2+}-$NO_3[NH_3]$, NH_4NO_3*) throughout the driving cycle were significantly less than during the Fast and NO_2 SCR steady state experiments. Thus, if we would have fit to only steady state data, we would have assumed a substantial amount of steady state surface species, and incorrectly predicted the transient, driving cycle conversion. This observation emphasizes the importance of modelling transient behaviour rather than steady state activity for the simulation of driving cycles. The minimal formation of

nitrate species during the driving cycle, however, does not necessarily imply that nitrate or ammonium nitrate effects do not play a role during other driving scenarios with longer periods of low temperature operation that might occur during real world driving.

Finally, this paper shows that the current mechanistic understanding of the different SCR subreactions forms a useful basis for the construction of a kinetic model that describes and predicts the behaviour of the copper chabazite catalyst under realistic operating conditions. However, it needs to be emphasized that most of the individual submechanisms used in this work are not settled and still under investigation. Nevertheless, we believe that the individual mechanisms should be integrated into comprehensive models at an early stage. This not only leads to a better understanding of the transient catalyst behaviour, but also contributes to the discussion of the individual submechanisms, as it helps to understand their role and importance in the overall reaction system.

2.6 References

[1] I. Nova, E. Tronconi (Eds.), Urea-SCR Technology for deNOx After Treatment of Diesel Exhausts, Springer (2014).

[2] M. Koebel, M. Elsener, M. Kleeman, Urea-SCR: a promising technique to reduce NOx emissions from automotive diesel engines, Catal. Today 59 (2000) 335-345.

[3] M. Colombo, I. Nova, E. Tronconi, A comparative study of the NH3-SCR reactions over a Cu–zeolite and a Fe–zeolite catalyst, Catal. Today 151 (2010) 223–230.

[4] A. Schuler, M. Votsmeier, P. Kiwic, J. Gieshoff, W. Hautpmann, A. Drochner, H. Vogel, NH3-SCR on Fe zeolite catalysts -- From model setup to NH3 dosing, Chem Eng. J. 154 (2009) 333-340.

[5] H.-Y. Chen, Z. Wei, M. Kollar, F. Gao, Y. Wang, J. Szanyi, C. H. F. Peden, A comparative study of N2O formation during the selective catalytic reduction of NOx with NH3 on zeolite supported Cu catalysts, J. Catal. 329 (2015) 490-498.

[6] M. Colombo, I. Nova, E. Tronconi, NO2 adsorption on Fe- and Cu-zeolite catalysts: The effect of the catalyst red-ox state, Appl.Cat. B 111-112 (2012) 433-444.

[7] J. Jansson, Vanadia-Based Catalysts for Mobile SCR, in: I. Nova, E. Tronconi (Eds.), Urea-SCR Technology for deNOx After Treatment of Diesel Exhausts, Springer (2014) 65-96.

[8] D. W. Fickel, E. D'Addio, J. A. Lauterbach, R. F. Lobo, The ammonia selective catalytic reduction activity of copper-exchanged small-pore zeolites, Appl Catal. B 102 (2011) 441-448.

[9] A. M. Beale, F. Gao, I. Lezcano-Gonzalez, C. H. F. Peden, J. Szanyi, Recent advances in automotive catalysts for NOx emission control by small-pore microporous materials, Chem. Soc. Rev. 44 (2015) 7371.

[10] F. Gao, E. D. Walter, M. Kollar, Y. Wang, J. Szanyi, C. H. F. Peden, Understanding ammonia selective catalytic reduction kinetics over Cu/SSZ-13 from motion of Cu ions, J. Catal. 319 (2014) 1-14.

[11] S. A. Bates, A. A. Verma, C. Paolucci, A. A. Parekh, T. Anggara, A. Yezerets, W. F. Schneider, J. T. Miller, W. N. Delgass, F. H. Ribeiro, Identification of the active Cu site in standard selective catalytic reduction with ammonia on Cu-SSZ-13, J. Catal. 312 (2014) 87-97.

[12] A. A. Verma, S. A. Bates, T. Anggara, C. Paolucci, A. A. Parekh, K. Kamasamudram, A. Yezerets, J. T. Miller, W. N. Delgass, W. F. Schneider, F. H. Ribeiro, NO oxidation: A probe reaction on Cu-SSZ-13, J. Catal. 312 (2014), 179-190.

[13] H. Zhu, J. H. Kwak, C. H. F. Peden, J. Szanyi, In situ DRIFTS-MS studies on the oxidation of adsorbed NH3 by NOx over a Cu-SSZ-13 zeolite, Catal. Today 205 (2013) 16–23.

[14] I. Lezcano-Gonzalez, U. Deka, B. Arstad, A. Van Yperen-De Deyne, K. Hemelsoet, M. Waroquier, V. Van Speybroeck, B. M. Weckhuysen, A. M. Beale, Determining the storage, availability, and reactivity of NH3 within Cu-Chabazite-based Ammonia Selective Catalytic Reduction systems, Phys. Chem. Chem. Phys. 16 (2014) 1639–1650.

[15] S. Brandenberger, O. Kroecher, A. Tissler, R. Althoff, P. D. Schettler, The State of the Art in Selective Catalytic Reduction of NOx by Ammonia Using Metal-Exchanged Zeolite Catalysts Catalysis Reviews, Sci. Eng. 50 (2008) 492-531.

[16] M. P. Ruggeri, T. Selleri, M. Colombo, I. Nova, E. Tronconi, Identification of nitrites/HONO as primary products of NO oxidation over Fe-ZSM-5 and their role in the Standard SCR mechanism: A chemical trapping study, J. Catal. 311 (2014) 266-270.

[17] M. P. Ruggeri, I. Nova, E. Tronconi, J. A. Pihl, T. J. Toops, W. P. Partridge, In-situ DRIFTS measurements for the mechanistic study of NO oxidation over a commercial Cu-CHA catalyst, Appl. Catal. B 166-167 (2015) 181-192.

[18] M. P. Ruggeri, T. Selleri, I. Nova, E. Tronconi, J. A. Pihl, T. J. Toops, W. P. Partridge, New Mechanistic Insights in the NH3-SCR Reactions at Low Temperature, Top. Catal. 59 (2016) 907-912.

[19] J. H. Kwak, J. H. Lee, S. D. Burton, A. S. Lipton, C. H. F. Peden, J. Szanyi, A Common Intermediate for N2 Formation in Enzymes and Zeolites: Side-On Cu-Nitrosyl Complexes, Angew. Chem. Int. Ed. 52 (2013) 9985-9989.

[20] F. Gao, J. H. Kwak, J. Szanyi, C. H. F. Peden, Current Understanding of Cu-Exchanged Chabazite Molecular Sieves for Use as Commercial Diesel Engine DeNOx Catalysts, Top. Catal. 56 (2013) 1441-1459.

[21] C. Paolucci, A. A. Verma, S. A. Bates, V. F. Kispersky, J. T. Miller, R. Gounder, W. N. Delgass, F. H. Ribeiro, W. F. Schneider, Isolation of the Copper Redox Steps in the Standard Selective Catalytic Reduction of Cu-SSZ-13, Angew. Chem. Int. Ed. 53 (2014) 11828-11833.

[22] T. Guenter and H. W. P. Carvalho and D. E. Doronkin and T. Sheppard and F. Glatzel and A. J. Atkins and J. Rudolph and C. R. Jacob and M. Casapu and J.-D. Grunwaldt, Structural snapshots of the SCR reaction mechanism on Cu-SSZ-13, Chem. Commun. 51 (2015) 9227-9230.

[23] T. V. W. Janssens, H. Falsig, L. F. Lundegaard, P. N. R. Vennestrom, S. B. Rasmussen, P. G. Moses, F. Giordanino, E. Borfecchia, K. A. Lomachenko, C. Lamberti, S. Bordiga, A. Godiksen, S. Mossin, P. Beato, A Consistent Reaction Scheme for the Selective Catalytic Reduction of Nitrogen Oxides with Ammonia, ACS Catal. 5 (2015) 2832-2845.

[24] A. Grossale, I. Nova, E. Tronconi, D. Chatterjee, M. Weibel, The chemistry of the NO/NO2-NH3 “fast” SCR reaction over Fe-ZSM5 investigated by transient reaction analysis, J. Catal. 256 (2008) 312-322.

[25] M. P. Ruggeri, A. Grossale, I. Nova, E. Tronconi, H. Jirglova, Z. Sobalik, FTIR in situ mechanistic study of the NH3-NO/NO2 “Fast SCR” reaction over a commercial Fe-ZSM-5 catalyst, Cat. Today 184 (2012) 107-114.

[26] A. Grossale, I. Nova, E. Tronconi, Role of Nitrate Species in the “NO2 SCR” Mechanism over a Commercial Fe-zeolite Catalyst for SCR Mobile Applications, Catal. Lett. 130 (2009) 525-531.

[27] L. Olsson, K. Wijayanti, K. Leistner, A. Kumar, S. Y. Joshi, K. Kamasamudram, N. W. Currier, A. Yezerets, A multi-site kinetic model for NH3-SCR over Cu/SSZ-13, Appl. Cat. B 174-175 (2015) 212-224.

[28] P. Metkar, M. P. Harold, V. Balakotaiah, Experimental and kinetic modeling study of NH3-SCR of NOx on Fe-ZSM-5, Cu-chabazite and combined Fe- and Cu-zeolite monolithic catalysts, Chem. Eng. Sci. 87 (2013) 51-66.

[29] M. Colombo, I. Nova, E. Tronconi, Detailed kinetic modeling of the NH3-NO/NO2 SCR reactions over a commercial Cu-zeolite catalyst for Diesel exhausts after treatment, Catal. Today 197 (2012) 243-255.

[30] E. Tronconi, P. Forzatti, Adequacy of lumped parameter models for SCR reactors with monolith structure, AlChE J. 38 (1992) 201-210.

[31] K. E. Brenan, S. L. Campbell, L. R. Petzold, Numerical Solution of Initial-value Problems in Differential-algebraic Equations, Elsevier Science Publishing Co. (1989).

[32] B. Opitz, M. Bendrich, A. Drochner, H. Vogel, R. E. Hayes, J. F. Forbes, M. Votsmeier, Simulation study of SCR catalysts with individually adjusted ammonia dosing strategies, Chem. Eng. J. 264 (2015) 936-944.

[33] A. Grossale, I. Nova, E. Tronconi, Study of a Fe–zeolite-based system as NH3-SCR catalyst for diesel exhaust aftertreatment, Catal. Today 136 (2008) 18-27.

[34] A. Grossale, I. Nova, E. Tronconi, Ammonia blocking of the ‘‘Fast SCR” reactivity over a commercial Fe-zeolite catalyst for Diesel exhaust aftertreatment, J. Catal. 265 (2009) 141-147.

[35] J.-S. McEwen, T. Anggara, W.F. Schneider, V.F. Kispersky, J.T. Miller, W.N. Delgass, F.H. Ribeiro, Integrated operando X-ray absorption and DFT characterization of Cu-SSZ-13 exchange sites during the selective catalytic reduction of NOx with NH3, Catal. Today 184 (2012) 129-144.

[36] F. Gao, E. D. Walter, E. M. Karp, J. Luo, R. G. Tonkyn, J. H. Kwak, J. Szanyi, C. H.F. Peden, Structure-activity relationships in NH3-SCR over Cu-SSZ-13 as probed by reaction kinetics and EPR studies, J. Catal. 300 (2013) 20-29.

[37] L. Arnarson, H. Falsig, S. B. Rasmussen, J. V. Lauritsen, P. G. Moses, A complete reaction mechanism for standard and fast selective catalytic reduction of nitrogen oxides on low coverage VOx/TiO2(001) catalysts, J. Catal. 346 (2017) 188-197.

[38] K. Hadjiivanov, J. Saussey, J. L. Freysz, J. C. Lavalley, FT-IR study of NO + O2 co-adsorption on H-ZSM-5: reassignment of the 2133 cm-1 band to NO+ species, Cat. Lett. 52 (1998) 103-108.

[39] J. A. Loiland, R. F. Lobo, Oxidation of zeolite acid sites in NO/O2 mixtures and the catalytic properties of the new site in NO oxidation, J. Catal. 325 (2015) 68-78.

Chapter 3 – Impact of ammonium nitrate formation on SCR activity over a Cu-CHA catalyst

A version of this chapter will be submitted as: M. Bendrich, A. Scheuer, R. E. Hayes, M. Votsmeier, Impact of ammonium nitrate formation on SCR over a Cu-CHA catalyst.

3.1 Introduction

To ensure lower CO_2 emissions, emission regulations are increasingly being based on colder driving cycles that are designed to give a better representation of actual automotive behaviour. In terms of diesel vehicle emissions, the lower temperatures make it more challenging for the selective catalytic reduction (SCR) catalysts to meet the NO_x limits owing to urea-injection difficulties and catalyst effectiveness. As a result, catalysts are continuously being developed to allow for the main SCR reactions (Standard SCR (1), Fast SCR (2), and NO_2 SCR (3)) to proceed such that they meet the desired conversions [1, 2]:

$$4NH_3 + 4NO + O_2 \rightarrow 4N_2 + 6H_2O \quad (1)$$

$$2NH_3 + NO + NO_2 \rightarrow 2N_2 + 3H_2O \quad (2)$$

$$4NH_3 + 3NO_2 \rightarrow 3.5\ N_2 + 6H_2O \quad (3)$$

Copper zeolite catalysts are attractive given their high SCR activity at low temperatures. More specifically, the copper chabazite (Cu-CHA) catalysts have recently received a significant amount of attention in the literature, owing to their small-pores that allow for improved hydrothermal stability [3]. Additionally, the Cu-CHA's small-pore structure is responsible for a higher thermal stability of ammonium nitrate (4) compared to its large pore counterparts (i.e., Cu-BEA), resulting in less N_2O formation (5), but also allowing the possibility that a significant amount of ammonium nitrate can inhibit the active catalytic sites [4]. This inhibition of ammonium nitrate on the SCR steady state performance at low temperatures (< 200 °C) with high NO_2/NO_x ratios (i.e., > 50%) is undesirable [5, 6, 4, 7].

$$2NH_3 + 2NO_2 \rightarrow N_2 + NH_4NO_3 + H_2O \quad (4)$$

$$NH_4NO_3 \rightarrow N_2O + 2H_2O \quad (5)$$

To improve understanding and mitigation of ammonium nitrate formation, research results focusing on the impact of ammonium nitrate on the Cu-zeolite catalyst performance have been published: Chen et al. [4] compared the stability of ammonium nitrate on Cu-CHA and Cu-BEA catalysts to understand its implications on N_2O formation; Luo et al. [7] established boundary conditions for ammonium nitrate inhibition on Cu-CHA and sought to understand its formation *via* DRIFTS; Ottinger et al. [8] analyzed the impact of hydrothermal aging on ammonium nitrate formation; Colombo et al. [9] completed experiments to understand the role of ammonium nitrate-like species in NO_2-related chemistry; however, it should be noted that despite these meaningful contributions providing insights on ammonium nitrate

formation, it is still not clear exactly where and how the ammonium nitrate forms and decomposes. Additionally, methods have been developed to quantify the amount of ammonium nitrate accumulated during catalyst testing [10], and a hybrid catalyst solution with a Fe-zeolite catalyst followed by a Cu-zeolite catalyst has been established to allow for an increased steady state, low temperature, fast SCR activity [5]. While ammonium nitrate is deemed undesirable due to its inhibition, research on an Fe-zeolite SCR catalyst has demonstrated that the addition of ammonium nitrate to feeds with NO_2/NO_x ratios below 50% is beneficial, as the presence of nitrates allows the standard SCR activity to approach the fast SCR activity [11].

To date, the impact of ammonium nitrate-like species on SCR activity has mainly been discussed at steady state conditions, which has led to the idea that high NO_2/NO_x ratios at low temperatures are undesirable owing to ammonium nitrate inhibition. However, the recent development of a detailed mechanistic model for Cu-CHA, which captures transients related to nitrate storage and reaction, demonstrated that the simulated amount of ammonium nitrate during a hot WHTC driving cycle (final cumulated NO_2/NO_x = 43%) is low compared to the simulated amount during steady state conditions with NO_2/NO_x > 50% [12]. Thus, during this WHTC it was not seen that ammonium nitrate accumulated and inhibited the catalyst performance, however a detailed study of ammonium nitrate accumulation, especially during cold starts, was not investigated in detail.

Therefore, the purpose of this work is to explore further the influence of ammonium nitrate formation on the NO_x conversion of a commercial, state-of-the-art, Cu-CHA

catalyst during steady state and transient conditions (e.g., cold WHTCs). To perform this investigation, the amount of ammonium nitrate deposited on the catalyst at low temperature, steady state conditions is first established *via* an experimental method from Ruggeri et al. [10] and simulations [12]. Step tests of different lengths between low and high NO_2/NO_x ratios are then implemented, to observe and understand the influence of ammonium nitrate on the NO_x conversion. These tests show that ammonium nitrate storage deviations from steady state generally allow for a higher NO_x conversion than its corresponding steady state value. Finally, multiple cold WHTCs with a final, cumulated 60% NO_2/NO_x ratio are run at our driving cycle test bench, and simulated with our mechanistic model, to investigate how much ammonium nitrate forms during the driving cycles. Both the simulations and applied experimental method demonstrate that little ammonium nitrate accumulates during the cold WHTC, owing to the rapidly changing NO_2/NO_x conditions.

3.2 Methods

3.2.1 TPSR laboratory test bench measurements

Temperature programmed surface reaction (TPSR) experiments were conducted, where multiple species were added in various orders at a constant temperature, for different lengths of time, to allow for reactions to occur between the desired species. All experiments had 5% H_2O and 6% O_2, with N_2 as the balance gas, and began with a treatment to ensure that no species were adsorbed on the catalyst at the beginning of the experiment. The gas hourly space velocity (GHSV) for all experiments was 50,000 h^{-1} referenced to STP.

The experiments were completed with a commercial, state-of-the-art, copper chabazite catalyst contained in a washcoat supported on a cordierite monolith substrate. The monolith samples had the following properties: 2.5 cm diameter, 5.1 cm length, cell density of 400 cpsi, and a wall thickness of 109 μm.

The monolith sample was placed inside a quartz tube through which the feed gas of selected composition and temperature was passed. A thermocouple monitored the inlet gas temperature, which was recorded and is used throughout this paper. The outlet gas composition was measured by an FTIR. The tubing from the reactor to the FTIR was heated to 185 °C to avoid ammonium nitrate deposition. The samples were aged in a flow of 10% O_2 and 10% H_2O with N_2 as the balance gas for 16 hours at 750 °C prior to use.

3.2.2 Driving cycle test bench measurements

Cold World Harmonized Transient Cycles (WHTC) were performed using the laboratory test bench described in [13], which is designed to simulate driving cycles. The use of this dynamic test bench is valuable for the ammonium nitrate quantification investigation, since it allows for the easy implementation of test protocols to driving cycles (i.e., NO titration after WHTC), which is shown in Section 3.4.3. The inlet conditions to the SCR for the WHTCs were taken from engine test bench data, where the catalytic converter system before the SCR consisted of a diesel oxidation catalyst (DOC) and a diesel particle filter (DPF); an NH_3/NO_x constant dosing strategy ratio of 1.2 was applied, with an ammonia dosing restriction when the

temperature was below 180 °C. A FTIR, CLD, and oxygen sensor measured the outlet composition.

The Cu-CHA monolith sample used at this laboratory test bench had the same chemical composition and aging protocol as described in Section 3.2.1, with the following geometrical properties: 5.1 cm diameter, 11.4 cm length, cell density of 400 cpsi, and a wall thickness of 109 μm.

3.3 Models

3.3.1 Reactor model

The reactor model assumes that all channels, their washcoat distribution, and the inlet conditions to each channel are identical, allowing one to model the monolith using a single channel. 1D mass and energy balances were solved for the species in the gas phase and washcoat, where axial advection in the gas phase, mass and heat transfer from the gas phase to washcoat, and source terms from the reactions in the washcoat were included. The position dependent mass and heat transfer coefficients were calculated *via* a Nu and Sh correlation for laminar flow [14]. Internal mass transfer in the washcoat was not explicitly accounted for, and therefore the kinetic parameters may include diffusion effects. The channel was discretized axially, and the mass and energy balances were integrated using DASSL [15]. For a detailed description of the 1D mass and energy balances used, refer to Opitz et al. [16].

3.3.2 Kinetic model

The kinetic model used was developed by Bendrich et al. [12] (Chapter 2) and describes the SCR reactions in terms of ammonia, nitrates, nitrites, and ammonium nitrate surface species. In this model, a dual site approach is used, where one site (*) accounts for the adsorbed ammonia (NH_3*) that forms on the Brønsted sites and copper ions, while another site (Cu^{2+}-OH) accounts for the nitrates ($Cu^{2+} – NO_3$) and nitrites (Cu^{2+} – ONO) adsorbed on the copper ion. While the exact location and mechanism for ammonium nitrate formation is not understood, the model captures the slow inhibition dynamics at low temperatures and high NO_2/NO_x *via* $Cu^{2+} – NO_3[NH_3]$ and NH_4NO_3* species (see [12]), a similar approach to Colombo et al. [9]. Since both species inhibit the catalyst activity, in this work, our simulated $Cu^{2+} – NO_3[NH_3]$ and NH_4NO_3* species are grouped together and called ammonium nitrate. The reaction scheme implemented from [12] is listed in Table 3.1.

Table 3.1 – Reaction mechanism.

	Reaction
R1	$NH_3 + * \leftrightarrow NH_3*$
R2	$2NO_2 + Cu^{2+} - OH \leftrightarrow Cu^{2+} - ONO + HNO_3$
R3	$HNO_3 + Cu^{2+} - OH \leftrightarrow Cu^{2+} - NO_3 + H_2O$
R4	$NO_2 + Cu^{2+} - ONO \leftrightarrow Cu^{2+} - NO_3 + NO$
R5	$Cu^{2+} - NO_3 + H_2O \rightarrow NO_2 + ¼O_2 + Cu^{2+} - OH$
R6	$Cu^{2+} - ONO + NH_3* \rightarrow N_2 + H_2O + Cu^{2+} - OH + *$
R7	$Cu^{2+} - ONO + NH_3* + ½O_2 \rightarrow N_2O + H_2O + Cu^{2+} - OH + *$
R8	$3Cu^{2+} - NO_3 + 2NH_3* \rightarrow 3Cu^{2+} - ONO + N_2 + 3H_2O + 2*$
R9	$Cu^{2+} - NO_3 + NH_3* \leftrightarrow Cu^{2+} - NO_3[NH_3] + *$
R10	$Cu^{2+} - NO_3[NH_3] \rightarrow N_2O + H_2O + Cu^{2+} - OH$
R11	$Cu^{2+} - NO_3[NH_3] + * + H_2O \leftrightarrow NH_4NO_3* + Cu^{2+} - OH$
R12	$2Cu^{2+} - OH + NO \leftrightarrow Cu^{2+} - ONO + H_2O + Cu^{+}$
R13	$Cu^{+} + ½H_2O + ¼O_2 \rightarrow Cu^{2+} - OH$
R14	$Cu^{2+} - ONO + ½H_2O + ¼O_2 \leftrightarrow NO_2 + Cu^{2+} - OH$
R15	$4NH_3* + 5O_2 \rightarrow 4NO + 6H_2O + 4*$
R16	$2NH_3* + 2O_2 \rightarrow N_2O + 3H_2O + 2*$
R17	$2Cu^{2+} - NO_3 + 2NH_3* \rightarrow N_2 + 2NO + 2H_2O + 2Cu^{2+} - OH + 2*$
R18	$2NH_3* + 2NO_2 \rightarrow 2N_2 + 3H_2O + ½O_2 + 2*$

3.4 Results & discussions

3.4.1 Steady state, ammonium nitrate storage at 200 °C and 50,000 h^{-1}

The first goal was to establish a steady state, ammonium nitrate storage line at 200 °C and 50,000 h^{-1}, to plot a relationship between the amount of ammonium nitrate stored on the Cu-CHA catalyst at steady state conditions and the NO_2/NO_x in the feed. This storage line is used in the succeeding subsections to compare the magnitude of ammonium nitrate stored during transient tests. To quantify ammonium nitrate in nitrogen flow, the method published by Ruggeri et al. [10] was used. The implementation of that [10] method at our laboratory test bench is described below, using the experiment shown in Figure 3.1 as a guide:

1. Ammonium nitrate formation (Figure 3.1, 0 to 4600 s): To allow for possible ammonium nitrate formation, a feed of 500 ppm NH_3, 500 ppm NO_x, 6% O_2, 5% H_2O, and N_2 as the balance gas was passed through the catalytic converter until steady state was reached. Since the amount of ammonium nitrate at different NO_2/NO_x ratios is to be determined, the ratio was varied between each experiment such that NO_2/NO_x = 0, 25, 40, 50, 60, 75, and 100%. The space velocity of 50,000 h^{-1} and temperature of 200 °C are held constant.
2. Titration of ammonium nitrate with NO (Figure 3.1, 4600 to 6200 s): To quantify the amount of ammonium nitrate stored [10], 500 ppm NO with 5% H_2O and N_2 as balance gas were passed over the catalytic converter until steady state conditions were reached. According to [10], the decomposition of ammonium nitrate *via* NO (6) and Fast SCR (2) would take place during this

step, allowing one to calculate the extent of reactions of (6) and (2) by solving the system of equations (2 element balances, NO consumed and NO_2 produced known), and thus the amount of ammonium nitrate stored.

$$NH_4NO_3 + NO \rightarrow NO_2 + 2H_2O + N_2 \quad (6)$$

3. Temperature ramp (Figure 3.1, 6200 s to end): To observe whether any species remained on the catalyst, NO was removed from the feed, and a temperature ramp of 10 K/min was run. According to [10], any NO_x desorption would need to be accounted for when calculating ammonium nitrate storage amount. As seen in Figure 3.1, no NO_x was observed to desorb during the temperature ramp, and only ammonia desorbed in the experiments when $NO_2/NO_x \leq 50\%$ (not shown).

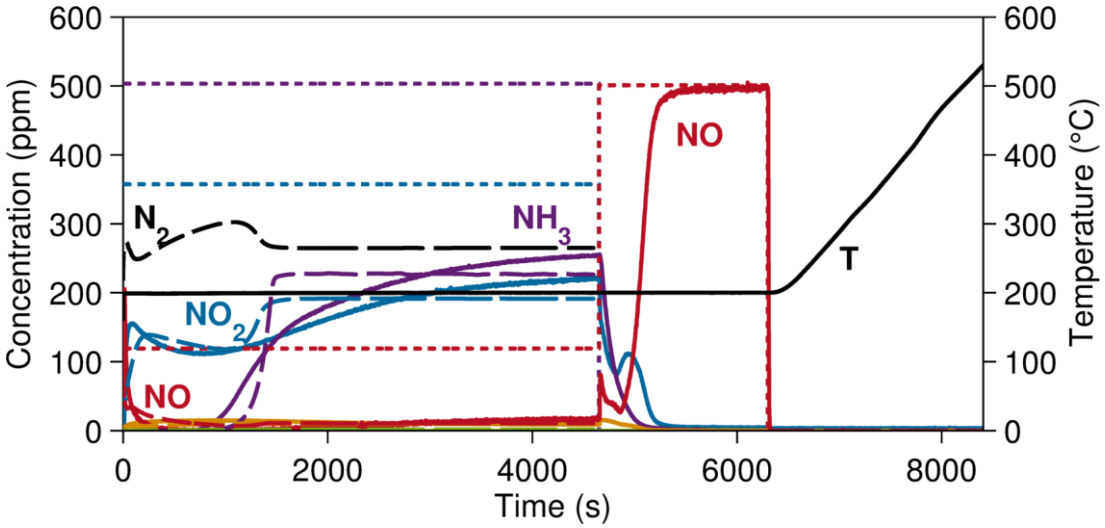

Figure 3.1 – Ammonium nitrate quantification experiment for a feed (dotted lines) of 500 ppm NH_3 and NO_x, NO_2/NO_x = 75%, 5% H_2O, 6% O_2, and N_2 balance gas; GHSV at STP = 50,000 h^{-1}. Experimental outlet is shown by the solid lines and the simulated outlet is shown by the dashed lines.

In addition to plotting the experimental output, Figure 3.1 also shows the quality of our simulation for NO_2/NO_x = 75% during the ammonium nitrate formation phase (0 to 4600 s). Since the model was not originally parameterized for a feed without oxygen, the quality of the simulation during the NO titration is not shown (4600 to 6200 s). Using the experimentally determined and simulated storage amounts, the corresponding experimental and simulated ammonium nitrate storage lines varying with NO_2/NO_x ratio are plotted in Figure 3.2.

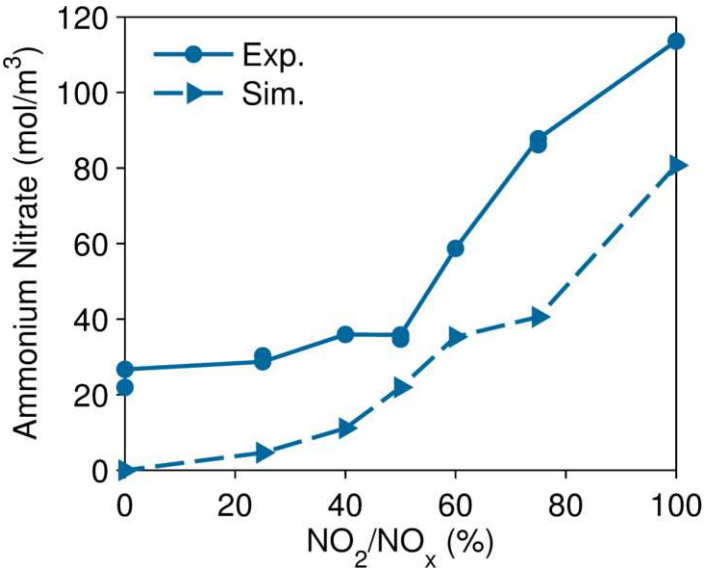

Figure 3.2 – Experimental and simulated ammonium nitrate storage line for different NO_2/NO_x ratios with a feed of 500 ppm NH_3, 500 ppm NO_x, 5% H_2O, 6% O_2, and N_2 balance gas at 200 °C and GHSV at STP of 50,000 h^{-1}. The simulated ammonium nitrate is the sum of the stored Cu^{2+} – $NO_3[NH_3]$ and NH_4NO_3* species.

In Figure 3.2, both the experimental and simulated amount of stored ammonium nitrate increases with the NO_2/NO_x ratio. However, the model consistently under predicts the stored ammonium nitrate observed in the experiment, although the model

generally simulates our various experiments well (i.e., experiments shown in our Cu-CHA model development publication [12]).

Unexpectedly, a significant amount of ammonium nitrate was calculated to form during the 0% NO_2/NO_x experiment, since a significant amount of NO was consumed during its titration phase (Figure S3.1 in Appendix A, 2700 to 4500 s). It is not expected that ammonium nitrate forms during Standard SCR conditions [8], demonstrating a challenge with the applicability of the method to this experiment. We hypothesize that when no more ammonium nitrate is present (i.e., Standard SCR) and ammonia is still stored, the NO added reacts with the stored ammonia until all the copper is reduced, according to the reduction portion of the Standard SCR reaction (7). Thus, the consumption of NO in such a scenario would result in the overprediction of the ammonium nitrate.

$$Cu^{2+}\text{-}OH + NO + NH_3* \rightarrow N_2 + 2H_2O + Cu^{+} \quad (7)$$

Including the reduction portion of the Standard SCR reaction (7) with the decomposition of ammonium nitrate *via* NO (6) and Fast SCR (2) to calculate the extent of each reaction, would require more element balances than we have known components (NO and NO_2). This means that the experiment would have to be conducted in a balance gas other than nitrogen, such that the nitrogen balance could be included to solve the system of equations.

Nevertheless, this ammonium nitrate quantification method in N_2 flow is a beneficial tool to gain an understanding of how much ammonium nitrate forms on the surface

during transient conditions compared to steady state and, keeping in mind its limitations, is used in the remainder of this work.

3.4.2 Boosting SCR activity with ammonium nitrate owing to changes in storage

The aim of this section is to observe how the ammonium nitrate affects the SCR deNO_x activity during fluctuating NO_2/NO_x conditions at low temperatures, and to relate the behaviour to the ammonium nitrate storage line shown in Figure 3.2. Therefore, a TPSR experiment was conducted at 200 °C and 50,000 h^{-1}, where the experiment is shown in Figure 3.3A, and its corresponding NO_x conversion is shown in Figure 3.3B. Throughout the entire experiment, a constant feed of 500 ppm NH_3, 500 ppm NO_x, 5% H_2O, 6% O_2, and N_2 as balance gas was passed through the catalytic converter. The NO_2/NO_x ratio is varied as follows and has the following effect on the catalyst:

1. NO_2/NO_x = 25% (Figure 3.3, 0 to 3500 s): For the first part of the experiment, the aforementioned inlet conditions with NO_2/NO_x = 25% were fed to an initially clean catalyst and held constant until steady state was reached; the NO_x conversion at steady state was 89%.
2. NO_2/NO_x = 75% (Figure 3.3, 3500 to 4700 s): Thereafter, the NO_2/NO_x ratio was increased to 75% and held constant for 20 minutes. During this time, the NO_x conversion initially increased, and then slowly decreased towards its steady state NO_x conversion of 46%.

3. NO_2/NO_x = 25% (Figure 3.3, 4700 to 8400 s): The NO_2/NO_x ratio of 25% is added again, to observe how the stored ammonium nitrate influences the NO_x conversion. Interestingly, the NO_x conversion initially peaks to its steady state value of 89%. It then decreases to 79%, and then slowly approaches its original steady state value of 89% again.

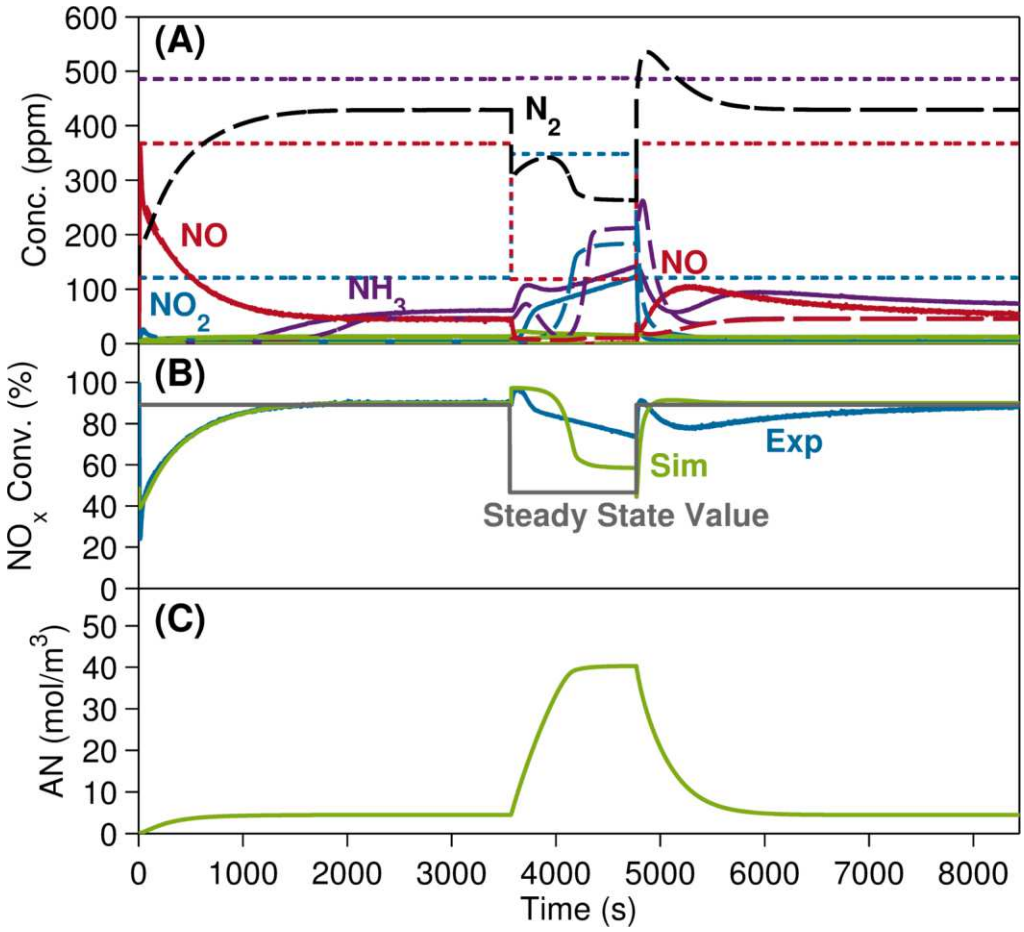

Figure 3.3 – (A) Experimental (solid lines) and simulated (dashed lines) concentrations, at a constant temperature of at 200 °C, for a successive feed of 1) NO_2/NO_x = 25% 2) NO_2/NO_x = 75% 3) NO_2/NO_x = 25%; Feed (dotted lines) = 500 ppm NH_3 and NO_x, 5% H_2O, 6% O_2, and N_2 balance gas; GHSV at STP = 50,000 h^{-1}. (B) Experimental, simulated, and the steady state NO_x conversion. (C) Simulated amount of stored ammonium nitrate. The simulated ammonium nitrate is the sum of the stored $Cu^{2+} – NO_3[NH_3]$ and NH_4NO_3* species.

While it is expected that the ammonium nitrate would a) slowly inhibit the catalyst's deNO$_x$ activity during the 75% NO$_2$/NO$_x$ conditions from 3500 to 4700 s and b) block the active sites, resulting in lower NO$_x$ conversion during 25% NO$_2$/NO$_x$ from 4700 to 8400 s, the highlight of this experiment is the occurrence of the two increased NO$_x$ conversion peaks from 3500 to 3700 s and from 4700 to 4900 s. To better understand why this occurs, the experiment was simulated using the mechanistic model (Section 3.3), with the prediction also being shown in Figure 3.3. While the simulation of the NO$_x$ conversion is not perfect, it captures the two increased NO$_x$ conversion peaks, and assists in hypothesizing this behaviour, which will be explained with our implemented reaction scheme (relevant reactions shown in Figure 3.4).

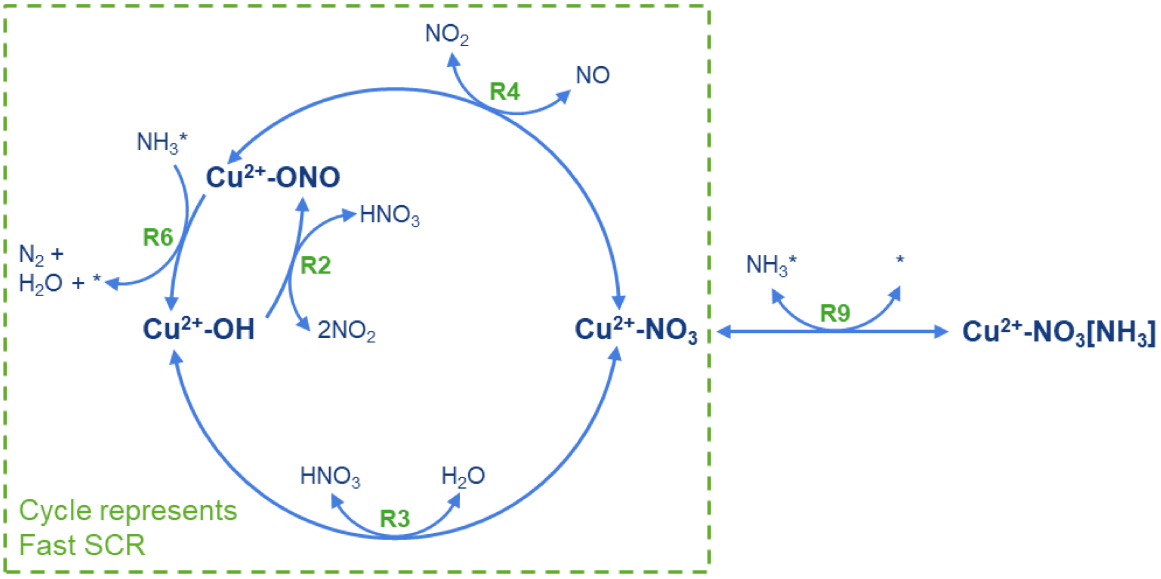

Figure 3.4 – Mechanism used to describe catalyst behaviour during step changes between low and high NO$_2$/NO$_x$ ratios.

First, the catalyst behaviour during NO_2/NO_x = 75% in Figure 3.3 (3500 to 4700 s) will be analyzed. According to the simulation, the amount of ammonium nitrate inhibiting the catalyst at the start of this part of the experiment is 5 mol/m^3 (at 3500 s), which corresponds to the steady state amount during the 25% NO_2/NO_x feed conditions, as seen in the simulated storage line of Figure 3.2. Since the 75% NO_2/NO_x feed conditions require 40 mol/m^3 of ammonium nitrate to reach storage conditions (Figure 3.2), the NO_x conversion initially increases to allow for this ammonium nitrate formation to occur.

In the ammonium nitrate formation process, the NO_2 is stored as unstable nitrites and stable nitrates (R2 and R3); the unstable nitrites react with NH_3 to produce N_2 (R6), while the stable nitrates react with either NO to produce nitrites again (R4) or with NH_3 to form ammonium nitrate-like species (Cu^{2+}-$NO_3[NH_3]$, R9) and inhibit the catalyst. The combination of the aforementioned steps (R2 + R3 + R4 + 2*R6), without the ammonium nitrate formation (R9), result in the Fast SCR mechanism. As a result, this Fast SCR pathway initially allows for a high deNOx activity, which slowly becomes inhibited and approaches its steady state value due to the formation of ammonium nitrate.

When the catalyst is exposed to the NO_2/NO_x = 25% step change (Figure 3.3, 4700 to 8400 s), the simulation predicts that 40 mol/m^3 ammonium nitrate initially is stored. Since the storage conditions require that only 5 mol/m^3 of ammonium nitrate are stored on the catalyst again (Figure 3.2), the stored ammonium nitrate decomposes to nitrates *via* R9. As a result, the NO reacts with the nitrates to produce nitrites (R4)

and the nitrites react with NH_3 *via* an ammonium nitrite pathway to produce N_2 (R6). The produced NO_2 from R4 is predicted to enter the Fast SCR reaction scheme; thus, the NO_2 would react with the Cu^{2+}-OH site, to produce more nitrates (R2 + R3), which then react with NO *via* R4 to produce nitrites, and the nitrites would react with NH_3 *via* R6. This decomposition of ammonium nitrate, resulting in the enhancement of the SCR NO_x activity when $NO_2/NO_x < 50\%$, has been named the "Enhanced SCR reaction" [11]. Finally, as ammonium nitrate is depleted and reaches equilibrium with the Cu^{2+}-OH sites, the catalyst activity (NO_x, N_2O) approaches the steady state 25% NO_2/NO_x activity.

In short, this experiment demonstrates that the limited inhibition as well as the storage and decomposition of ammonium nitrate on the Cu-CHA catalyst during varying NO_2/NO_x conditions may allow for an increased NO_x conversion. The model assists in explaining the phenomenon but does not describe the sudden, slow inhibition of $deNO_x$ activity owing to ammonium nitrate formation (3500 to 4700 s) or the fluctuating NO_x conversion owing to ammonium nitrate decomposition (4700 to 8400 s) correctly. However, since the purpose of the model is to describe transient driving cycles, it may not even be necessary to describe such a significant amount of ammonium nitrate storage and inhibition, as the length of time that the catalyst is exposed to a high NO_2/NO_x ratio is likely much shorter in time.

Therefore, to investigate the influence of ammonium nitrate on the $deNO_x$ activity, as well as evaluate the model performance under conditions more relevant to the transient driving cycles, step change tests with shorter step sizes were completed. An

experiment with many three-minute step changes between 25% and 75% NO_2/NO_x was implemented; the step changes were completed multiple times, such that the transient conditions could be analyzed once the catalyst outlet reached a constant, fluctuating behaviour. The constant, fluctuating behaviour of the catalyst for the three-minute step changes is shown in Figure 3.5.

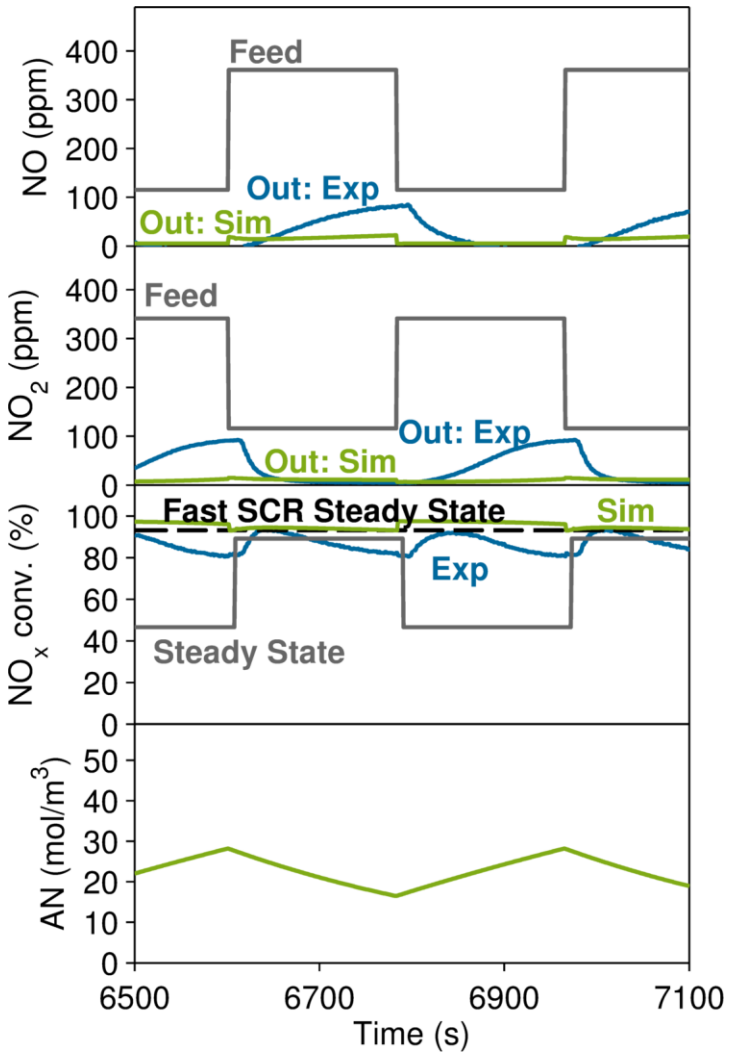

Figure 3.5 – Three-minute step changes between NO_2/NO_x = 25 and 75%. Feed = 500 ppm NH_3, 500 ppm NO_x, 5% H_2O, 6% O_2, N_2 as balance gas. GHSV at STP = 50,000 h^{-1}. Temperature = 200 °C. Many step changes were completed beforehand, until the catalyst reached the constant, fluctuating behaviour shown

here. The simulated ammonium nitrate is the sum of the stored $Cu^{2+} - NO_3[NH_3]$ and NH_4NO_3* species.

In Figure 3.5, it is seen that the experimental NO_x conversion first approaches and then diverges from the Fast SCR steady state conversion for both 25% and 75% NO_2/NO_x, resulting in a constant fluctuation. Similar to the experiment shown in Figure 3.3, we hypothesize that the increase in NO_x conversion towards the Fast SCR activity for the 75% NO_2/NO_x step change is owing to the consumption of NO_2, where the nitrates produced allow for the ammonium nitrate to slowly approach steady state conditions. As more ammonium nitrate accumulates on the catalyst surface, its storage gradually inhibits the deNO_x activity and the NO_x conversion slowly approaches towards its steady state value. We hypothesize that the NO_x conversion approaches the Fast SCR activity at 25% NO_2/NO_x due to the decomposition of ammonium nitrate to reach steady state conditions, resulting in a greater availability of nitrates to allow for the "Enhanced SCR reaction" to proceed [11]. The decrease of the NO_x conversion past the steady state conversion corresponding to 25% NO_2/NO_x is not understood, and we hypothesize that it has to do with the complex inhibition dynamics of ammonium nitrate.

The simulated ammonium nitrate fluctuation between a surface coverage of 26 and 17 mol/m^3 in Figure 3.5 provides a hypothesis as to why the catalyst buffers the changing NO_2/NO_x inlet conditions, resulting in an overall increased NO_x conversion. To verify whether the fluctuation of stored ammonium nitrate is also seen experimentally, the ammonium nitrate quantification method was applied to this

experiment at the end of the 25% and 75% NO_2/NO_x step changes, where the experiment corresponding to the 75% NO_2/NO_x step change is shown in Figure S3.2 in Appendix A. From these experiments, the determined amount of ammonium nitrate is 39 mol/m^3 and 45 mol/m^3 for the 25 and 75% NO_2/NO_x step change respectively. When plotting the stored ammonium nitrate on the experimental storage line in Figure 3.2, it is observed that the amount of ammonium nitrate fluctuates around the Fast SCR centre point, like in the simulation. This supports our hypothesis that deviations from the nitrates storage point for a given feed results in the storage and release of nitrates, which helps increase the SCR activity.

Unfortunately, the simulated and experimental NO_x conversion trends in Figure 3.5 do not agree. For instance, the model does not capture the NO_2 breakthrough within the 3-minute 75% NO_2/NO_x peak. However, the model would eventually predict an NO_2 breakthrough under the 75% NO_2/NO_x conditions, but as seen in Figure 3.3, the conditions would have to be held longer since the timing of the simulated NO_2 breakthrough is delayed. The NO breakthrough during the 3-minute 25% NO_2/NO_x peak is not predicted at all, which is owing to the same reason of not being able to describe the 25% NO_2/NO_x peak in Figure 3.3: a more detailed understanding for ammonium nitrate formation/decomposition on the Cu-CHA's various active sites needs to be obtained.

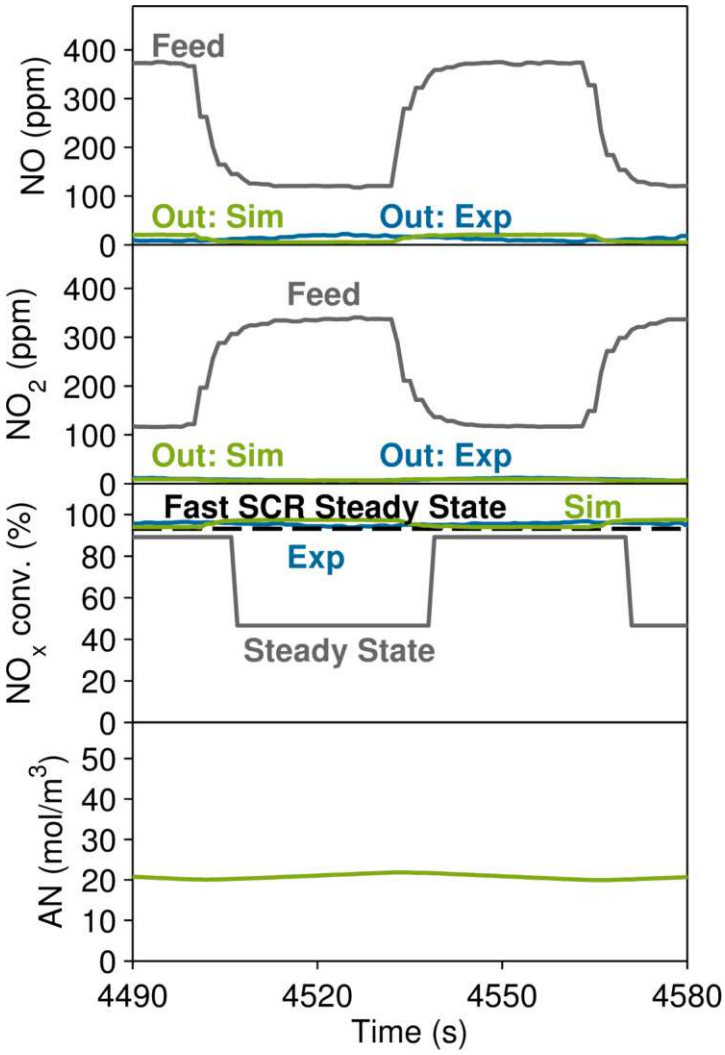

Figure 3.6 – 30-second step changes between NO_2/NO_x = 25 and 75%. Feed = 500 ppm NH_3, 500 ppm NO_x, 5% H_2O, 6% O_2, N_2 as balance gas. GHSV at STP = 50,000 h^{-1}. Temperature = 200 °C. Many step changes were completed beforehand, until the catalyst reached the constant, fluctuating behaviour shown here. The simulated ammonium nitrate is the sum of the stored $Cu^{2+} – NO_3[NH_3]$ and NH_4NO_3* species.

Finally, the same experiment was conducted with 30-second step changes and is shown in Figure 3.6. Given the short step size in this experiment, the plotted inlet reactor concentrations are the process values that were measured with a catalyst-free

monolith to capture the mass flow controller and dispersion effects. In this experiment, it is seen that little NO and no NO_2 breaks through and that the NO_x conversion corresponds to the Fast SCR conversion. Like before, the reason for this is the ability for the catalyst to buffer the feed conditions owing to deviations from the ammonium nitrate storage points corresponding to the 25 and 75% NO_2/NO_x feeds. Additionally, the short step changes do not allow for a substantial deviation from the Fast SCR ammonium nitrate storage point. The model predicts this conversion correctly, since there is almost complete conversion of the NO and NO_2, and thus the timing of their breakthrough does not play an effect on the conversion.

Overall, in this section we highlighted the ability of the stored ammonium nitrate to cushion the NO_x conversion during fluctuating NO_2/NO_x ratios. Capturing these increases in NO_x conversion requires a nitrate storage model, since the deviation of the stored ammonium nitrate from its storage amount can have a significant effect on the catalyst's deNO_x performance. Knowledge of the deviations between the stored and storage amount of ammonium nitrate could be leveraged to help increase the catalyst performance during transient driving cycles.

3.4.3 Ammonium nitrate formation during driving cycles

Having seen that the feed conditions influence the ammonium nitrate stored, which greatly affects the NO_x conversion, in a final step we investigate how much ammonium nitrate forms on the Cu-CHA catalyst during cold WHTC driving cycles with high cumulated NO_2/NO_x ratios (60%). To determine the quantity of ammonium nitrate stored, the simulated amount of ammonium nitrate will be compared to the

experimental amount using the method of Ruggeri et al. [10], as described in Section 3.4.1.

To capture the behaviour of Cu-CHA, four WHTCs were run successively at the dynamic test bench that can run driving cycles. No ammonia, nitrate, or ammonium nitrate was stored on the catalyst at the start of the first WHTC. The catalyst was cooled to its starting temperature between each driving cycle *via* forced convection with nitrogen, with less than 5% of the stored amount of ammonia desorbing because of the forced convection between the cycles. Additionally, a constant ammonia dosing strategy of $NH_3/NO_x = 1.2$, with an ammonia dosing restriction of 180 °C, was applied. The mechanistic model was also implemented, without the refitting of any kinetic parameters, to simulate the Cu-CHA's behaviour during the WHTC. Figure 3.7 shows the cumulated inlet, experimental output, and simulated output for the NH_3, NO, NO_2, and N_2O species, along with the predicted surface coverages, for the first WHTC at 60% NO_2/NO_x.

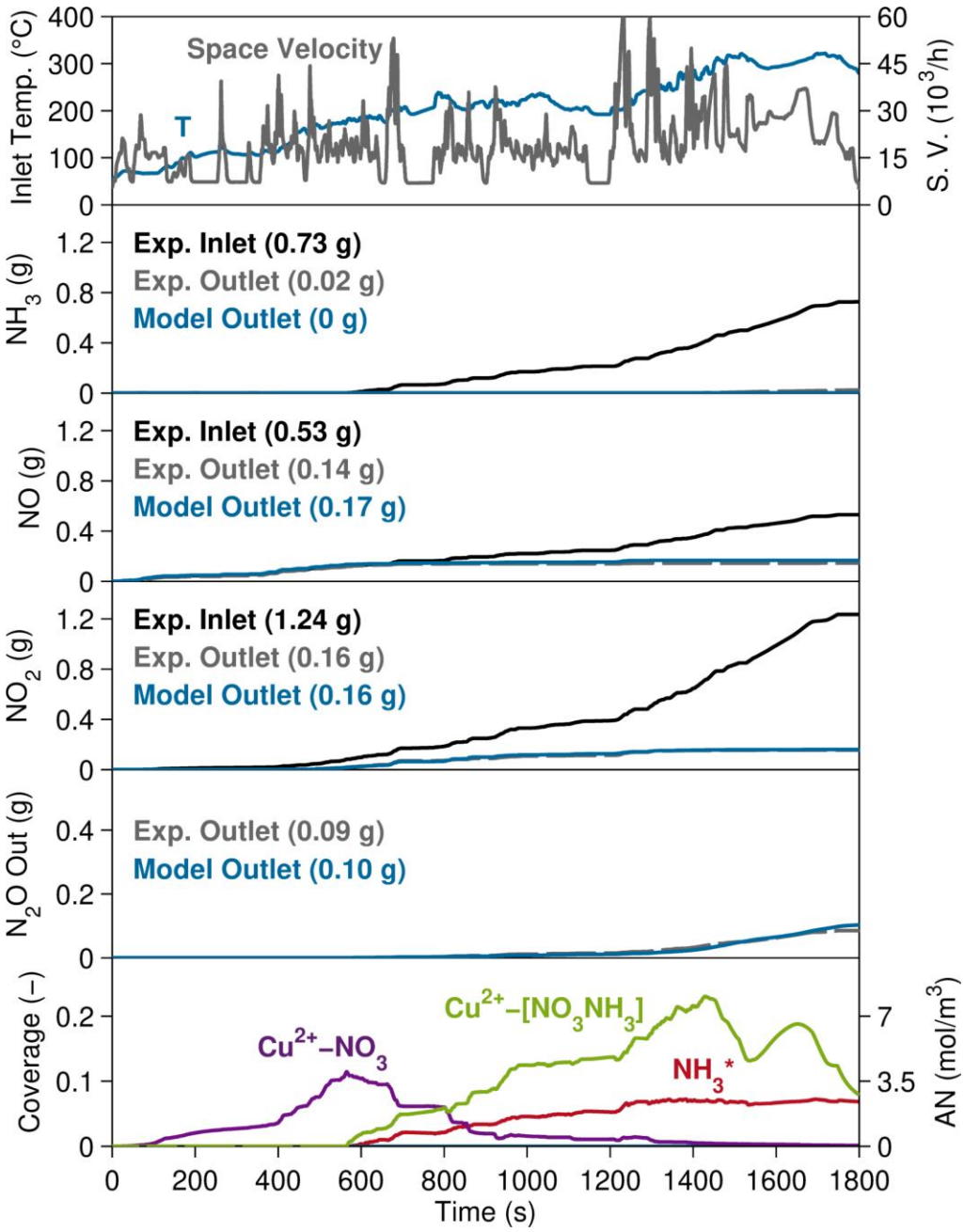

Figure 3.7 – Experimental and simulated Cu-CHA behaviour during a cold WHTC driving cycle (60% NO_2/NO_x) with initially empty catalyst. In this figure, the simulated ammonium nitrate is equivalent to the stored $Cu^{2+} – NO_3[NH_3]$ species, as no NH_4NO_3* is simulated to form.

In Figure 3.7, it is seen that the mechanistic model simulates the species conversion throughout the driving cycle very well and can be used to help us understand the Cu-CHA dynamics. For instance, since no ammonia is added to or stored on the catalyst until 600 s, due to the 180 °C ammonia dosing restriction, the Cu-CHA catalyst is still able to reduce the NO_2 emissions up until 600 s, owing to nitrate storage. The addition of ammonia at 600 s allows for greater NO_x conversion, along with ammonium nitrate formation and N_2O production. Interestingly, only a maximum of 22% (8 mol/m^3) of the copper sites are predicted to be blocked with ammonium nitrate, which is very little compared to the predicted steady state values shown in Figure 3.2.

To observe whether more ammonium nitrate is predicted to form during cold starts when ammonia is pre-stored on the catalyst, a second cold WHTC was run consecutively to the first (Figure 3.8). Figure 3.8 shows that fewer nitrates and more ammonium nitrate was predicted to form compared to the 1st WHTC in Figure 3.7, due to the available ammonia reacting with nitrates to produce ammonium nitrate. Nevertheless, the maximum predicted amount of ammonium nitrate did not increase significantly compared to the 1st WHTC, nor did the cumulated amount of N_2O emissions. The model was again able to capture the experimental dynamics very well. Since there were no changes in the experimental and simulated NH_3 conversion, NO_x conversion, N_2O formation, and predicted ammonium nitrate formation for the 3rd and 4th cold WHTC, the results are not shown here.

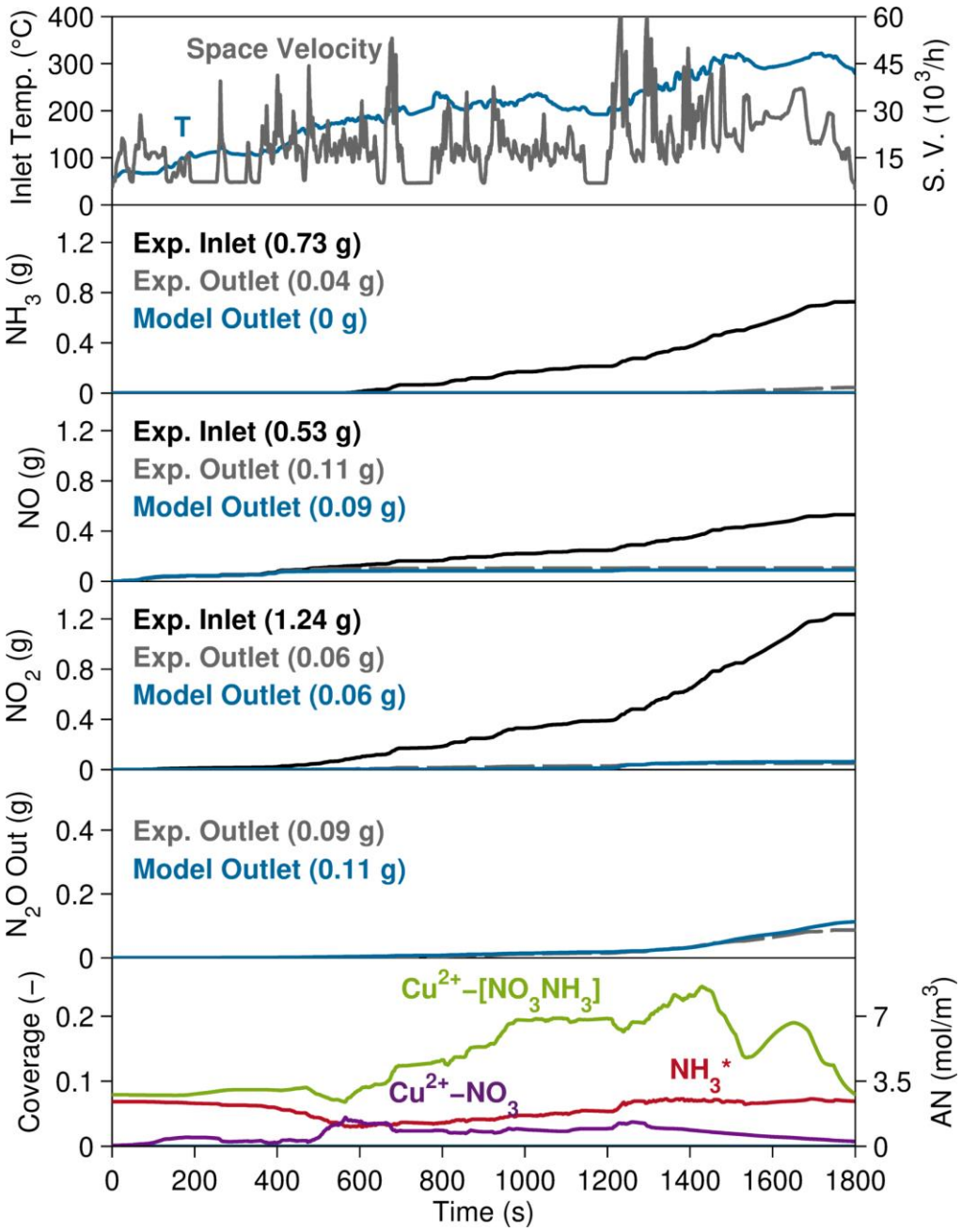

Figure 3.8 – Experimental and simulated Cu-CHA behaviour during a cold WHTC driving cycle (60% NO_2/NO_x) succeeding the WHTC in Figure 6. In this figure, the simulated ammonium nitrate is equivalent to the stored Cu^{2+} – $NO_3[NH_3]$ species, as no NH_4NO_3* is simulated to form.

As seen in Figure 3.7 and Figure 3.8, our simulation predicts that little ammonium nitrate (max. 8 mol/m^3) inhibits Cu-CHA during the WHTC. To verify whether the simulated amount of ammonium nitrate agrees with the experimental amount, Ruggeri et al.'s [10] ammonium nitrate quantification method discussed in Section 3.4.1 was applied at 677 and 1400 s for the 1st WHTC cycle shown in Figure 3.7. The titration experiment to quantify the transient amount of ammonium nitrate at 1400 s is shown in Figure S3.3 in Appendix A. The inlet values at 677 and 1400 s were also held until steady state was reached, followed by the titration experiment, to compare the driving cycle transient value to its hypothetical steady state value.

As seen in Table 3.2, the experimental quantification results in only 8 mol/m^3 and 16 mol/m^3 of ammonium nitrate being stored at 677 s and 1400 s, respectively, for the 1st cold WHTC. This is less than the corresponding steady state amount (e.g., if the inlet conditions at this time instance were held until steady state is reached) of 88 and 20 mol/m^3 at 677 and 1400 s. It can also be seen that these transient results are below the ammonium nitrate storage line at 200 °C (Figure 3.2).

Table 3.2 also shows that the simulation predicts a lower amount of ammonium nitrate being stored during the 1st cold WHTC, compared to steady state conditions. Thus, both the experiment and simulation demonstrate that little ammonium nitrate is stored on the catalyst compared to the steady state experiments.

Table 3.2 - Experimental and simulated ammonium nitrate during WHTC.

		Experiment (mol/m^3)	Simulation (mol/m^3)
677 s (60% NO_2/NO_x; 200 °C; 50,000 h^{-1})	Driving cycle	8	1
	Steady state	88	35
1400 s (70% NO_2/NO_x; 290 °C; 30,000 h^{-1})	Driving cycle	16	8
	Steady state	20	10

To understand why little ammonium nitrate forms during the WHTC, the ammonium nitrate predicted to form under the transient conditions was compared to the hypothetical simulated steady state values for the inlet conditions at every second (Figure 3.9). In Figure 3.9, it is seen that the inlet conditions from 0 to 600 s do not allow for the prediction of any ammonium nitrate formation at steady state, since no ammonia is being dosed to the SCR because the inlet temperature is below 180 °C. However, from 600 to 1500 s, there is a great fluctuation in predicted steady state ammonium nitrate, because the NO_2/NO_x ratio varies significantly. The rapid fluctuation of inlet conditions allows for slight formation and decomposition of ammonium nitrate, and thus never allows for a significant amount of ammonium nitrate accumulation since the conditions with high NO_2/NO_x and low temperatures are never held long enough. From 1500 to 1800 s, the simulated steady state ammonium nitrate then equals the simulated amount during the transient driving cycle and decreases slightly, owing to the increase temperature. Thus, it can be concluded that the variation in inlet NO_2/NO_x during the WHTC prevent a significant amount of ammonium nitrate from accumulating on the catalyst.

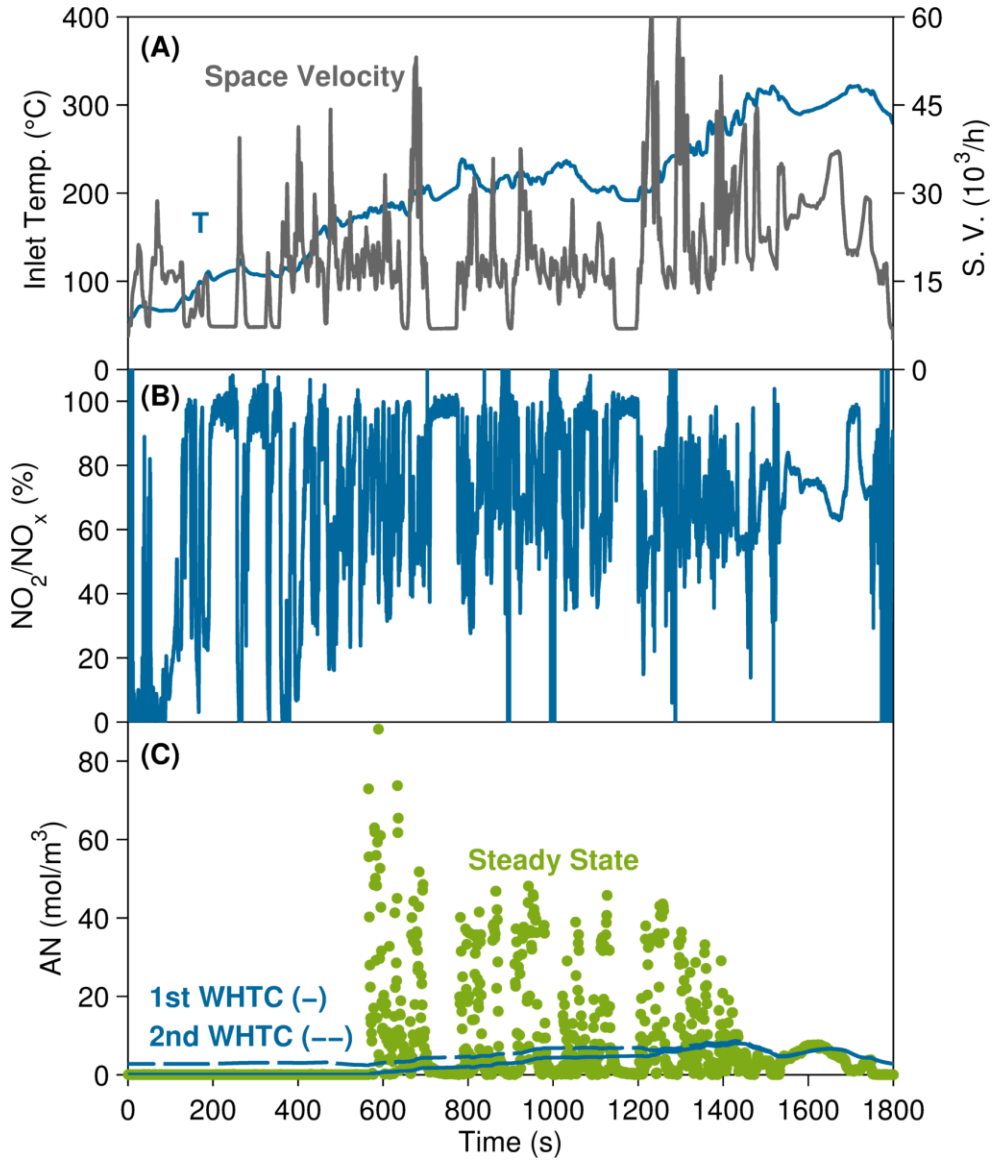

Figure 3.9 – (A) and (B) Inlet conditions for cold WHTC with 60% NO_2/NO_x shown in Figure 7 and Figure 8. (C) Simulated ammonium nitrate for WHTC in Figure 7 and Figure 8 (solid blue and dashed blue lines, respectively) as well as corresponding steady state ammonium nitrate value for every second (green dots). The simulated ammonium nitrate is the sum of the $Cu^{2+} – NO_3[NH_3]$ and NH_4NO_3* species.

Finally, the simulations and ammonium nitrate titration experiments have demonstrated that little ammonium nitrate forms during cold WHTCs with high

NO_2/NO_x, given the slow accumulation of ammonium nitrate, owing to rapidly fluctuating inlet conditions. From a modelling perspective, the inclusion of the ammonium nitrate storage in our simulation allows us to predict the catalyst behaviour for the corresponding catalyst surface species history, which allows us to capture the driving cycle trends very well.

3.5 Conclusions

In this work, we demonstrated that the Cu-CHA deNO_x activity is dependent on the ammonium nitrate stored, and that the inhibited deNO_x steady state performance at low temperatures (i.e., < 200 °C) and high NO_2/NO_x are not necessarily reached under transient conditions. To demonstrate this, we first quantified the amount of ammonium nitrate stored on the catalyst at steady state with varying NO_2/NO_x at 200 °C and 50,000 h^{-1}, using the ammonium nitrate quantification method of Ruggeri et al. [10] and compared the results to our simulation using our mechanistic model [12]; this steady state line was used as a basis to compare ammonium nitrate accumulation in succeeding transient experiments.

The completion of step changes of varying lengths between 25% NO_2/NO_x and 75% NO_2/NO_x at the same conditions as the steady state line, highlighted the ability of the Cu-CHA catalyst to buffer the NO_x conversion when the stored ammonium nitrate deviates from its steady state value. During the three-minute step change experiments, we observed that the NO_x conversion was generally higher than the corresponding steady state value and fluctuated close the Fast SCR steady state value. Our mechanistic model, which predicts a high NO_x conversion owing to fluctuations in

ammonium nitrate-like species, assisted in understanding this effect. According to the model, when the amount of ammonium nitrate stored is less than its corresponding steady state value (i.e., at 75% NO_2/NO_x), NO_x is stored as ammonium nitrate, resulting in a higher NO_x conversion which slowly approaches steady state. When the amount of ammonium nitrate stored is greater than its corresponding steady state value (i.e., at 25% NO_2/NO_x), the ammonium nitrate decomposes, and during the process, the available nitrates can assist in boosting the SCR activity as observed by Marchitti et al. [11]. These deviations in stored ammonium nitrate during these step change experiments were confirmed with the ammonium nitrate quantification method. Decreasing the step changes to 30-seconds showed that the NO_x conversion equalled the Fast SCR conversion, since the short step changes allow for little additional ammonium nitrate accumulation/decomposition.

Finally, we investigated the formation of ammonium nitrate during consecutive cold WHTCs with 60% NO_2/NO_x. Our simulations predict driving cycle dynamics very well but show little ammonium nitrate formation compared to our steady state line. The minimal formation of ammonium nitrate was again confirmed *via* the quantification experiments. Using our simulations, we conclude that the minimal formation of ammonium nitrate is owing to the rapid fluctuating NO_2/NO_x inlet conditions, which allows for slight formation and decomposition of ammonium nitrate, but never for a significant amount since the conditions are never held long enough. Overall, these results demonstrate that ammonium nitrate does not have a strong inhibitive effect on Cu-CHA during driving cycles.

On a final note, this work again emphasizes the importance of including nitrate and ammonium nitrate formation in the catalyst model, to be able to capture the NO_x conversions, which are dependent on the surface species history. A global model, calibrated to steady state Fast and NO_2 SCR points, and only considering ammonia as the adsorbed species, would not be able to capture the NO_x conversion trends, as it does not consider the complete stored species history (i.e., degree of ammonium nitrate accumulation). Although ammonium nitrate decomposition dynamics are more complex than our model can describe, the level of complexity is sufficient to capture the dynamics in the presented driving cycles.

3.6 References

[1] I. Nova, E. Tronconi (Eds.), Urea-SCR Technology for deNOx After Treatment of Diesel Exhausts, Springer (2014).

[2] M. Koebel, M. Elsener, M. Kleeman, Urea-SCR: a promising technique to reduce NOx emissions from automotive diesel engines, Catal. Today 59 (2000) 335-345.

[3] D. W. Fickel, E. D'Addio, J. A. Lauterbach, R. F. Lobo, The ammonia selective catalytic reduction activity of copper-exchanged small-pore zeolites, Appl. Catal. B 102 (2011) 441-448.

[4] H.-Y. Chen, Z. Wei, M. Kollar, F. Gao, Y. Wang, J. Szanyi, C. H. F. Peden, A comparative study of N2O formation during the selective catalytic reduction of NOx with NH3 on zeolite supported Cu catalysts, J. Catal. 329 (2015) 490-498.

[5] Y. Zha, Cummins Sustained Low Temperature NOx Reduction, https://energy.gov/sites/prod/files/2016/06/f33/pm068_zha_2016_o_web.pdf.

[6] L. Xie, F. Liu, K. Liu, X. Shi, H. He, Inhibitory effect of NO2 on the selective catalytic reduction of NOx with NH3 over one-pot synthesized Cu-SSZ-13 catalyst, Catal. Sci. Technol. 4 (2014) 1104.

[7] J. Luo, Y. Tang, S. Joshi, K. Kamasamudram, N. Currier, A. Yezerets, The Impact of Ammonium Nitrate Species on Low Temperature NOx Conversion Over Cu/CHA SCR Catalyst, SAE Technical Paper, 2017-01-0953.

[8] N. Ottinger, Y. Xi, C. Keturakis, Z. G. Liu, Impact of Hydrothermal Aging on the Formation and Decomposition of Ammonium Nitrate on a Cu/Zeolite SCR Catalyst, SAE Technical Paper, 2017-01-0946.

[9] M. Colombo, I. Nova, E. Tronconi, Detailed kinetic modeling of the NH3-NO/NO2 SCR reactions over a commercial Cu-zeolite catalyst for Diesel exhausts after treatment, Catal. Today 197 (2012) 243-255.

[10] Ruggeri, M. P., J. Luo, I. Nova, E. Tronconi, K. Kamasamudram, A. Yezerts, Novel method of ammonium nitrate quantification in SCR catalysts, Catal. Today 307 (2017) 48-54.

[11] F. Marchitti, E. Barker Hemings, I. Nova, P. Forzatti, E. Tronconi, Enhancing the Low-T NH3-SCR Activity of a Commmerical Fe-Zeolite Catalyst by NH4NO3 Dosing: an Experimental and Modeling Study, Emiss. Control Sci. Technol. 2 (2016) 1-9.

[12] M. Bendrich, A. Scheuer, R. E. Hayes, M. Votsmeier, Unified mechanistic model for Standard SCR, Fast SCR, and NO2 SCR over a copper chabazite catalyst, Appl. Catal. B 222 (2018) 76-87.

[13] F. Adam, J. Schoenhaber, A. Wagner, Synthetic Gas Bench (SGB) Tests Simulating Real and Dynamic Driving Conditions: A New and Cost Attractive Method for TWC Evaluation, SAE Technical Paper, 2015-01-1066.

[14] E. Tronconi, P. Forzatti, Adequacy of lumped parameter models for SCR reactors with monolith structure, AlChE J. 38 (1992) 201-210.

[15] K. E. Brenan, S. L. Campbell, L. R. Petzold, Numerical Solution of Initial-value Problems in Differential-algebraic Equations, Elsevier Science Publishing Co. (1989).

[16] B. Opitz, M. Bendrich, A. Drochner, H. Vogel, R. E. Hayes, J. F. Forbes, M. Votsmeier, Simulation study of SCR catalysts with individually adjusted ammonia dosing strategies, Chem. Eng. J. 264 (2015) 936-944.

Chapter 4 – Comparison of SCR and SCR + ASC performance: a simulation study

A version of this chapter will be submitted to a journal. A portion of this chapter has been used in my Master's thesis: M. Bendrich, A Systematic Approach for Performance Comparisons of NO_x Converter Designs, University of Alberta Thesis (2014). The new material includes the content and discussions related to Figure 4.5, Table 4.2, and Figure 4.8 as well as the entire material found in Section 4.4.5.

4.1 Introduction

Meeting the more stringent, government-imposed exhaust emission standards that result in more challenging driving cycles present a significant challenge in the development of efficient exhaust after-treatment systems. Selective catalytic reduction (SCR) has been, and currently is, the method of choice in attaining the demanding NO_x regulations for diesel vehicles emissions, at least for larger engines [1, 2]. This approach operates under the principle that ammonia, the reducing agent, is generated onboard through the hydrolysis of urea and is injected into the SCR according to a chosen dosing strategy. Ammonia can be adsorbed or desorbed by the SCR catalyst, which is beneficial when too much has been dosed or more is needed to convert the NO_x gas; however, the storage capacity of ammonia in the catalyst decreases strongly with an increase in temperature [1]. This means that a sharp

increase in load and engine, e.g. due to acceleration, can result in a significant amount of ammonia slip. Therefore, a well-designed catalytic converter and operating strategy must be developed, such that the NO_x conversion is maximized, while maintaining the ammonia slip below an acceptable level.

In terms of catalytic converter design, there is the possibility of adding an ammonia slip catalyst (ASC) as a short zone directly after the SCR to convert the ammonia exiting the SCR-zone to nitrogen. The ASC is able to increase the conversion of ammonia through its ammonia oxidation layer (AOC), which uses a platinum catalyst on a supported oxide. Where the platinum catalyst has a poor selectivity to nitrogen at high temperatures, resulting in NO_x formation from the ammonia oxidation, a dual layer concept consisting of a lower AOC layer and an upper SCR layer is used to increase the ASC's selectivity to nitrogen [3].

Numerical simulation is an important tool for the development of these exhaust after-treatment systems, particularly where physical experiments are very time consuming and costly [4, 2]. In this context, the SCR has been well-modelled and the literature provides a good overview [2, 5, 6, 7, 8]. Models for the ASC have also been published and have been used for analyzes of the ASC design. For instance, Scheuer et al. [3] used their published, experimentally-validated numerical model to complete a design parameter study (SCR layer washcoat loading, diffusion coefficient, catalyst size) on the steady state, ammonia oxidation activity for the ASC. In the process of developing and validating an ASC model, Colombo et al. [9, 10] compared steady state operations between dual-layer and mixed ASCs, where the powders of the two

different layers are mixed as a single layer. Shrestha et al. [11, 12] experimentally investigated the performance of a dual-layer and mixed ASC at different space velocities and reactant compositions to examine their effect on ammonia oxidation and N_2 selectivity.

In Opitz et al. [13], a simple ammonia dosing strategy was presented that can easily be applied to simulations to evaluate the true catalyst performance during driving cycles. With this approach, entities of a look-up table, which relate desired ammonia surface coverages to surface temperatures, are optimized to maximize the overall NO_x conversion and maintain the ammonia slip below user-defined constraints. The application examples of the dosing strategy in Optiz et al. [13] demonstrated the importance of implementing an optimized dosing strategy to each catalyst to compare its true performance, and that the catalyst performance may be underestimated when applying dosing profiles optimized to other catalysts or constant alpha (ratio of ppm NH_3/ppm NO_x) dosing strategies [13].

Since the ammonia dosing strategy plays a significant role on the catalyst performance, in this work, optimized dosing strategies are applied to analyze the true performance potential of including an ASC behind an SCR during driving cycles. In particular, this work investigates the idea that the ASC's ability to lower ammonia slip can result in a more aggressive ammonia dosing strategy being applied to increase the overall SCR and ASC system's NO_x conversion. To obtain the true performance potential of the ASC catalytic converter on the overall NO_x conversion

and ammonia slip, the complete SCR and ASC catalytic converter configuration needs to be considered.

The comparisons shown in this work provide a better understanding of the value of an ASC throughout driving cycles and its impact on the overall system's NO_x conversion and ammonia slip. While this investigation was mainly completed using the experimentally validated ASC model of Scheuer et al. [3], comprising of an upper Fe-zeolite SCR layer, comparisons are also made using a Cu-CHA model [8] for the SCR washcoat of the catalyst configuration. To begin the investigation, the base performance of the two catalytic converter designs (SCR versus SCR with an ASC) are investigated and compared *via* steady state tests and a system response test to a sudden increase in temperature. Thereafter, driving cycles are used, and the optimized ammonia dosing strategy presented in [13] is applied to make meaningful comparisons between the catalytic converter designs under transient inputs. Finally, the effect of design parameters such as the ASC length and the ASC's SCR washcoat loading on the catalyst system performance during driving cycles is investigated. Overall, it is shown that the true value of an ASC is its ability to limit ammonia slip when an error in dosing occurs, rather than allow for a more aggressive ammonia dosing strategy to increase the overall NO_x conversion of the catalytic converter system.

4.2 Models

In this work, two different catalytic converter configurations were used and are compared. The first catalytic converter design used throughout this simulation study

consisted of an 8” SCR catalyst. The second design had a front-end SCR and a back-end ASC. The length of the SCR varied based on the length of the ASC such that the combined monolith length is 8”. A schematic of both catalytic converter layouts can be seen in Figure 4.1. Where a dual-layer ASC is used, the upper SCR layer had the same washcoat loading as the 8” SCR. Both of these systems had a diameter of 12”, a density of 400 cpsi, and a wall thickness of 6.5 mil.

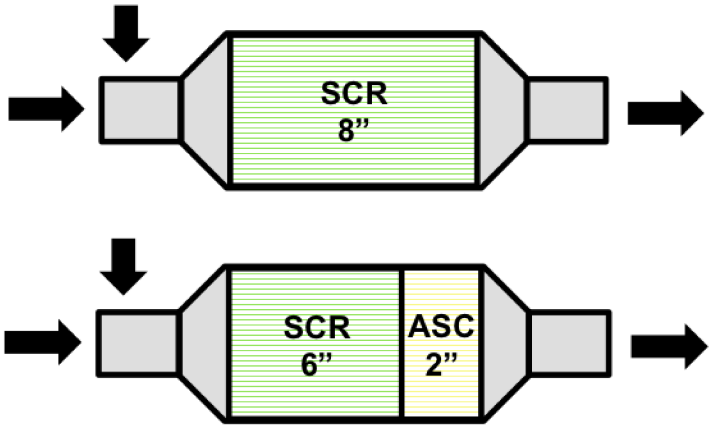

Figure 4.1 – Catalytic converter layouts used.

Single channel models are used to describe the behaviour of the exhaust gas passing through both the SCR and the ASC. As the geometrical properties of the channels, their catalyst distribution, and the inlet conditions are assumed identical, the model is assumed to be representative of each channel in the reactor. A 1D model is used for simulation of the SCR channels, whereas a 1D + 1D model is used for the ASC. Both of these models will be briefly described in the following subsections and are explained in more detail in [14].

4.2.1 SCR model

In the one-dimensional SCR model, the temperature and concentration variations in the radial direction have been neglected and are assumed to be mixing cup values (lumped parameters). Equations (1) and (2) describe the mass balances for the gas phase and the gas in the washcoat, respectively. Equation (1) accounts for the axial convection and mass transfer from the gas phase to the washcoat, and Equation (2) also accounts for the mass transfer and the reaction in the specific washcoat layer.

$$\frac{\partial c_{gas,i}}{\partial t} = -v_{gas} \cdot \frac{\partial c_{gas,i}}{\partial z} - \beta_i \cdot \frac{4}{D_H} \cdot \left(c_{gas,i} - c_{wc,i}\right) \tag{1}$$

$$\frac{\partial c_{wc,i}}{\partial t} = \varphi \cdot \beta_i \cdot \left(c_{gas,i} - c_{wc,i}\right) + \sum_j \left(v_{i,j} \cdot r_j\right) \tag{2}$$

In the equations above, c_{gas} and c_{wc} represent the concentration of the gas i and the gas species i in the washcoat phase, respectively and z represents the axial position in the reactor. Additionally, the variable v_{gas} represents the average gas velocity, D_H is the hydraulic diameter, β_i represents the position-dependent mass transfer coefficient, and φ is a geometrical factor for the specific surface area between the gas and solid phase per washcoat volume.

Equations (3) and (4) describe the energy balances for the gas phase and gas in the washcoat. Equation (3) accounts for convection and the heat added to the gas from the surface. Equation (4) accounts for the heat transferred from the solid to the gas as well as the heat released from the reaction.

$$\frac{\partial T_{gas}}{\partial t} = -v_{gas} \cdot \frac{\partial T_{gas}}{\partial z} - \alpha \cdot \frac{4}{D_H \cdot \rho_{gas} \cdot c_{p,gas}} \cdot \left(T_{gas} - T_{wc}\right) \tag{3}$$

$$\frac{dT_{wc}}{dt} = \alpha \cdot \frac{4}{D_H \cdot \rho_{wc} \cdot c_{p,wc}} \cdot \left(T_{gas} - T_{wc}\right) + \frac{\sum_j \left(\Delta H_j \cdot r_j\right)}{\rho_{wc} \cdot c_{p,wc}} \quad (4)$$

In the equations above T_{gas} represents the gas temperature and T_{wc} represents the temperature of the washcoat. Additional definitions of variables include ρ, which the density, c_p is the heat capacity, ΔH_j is the reaction enthalpy, and r_j is the reaction rate. The system of mass and energy balances were solved numerically for each volume element. More detail regarding the reactor model can be found in [14].

The SCR kinetic model for an Fe-zeolite catalyst was previously published in [5]. The model was parameterized using steady state and transient data, and takes into account the following global reactions:

Adsorption/Desorption $NH_3 + [*] \leftrightarrow NH_3*$ (R1)

Standard SCR: $4NH_3 + 4NO + O_2 \rightarrow 4N_2 + 6H_2O$ (R2)

Fast SCR: $4NH_3 + 2NO + 2NO_2 \rightarrow 4N_2 + 6H_2O$ (R3)

NO_2 SCR: $8NH_3 + 6NO_2 \rightarrow 7N_2 + 12H_2O$ (R4)

Ammonia oxidation: $4NH_3 + 3O_2 \rightarrow 2N_2 + 6H_2O$ (R5)

NO oxidation: $NO + 0.5 \leftrightarrow NO_2$ (R6)

The SCR model for the Cu-CHA catalyst has been published in Bendrich et al. [8] and accounts for the reactions above *via* a mechanistic approach. While this model has been validated for the SCR, it has not been validated in combination with a lower platinum layer for an ASC. Details regarding the Cu-CHA reaction mechanism can be found in [8] and Chapter 2.

4.2.2 ASC model

The ASC consists of an upper SCR layer and a lower ammonia oxidation layer and is typically added as a short zone after the SCR. Where the ASC must generally operate close to the mass transfer limit, radial mass diffusion effects in the washcoat must be considered and therefore a 1D + 1D model was used [15].

Hence, as completed with the SCR model, Equation (1), (3) and (4) are used to describe the concentration behaviour of the exhaust gas, temperature behaviour of the exhaust gas, and temperature behaviour in the washcoat through the ASC. For every lumped parameter gas phase position solved in the axial direction, a one-dimensional concentration and temperature profile is solved for in the radial direction for the two layers. The radial concentration is solved for in Equation (5) and Equation (6).

$$D_{eff} \cdot \frac{\partial c_{wc,i}}{\partial x}|_{x=0} = \beta_i \cdot \left(c_{wc,i|x=0} - c_{wc,i|x}\right) \tag{5}$$

$$\frac{\partial c_{wc,i}}{\partial x}|_{x=x\_max} = 0 \tag{6}$$

In Equations (5) and (6), the variable $D_{eff,i}$ represents the diffusion coefficient of species i in the washcoat and β_i is the mass transfer coefficient calculated according to the method of [16].

Owing to the ASC's dual-layer structure, different kinetic models are used for the ASC's upper and lower layer. Both SCR kinetic models briefly outlined in Section 4.2.1 were used for the upper SCR layer. The ammonia oxidation catalyst kinetic model from Scheuer et al. [3] is used for the lower ammonia oxidation layer, which accounts for the following global reactions:

$$4NH_3 + 3O_2 \rightarrow 2N_2 + 6H_2O \quad \text{(R7)}$$

$$2NH_3 + 2O_2 \rightarrow N_2O + 3H_2O \quad \text{(R8)}$$

$$2NH_3 + 5/2O_2 \rightarrow 2NO + 3H_2O \quad \text{(R9)}$$

$$2NH_3 + 7/2O_2 \rightarrow 2NO_2 + 3H_2O \quad \text{(R10)}$$

$$2NH_3 + 2NO + 1.5O_2 \rightarrow 2N_2O + 3H_2O \quad \text{(R11)}$$

$$NO + 0.5O_2 \leftrightarrow NO_2 \quad \text{(R12)}$$

$$2NH_3 + 2NO_2 + 0.5O_2 \rightarrow 2N_2O + 3H_2O \quad \text{(R13)}$$

The bottom-layer ammonia oxidation mechanistic model from Scheuer et al. [3] assumes that the kinetics are not influenced by internal mass transfer limitations, which is supported by the work of Votsmeier et al. [15] who showed that the diffusion effects could be neglected at washcoat loadings below 25 g/L.

4.3 Ammonia dosing strategy

Comparisons between the catalyst systems will be completed under steady state and transient conditions in Sections 4.4.1 and 4.4.3 onwards, respectively. The comparisons at steady state were completed under constant input conditions that are specified in their corresponding sections. Transient condition comparisons were completed using the WHTC; the ETC driving cycle [17] was used for comparison in Section 4.4.5.1. The input data used for the catalytic converter designs were experimental values from the engine test bench once the exhaust gas has passed through a DOC and a Catalyzed Diesel Particle Filter (CDPF). This means that only the SCR or SCR + ASC needs to be considered in all of the simulation study experiments. The space velocity for an 8” long catalytic converter with a 12”

diameter and the temperature profile for the WHTC and ETC driving cycle can be seen in Figure 4.2.

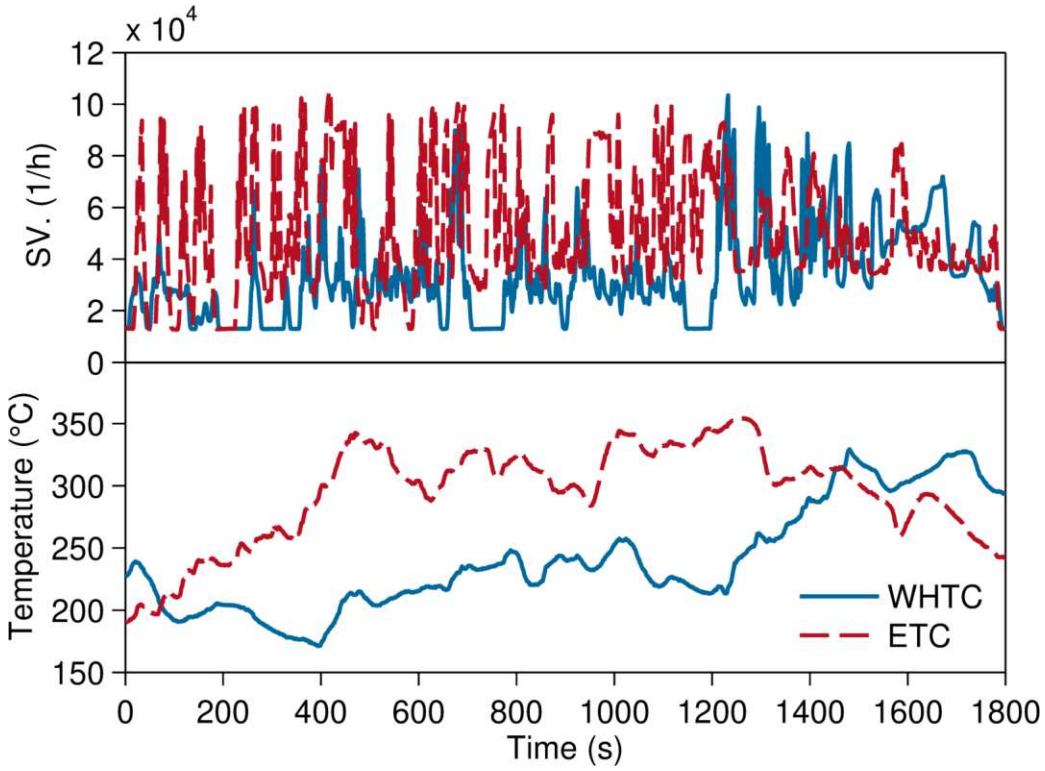

Figure 4.2 – Space velocity (8" long catalytic converter with 12" diameter) and temperature profile for the used WHTC and ETC driving cycle.

To make meaningful comparisons between the catalytic converters during transient conditions, an optimal ammonia dosing strategy must be considered [13, 18]. Therefore, Section 4.4.3, Section 4.4.5.1, and Section 4.4.5.2 use an optimized ammonia dosing strategy to evaluate the catalyst performance over a given driving cycle. This dosing strategy is briefly described here and more information can be found in Opitz et al. [13].

The ammonia dosing strategy achieves its goal for a given driving cycle, e.g. maximizing NO_x while fulfilling the ammonia slip constraints, according to a look-up table whose entries have been optimized for the given driving cycle. This optimized look-up table is essentially a piece-wise function that takes into account the catalyst activity by relating the catalyst temperature to a desired ammonia surface coverage.

Figure 4.3 will assist in explaining how the optimized look-up table is used for the dosing strategy, which can be described in the following three steps, that can be completed successively for each time instance of a given driving cycle:

1) At a given time instant (t), ammonia ($n_{NH3,in}(t)$) is injected into the exhaust gas stream in front of the catalyst. At this time instant, the SCR model is used to calculate the output variables including the average catalyst temperature ($T_{cat.}(t)$) and actual average ammonia surface coverage ($\theta_{act.}(t)$).
2) The look-up table is then used to determine the setpoint, or desired average ammonia surface coverage ($\theta_{des.}(t)$), for the current catalyst temperature *via* linear interpolation between table entries.
3) The amount of ammonia required for the actual surface coverage to reach the desired can then be calculated *via*:

$$n_{NH_3,in(t+\Delta t)f(x)}=\begin{cases}[\theta_{des.}(t)-\theta_{act.}(t)]\cdot\varepsilon\cdot V, & \theta_{des.}(t)>\theta_{act.}(t)\\ 0, & \theta_{act.}(t)>\theta_{des.}(t)\end{cases} \quad (8)$$

where $\theta(t)$ represents the average ammonia surface coverage, ε the number of active sites per reactor volume and V the catalyst volume.

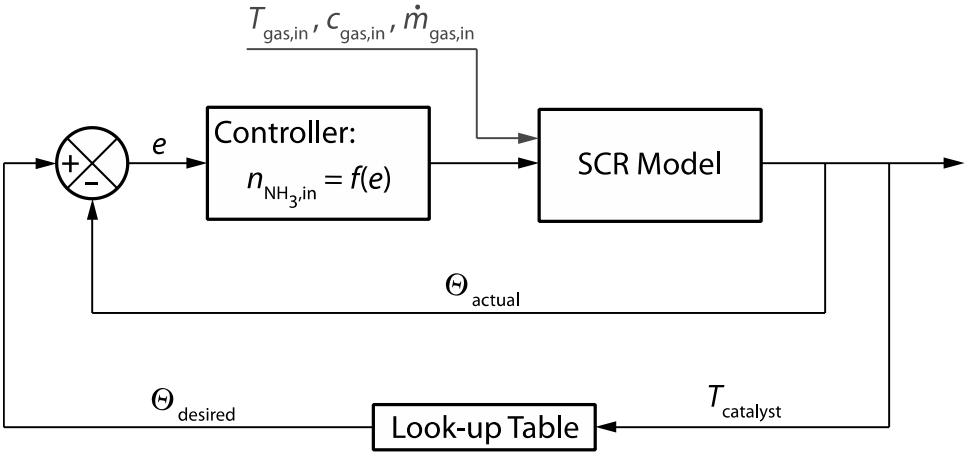

Figure 4.3 – Schematic of dosing strategy.

The optimization of the look-up table's entries is completed through the following summarized steps:

1) Adjusting the look-up table entry values *via* an optimization algorithm.
2) Using the look-up table for the ammonia dosing control in the simulation with a given driving cycle (Figure 4.3).
3) Calculating the resulting objective function (maximize NO_x conversion) and constraint values (e.g. ammonia slip constraints) from Step 2.

These steps are repeated until the change in the objective function was below a specified tolerance. For the coupled SCR-ASC configuration, it is important to note that the optimization was only completed based on the front-end SCR's catalyst temperature and ammonia surface coverage, and that the back-end ASC's catalyst temperature and ammonia surface coverage was not considered.

4.4 Results & discussion

4.4.1 System performance analysis at different alpha values

To begin investigating the benefit of an ASC, the steady state NO_x conversion and ammonia slip are compared when various alpha (ratio NH_3/NO_x) values are added to an 8" SCR and a coupled 6" SCR and 2" ASC system. The feed had an exhaust gas composition of 420 ppm NO, 180 ppm NO_2, 5% O_2, 5% H_2O, with N_2 as the balance gas, a constant space velocity of 30 000 h^{-1}, and an inlet gas temperature of either 200°C or 300°C. This analysis was first completed using the Fe-zeolite model as the SCR washcoat for the converter configurations.

Each converter configuration's change in NO_x conversion and ammonia slip with alpha at the specified temperature is seen in Figure 4.4. At 200°C, one can note that there is no ammonia slip at alpha values less than approximately 0.60 (Figure 4B), resulting in the NO_x conversion increasing identically from alpha 0.50 to 0.60 owing to the complete conversion of ammonia in the front end of the catalyst configuration (Figure 4A). At alpha values greater than 0.60, ammonia begins to break through and the NO_x conversion and ammonia slip values differ between the two systems (SCR vs. ASC). The SCR + ASC achieves higher NO_x conversion values compared to the 8" SCR because of the reaction between ammonia and NO_x to produce N_2O, a strong greenhouse gas [19], *via* R11 and R13 in the ASC system. Likewise, the SCR + ASC has less ammonia slip, owing to the ammonia oxidation (R7 and R8), R11 and R13. When setting the pre-exponential factor for the N_2O formation to zero, and thus preventing R11 and R13 from occurring, the 6" SCR + 2" ASC system would result

in the same NO_x conversion as the 8" SCR, with less ammonia slip (green, dashed line). In all cases, the NO_x conversion eventually no longer increases with alpha and, as a result, the ammonia slip values rise steeply.

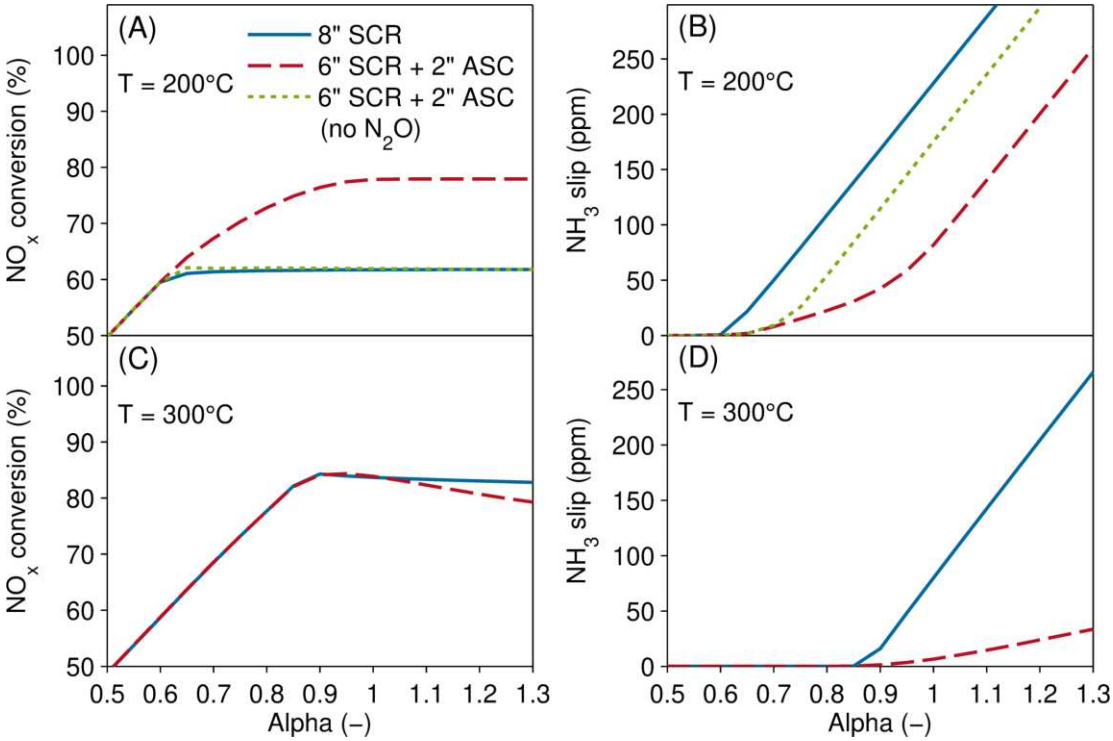

Figure 4.4 – NO_x conversion and ammonia slip for an 8" SCR and a 6" SCR with a 2" ASC zone during steady state alpha dosing simulation experiments at 200°C and 300°C. An Fe-zeolite catalyst was used as the SCR washcoat for the catalyst configurations.

The same effects can be seen for the catalytic converter behaviours at an inlet gas temperature of 300°C (Figure 4C and 4D) and an alpha value less than 0.85, when ammonia is being completely converted in the SCR. At alpha values above 0.85, the SCR + ASC system has less ammonia slip due to the ASC's ability to oxidize the ammonia exiting the SCR brick; however, the NO_x conversion does not exceed the

SCR's NO_x conversion for any alpha value. This occurs as the excess ammonia is being oxidized to NO_x in the ASC (R9 and R10), which occurs at higher temperatures. The NO_x conversion also decreases slightly with increasing alpha for the 8" SCR system because of the inhibition of ammonia.

The same analysis was also completed using the Cu-CHA catalyst model as the SCR washcoat for the catalyst configurations, with the results being shown in Figure 4.5. In Figure 4.5A, it is observed that unlike the Fe-zeolite, the NO_x performance is almost identical between the SCR and SCR + ASC configuration at 200 °C. This is owing to the higher conversion of NO_x in the SCR, which limits the amount of NO_x available in the oxidation layer to allow the reaction between ammonia and NO_x to N_2O (R11 and R13) to occur. The NO_x conversion at 300 °C (Figure 4.5C) is again almost identical for the SCR and SCR + ASC configuration, with the conversion decreasing slightly with increasing alpha owing to ammonia oxidation to NO_x (R9 and R10). As with the Fe-zeolite catalyst, the SCR + ASC configuration has less ammonia slip than the SCR, owing to the ammonia oxidation of the lower platinum layer.

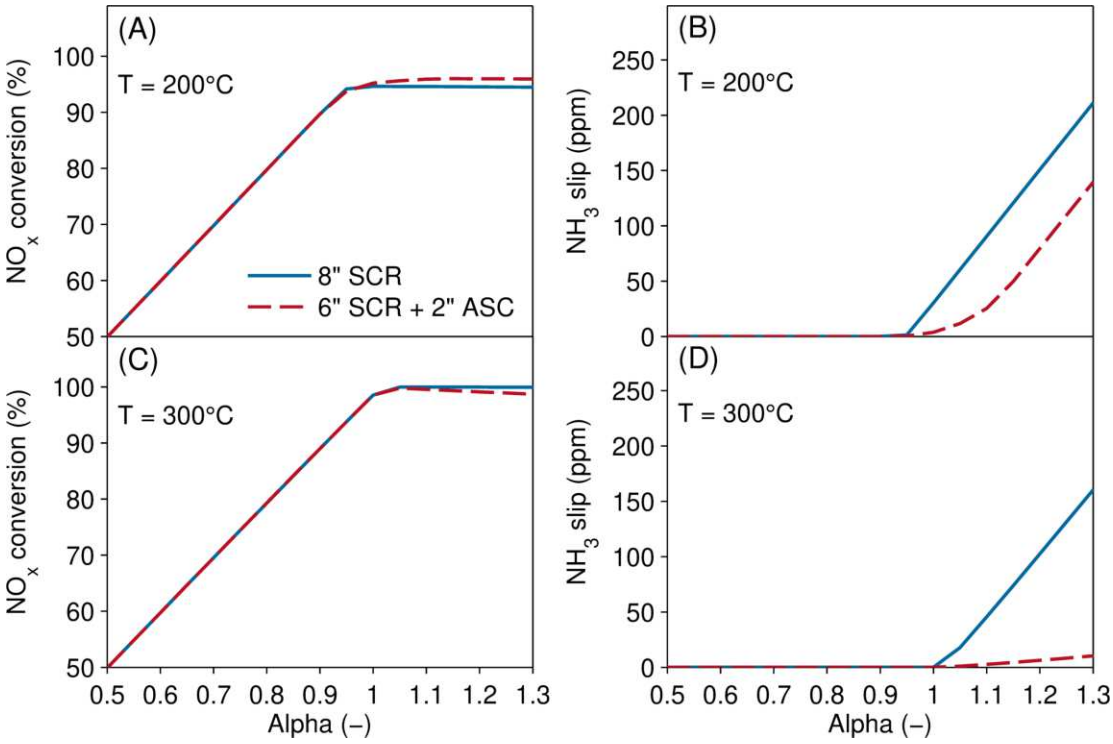

Figure 4.5 – NO_x conversion and ammonia slip for an 8" SCR and a 6" SCR with a 2" ASC zone during steady state alpha dosing simulation experiments at 200°C and 300°C. A Cu-CHA catalyst was used as the SCR washcoat for the catalyst configurations.

In short, at the given inlet conditions, it can be seen that the addition of an ASC allows for less ammonia slip and, given the availability of NO_x in the ASC, may allow for an increased deNO_x activity at low temperatures. This improved deNO_x performance at 200 °C was seen for the Fe-zeolite system, however, comes with the tradeoff of N_2O formation. Higher inlet gas temperatures (e.g., 300°C) also allowed for the SCR + ASC to achieve less ammonia slip with a possible NO_x conversion loss compared to the SCR, owing to ammonia oxidation to NO_x.

4.4.2 Response to step increase in inlet gas temperature

A temperature step simulation experiment is completed in this section to analyze and compare the system configuration's response, in particular ammonia slip breakthrough. During this simulation, a constant amount of ammonia was first added to each configuration such that both systems had the same amount of ammonia slip (10 ppm) once steady state was reached. Thereafter, a step increase in the inlet gas temperature from 200ºC to 300ºC was implemented while the ammonia supplied to the system was simultaneously cut off. As in the previous section, the inlet gas space velocity used was 30 000 h^{-1} and had a mole fraction composition of 420 ppm NO, 180 ppm NO_2, 5% O_2, and 5% H_2O. The simulation shown in this section was conducted using the Fe-zeolite SCR for the catalyst configuration; results using the Cu-CHA catalyst for the SCR washcoat are not shown but demonstrate the same benefit of an ASC. To achieve a steady state ammonia slip of 10 ppm at the specified inlet conditions using the Fe-zeolite washcoat, ammonia was added at an alpha ratio of 0.63 for the SCR and 0.72 for the SCR + ASC system.

Figure 4.6 shows the inlet gas temperature, inlet amount of ammonia, the resulting ammonia slip, and the resulting amount of NO_x gas exiting the two different catalytic converter designs over time. Before 500 s, the stationary NO_x conversion for the SCR is 60.8% and 68.4% for the SCR + ASC. A higher NO_x conversion is achieved for the SCR + ASC system because ammonia slip and NO_x exiting the 6" SCR zone is being converted to N_2O, as highlighted in Section 4.4.1. As more ammonia can be converted over this 2" ASC zone compared to the last 2" of the SCR, a higher alpha value is added to the SCR + ASC system.

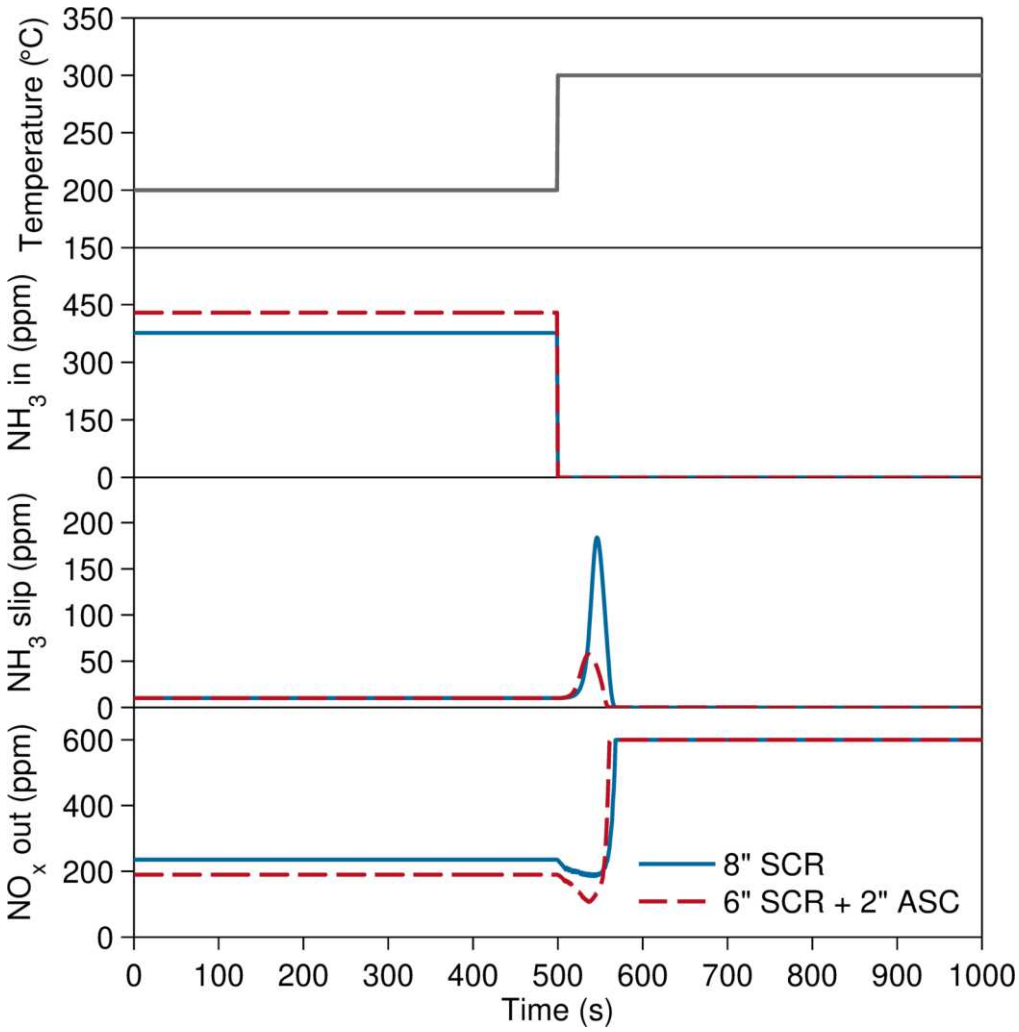

Figure 4.6 – Comparison of system response (ammonia slip, outlet NO_x) to an initial step change in temperature for an 8" SCR and a 6" SCR with a 2" ASC zone at 30 000 h^{-1}. An Fe-zeolite catalyst was used as the SCR washcoat for the catalyst configurations.

When an inlet gas temperature increase of 100ºC occurs and the ammonia supplied is simultaneously cut off, one can see through Figure 4.6 that the SCR + ASC system response results in approximately a third of the amount of ammonia slip compared to the SCR system. Less ammonia slip arises from the SCR + ASC system as the ASC-brick oxidizes the ammonia.

The same experiments were also completed at a very high space velocity (e.g., 120 000 h^{-1}), and it was observed that approximately the same amount of ammonia, or alpha values, were added to the 8" SCR as for the 6" SCR + 2" ASC. This occurred because the ASC layer is not accessible owing to the diffusion limitation in the upper SCR washcoat layer. As a result, the two catalytic converter configurations' resulting steady state NO_x conversion and the resulting ammonia slip due to the temperature step change were identical.

To summarize, in this section it is observed that the system with an ASC allows for significantly less ammonia slip compared to only an SCR, given that no external transport limitation is present. This demonstrates the ASC's ability to cushion ammonia breakthrough occurring in driving cycles owing to increases in temperature (e.g., due to acceleration).

4.4.3 Comparing optimized dosing profiles for SCR and SCR+ASC system

As seen in Section 4.4.1 and 4.4.2, the addition of an ASC behind an SCR allows for less ammonia slip compared to an SCR-only system during steady state alpha dosing tests, and during sudden increases in temperature that occur owing to increases in load during driving cycles. Since the ASC lowers the ammonia slip exiting the catalytic converter configuration, it may be possible to dose ammonia more aggressively to a catalyst system with an ASC to increase NO_x conversion, while staying below an ammonia slip constraint. Therefore, in this section, the performance of the 8" SCR and combined 6" SCR + 2" ASC system are compared using optimized dosing strategies for each configuration during a WHTC. The goal is to investigate

the benefit of the ASC addition during more realistic driving scenarios, and more specifically, whether it allows for a more aggressive ammonia dosing strategy to increase the overall NO_x conversion.

The ammonia dosing strategy was optimized to maximize the NO_x conversion over the driving cycle while maintaining the average ammonia slip across the driving cycle below 10 ppm and the maximum ammonia slip below 50 ppm. Additionally, constraints were added to ensure that ammonia could only be added to the system at any given time instant where the inlet temperature is above 180ºC, owing to the hydrolysis of urea, and that the maximum amount of ammonia that could be added at any given time instance is 4000 ppm to reflect equipment limitations. The optimization procedure is discussed in more detail in the Section 4.3 or in [13].

The analysis was first completed for the catalyst configurations using an Fe-zeolite catalyst as the SCR washcoat, with the NO_x conversions, ammonia slip values, and ammonia added during the WHTC being recorded in Table 2.1. In this table, it is seen that when one optimizes the ammonia dosing strategy for the 8" SCR, a NO_x conversion of 77.7% was achieved and the constraints are satisfied. When applying the identical SCR optimized dosing profile to a 6" SCR + 2" ASC system, such that the same amount of moles of ammonia were added at every time instant as was done for the SCR, the amount of ammonia slip from the catalytic converter system decreased to an average slip of 2.3 ppm, as the ASC's oxidation layer converted some ammonia, while the NO_x conversion stayed the same. Finally, when optimizing the ammonia dosing profile for the 6" SCR + 2" ASC it is seen that the ASC allowed for

10% more ammonia to be added to the system (5.85 mol). Despite more ammonia being added, the 6" SCR + 2" ASC only allowed for a 3% higher NO_x conversion. This slight increase is partially owing to the reaction of NO_x with ammonia to produce N_2O in the lower platinum layer (R11 and R13), but also the greater availability of ammonia in the front end of the SCR to allow for a higher NO_x conversion.

Table 4.1 – Applying ammonia dosing strategy for catalyst systems during WHTC driving cycle. An Fe-zeolite catalyst was used as the SCR washcoat for the catalyst configurations.

	Target	Opt. 8" SCR	6" SCR + 2" ASC	Opt. 6" SCR + 2" ASC
NO_x Conv. (%)	maximize	77.7	77.6	80.8
Avg. NH_3 Slip (ppm)	≤ 10	10.0	2.3	10.0
Max. NH_3 Slip (ppm)	≤ 50	35.7	18.7	50.0
Moles NH_3 Added (mol)	-	5.23	5.23	5.85

The same analysis was completed for the Cu-CHA SCR and SCR + ASC system, with the results being shown in Table 4.2. As with the Fe-zeolite catalyst system, the results demonstrate that applying the dosing profile from the 8" SCR to the 6" SCR + 2" ASC allows for less ammonia slip and a minimal decrease in NO_x conversion. This minimal decrease in NO_x conversion is owing to the oxidation of ammonia to NO_x and the consumption of ammonia in the oxidation layer, which limits its availability to react with NO_x in the SCR layer. Optimizing the ammonia dosing strategy for the

6” SCR + 2” ASC configuration allows for more aggressive ammonia dosing, with no improvement in deNO_x performance.

Table 4.2 – Applying ammonia dosing strategy for catalyst systems during WHTC driving cycle. A Cu-CHA catalyst was used as the SCR washcoat for the catalyst configurations.

	Target	Opt. 8” SCR	6” SCR + 2” ASC	Opt. 6” SCR + 2” ASC
NO_x Conv. (%)	maximize	96.0	95.7	95.5
Avg. NH_3 Slip (ppm)	≤ 10	10.0	1.6	7.4
Max. NH_3 Slip (ppm)	≤ 50	38.3	18.8	47.0
Moles NH_3 Added (mol)	-	6.69	6.69	7.37

4.4.4 Over/under-dosing

Section 4.3 showed that the SCR + ASC system allows for little to no increase in NO_x conversion compared to an SCR alone when applying individually adjusted dosing strategies to a WHTC, but did not analyze how the catalytic converter configurations behave when an error in dosing occurs. Therefore, the individually optimized dosing profile for both the 8” SCR and 6” SCR + 2” ASC system was used and a constant dosing error was introduced to the respective system’s optimized dosing profile, allowing the catalytic converter’s behaviour to be analyzed during constant under- and over-dosing of an optimized dosing profile for a given driving cycle. The effect of applying a constant dosing error to the 8” SCR and 6” SCR + 2” ASC (Fe-zeolite as SCR washcoat) on NO_x conversion and average ammonia slip is seen in Figure 4.7.

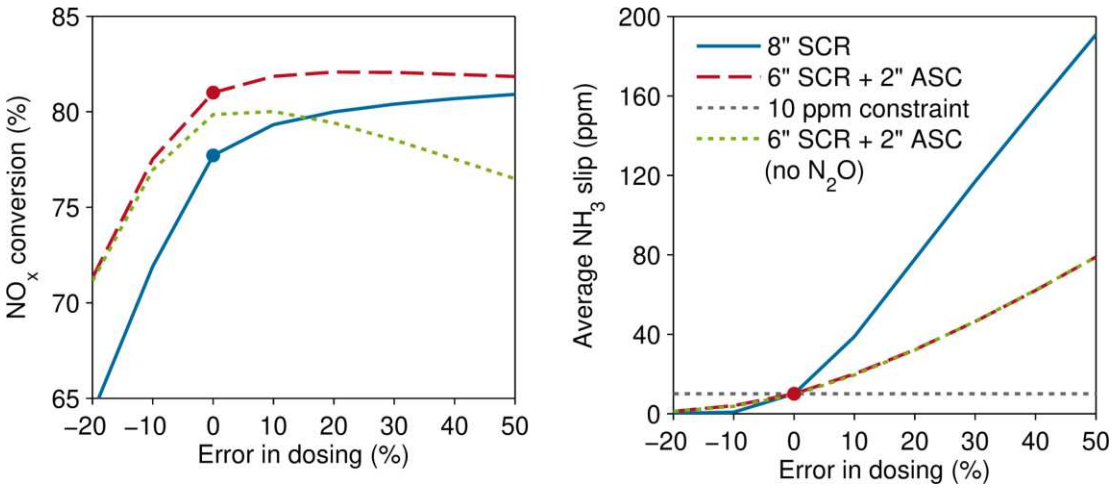

Figure 4.7 – NO_x conversion and average ammonia slip for different errors in dosing for the WHTC driving cycle. An Fe-zeolite catalyst was used as the SCR washcoat for the catalyst configurations.

The NO_x conversions and average ammonia slip values at a 0% error in dosing in Figure 4.7 represent the optimized result for the respective catalytic converter design, which was discussed in Section 4.3. When constantly under-dosing ammonia throughout the driving cycle, resulting in a negative error in dosing, the combined SCR + ASC system achieves a slightly higher ammonia slip value (Figure 4.7 - right) because more ammonia is being added to the SCR + ASC system. This results in a higher NO_x conversion for the SCR + ASC configuration (Figure 4.7 - left), as more ammonia being added to the system compared to the 8" SCR, and completely reacts with NO_x in the front-end SCR.

When constantly over-dosing ammonia, which corresponds to the positive "error in dosing" values, the NO_x conversion for the 8" SCR continues to rise noticeably and approaches the NO_x conversion of the SCR + ASC. While the SCR + ASC

demonstrates a higher NO_x conversion in the driving cycle, it is important to note that higher NO_x conversion is partially owing to N_2O formation because of R11 and R13. If this reaction were not to take place (i.e., when setting the pre-exponential factor of the N_2O formation reaction to zero), the NO_x conversion of the SCR + ASC would begin to decrease and become less than the NO_x conversion of the 8" SCR itself, owing to the ammonia oxidation to NO_x in the bottom layer of the ASC. When comparing the average ammonia slip for the two different configurations during over-dosing in Figure 4.7, one can note that significantly more ammonia slip is occurring from the 8" SCR in comparison to the 6" SCR + 2" ASC system since the ASC oxidizes the ammonia.

The performance of the SCR + ASC system when using the Cu-CHA catalyst for the SCR washcoat is shown in Figure 4.8. In this figure, it is observed that when a constant over-dosing of ammonia occurs, the ASC releases less ammonia owing to its oxidation. The NO_x conversion of the 6" SCR + 2" ASC remains minimally lower owing to the oxidation of ammonia to NO_x. During under-dosing situations, the performance of the SCR + ASC is again better than the SCR itself, since more ammonia is being added to the system and consumed.

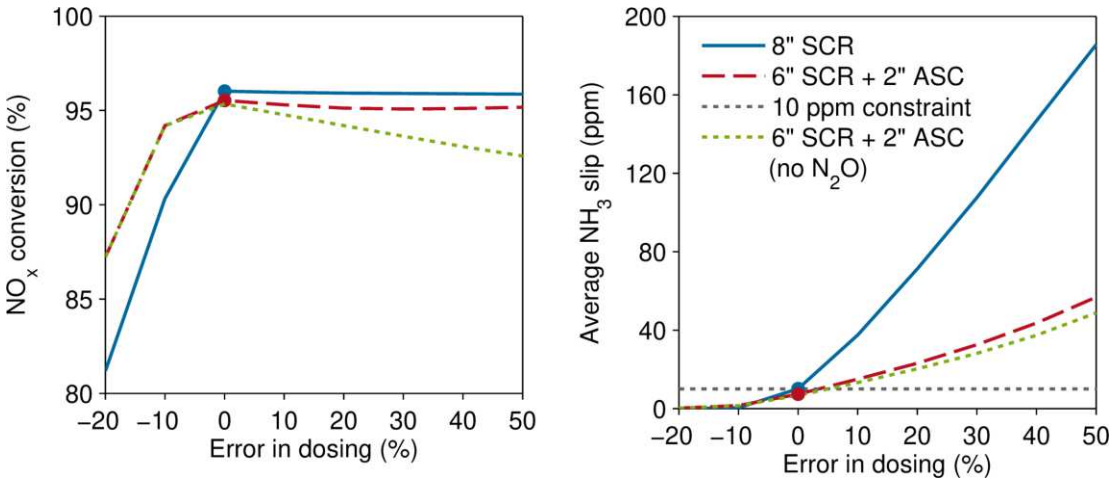

Figure 4.8 – NO_x conversion and average ammonia slip for different errors in dosing for the WHTC driving cycle. A Cu-CHA catalyst was used as the SCR washcoat for the catalyst configurations.

Finally, this analysis demonstrates the ASC's ability to offer significant security to the exhaust emission after-treatment system when an error in dosing occurs. This could be seen through its capability in maintaining the ammonia slip closer to an acceptable level when over-dosing and allowing for a higher NO_x conversion when under-dosing. The security is particularly beneficial in catalyst aging or unpredictable driving conditions when an inadequate amount of ammonia may be added and is not achieved with solely an 8" SCR.

4.4.5 Sensitivity analysis on ASC design parameters

Opitz et al. [13] demonstrated the importance of completing the design of the catalytic converter configuration and optimization of the operation strategy simultaneously. Here, two design parameters of the SCR + ASC reactor configurations, ASC length and washcoat loading of the SCR layer in the ASC, are

analyzed to observe their effect on the catalytic converter system performance. The studies are completed by optimizing the dosing strategy for each of the various catalyst configurations to allow for meaningful comparisons between the different systems.

4.4.5.1 Effect of catalyst length

To analyze the effect of the ASC's length on the SCR + ASC catalytic converter configuration performance during a given driving cycle, the ASC and SCR length were modified such that the total catalytic converter configuration had a length of 8". The dosing profile was optimized for each respective catalytic converter system under the same constraints presented in Section 4.4, that is, the 10 ppm average ammonia slip constraint, 50 ppm maximum ammonia slip constraint, and the equipment and temperature limitation. In addition to the WHTC, an ETC is used to observe the effect of the ASC length during hot operating conditions (Figure 4.2). The resulting NO_x conversion, total ammonia added, and overall cumulated N_2O emissions for each catalytic converter configuration using an Fe-zeolite catalyst for the SCR washcoat are shown in Figure 4.9.

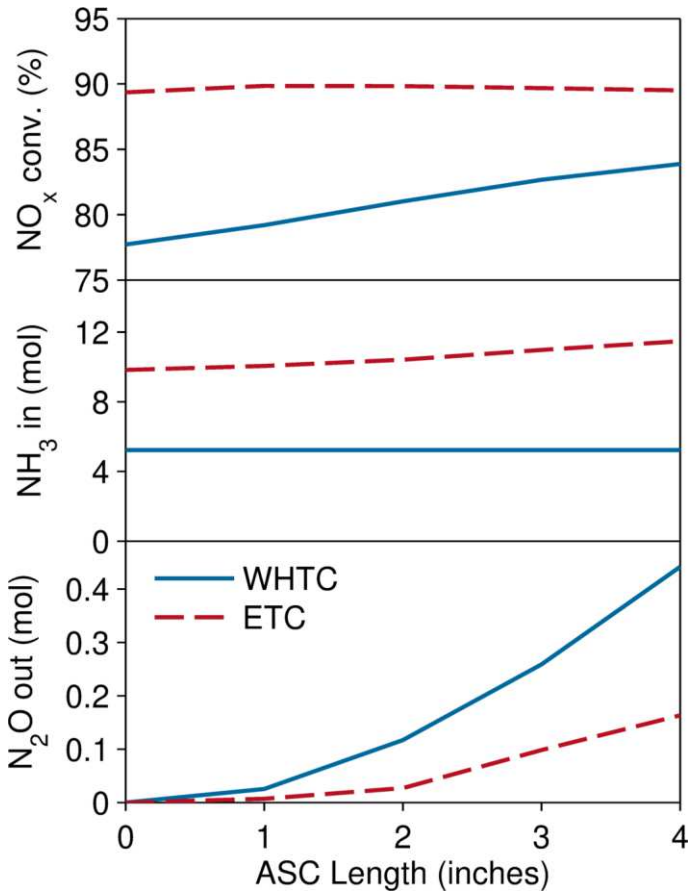

Figure 4.9 – Influence of ASC length on overall catalytic converter configuration NO_x increase during WHTC and ETC driving cycle. An Fe-zeolite catalyst was used as the SCR washcoat for the catalyst configurations.

Figure 4.9 shows that, for the WHTC driving cycle, the NO_x conversion rises with an increase in ASC length. This occurs because the longer ASC length allows for more ammonia to be added to the system, which results in more ammonia slip and NO_x exiting the shorter SCR-brick; thus, more ammonia is available to be oxidized or react with NO_x to produce N_2O in the ASC-brick's lower platinum layer. As a result, the N_2O increases significantly with ASC length. If the reaction between ammonia and NO_x to N_2O (R11 and R13) were not able to occur, the increase in NO_x conversion

during the WHTC with increase length of catalyst would be less than 1% (not shown).

Figure 4.9 also shows that there is no change in the overall NO_x conversion of the system when increasing the ASC length for the hot ETC driving cycle, despite more ammonia being added to the system. This effect can be explained by the greater selectivity for NO_x in the ASC at hot temperatures, which was discussed in Section 4.1. Owing to the hot temperature, less N_2O is also formed compared to the WHTC.

The same analysis was completed with the Cu-CHA SCR catalyst, with the results for the WHTC being shown in Figure 4.10. The results demonstrate that there is no change in NO_x conversion with the ASC length, however the N_2O formation increases owing to the greater amount of ammonia and NO_x entering the ASC earlier to allow R11 and R13 to occur, given the SCR's shorter length.

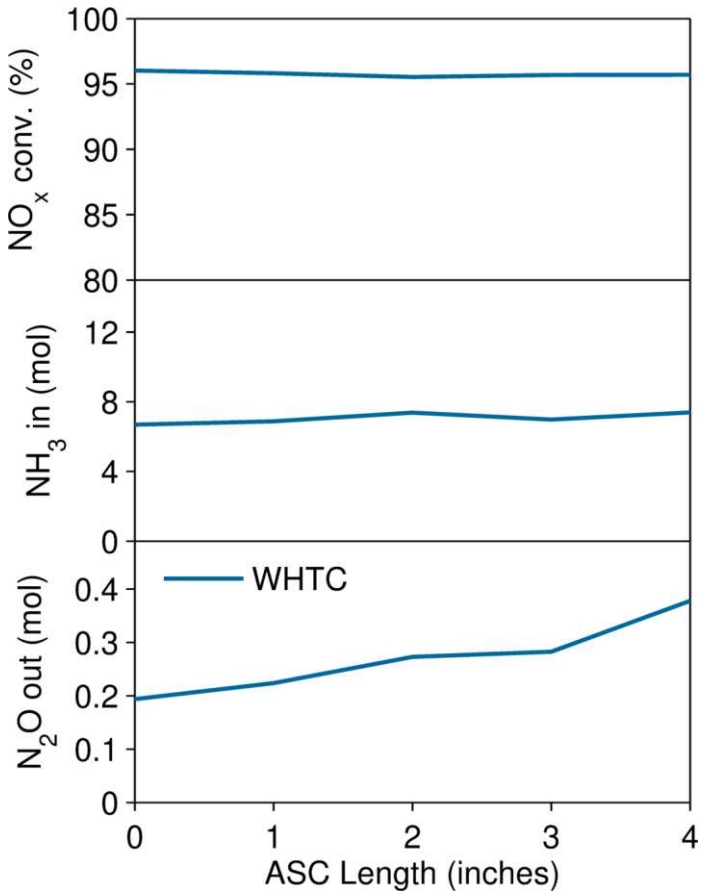

Figure 4.10 – Influence of ASC length on overall catalytic converter configuration NO_x increase during WHTC and ETC driving cycle. A Cu-CHA catalyst was used as the SCR washcoat for the catalyst configurations.

Overall, it can be seen that increasing the ASC length may result in a slightly higher NO_x conversion for the lower-temperature WHTC, however comes at the cost of significantly more N_2O formation. Given the limited change in NO_x conversion with ASC length, a shorter ASC (i.e., 1") following the SCR would suffice in providing a safety net in over and under-dosing scenarios, while limiting N_2O production.

4.4.5.2 Effect of SCR layer washcoat loading

In this subsection, a sensitivity analysis that investigates the effect of the ASC's upper-SCR layer washcoat loading on catalyst performance during the WHTC is completed. The study is performed for the 6" SCR + 2" ASC catalyst system, using the Fe-zeolite catalyst as the SCR washcoat. The washcoat loading of the ASC's upper SCR layer is varied while the washcoat (active site) density is kept constant. Therefore, as the washcoat loading decreases, the washcoat thickness decreases. The dosing strategy was optimized for each of these catalyst systems under the same constraints as for catalyst length to make meaningful comparisons.

The overall catalytic converter NO_x conversion, ammonia conversion, and N_2O production in the ASC-brick can be seen in Figure 4.11 for the different washcoat loadings of the SCR + ASC configuration. In this figure, a 100% washcoat loading for the ASC represents the original amount of the upper layer SCR washcoat used in the previous sections. The average ammonia slip and maximum ammonia slip bounded the 10 and 50 ppm constraints for all performed optimizations.

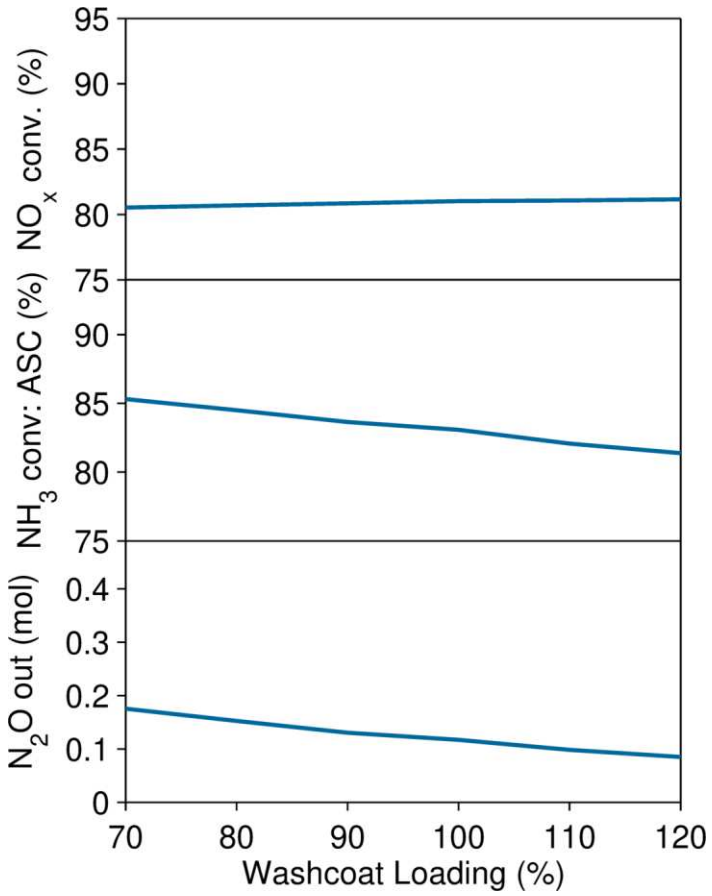

Figure 4.11 – Influence of the ASC's SCR washcoat loading on catalyst system performance. An Fe-zeolite catalyst was used as the SCR washcoat for the catalyst configurations.

The results in Figure 4.11 demonstrate that the variation in washcoat loading does not result in a change in the overall NO_x conversion. Lower SCR washcoat loadings (i.e., 70%) allow for slightly more ammonia to be added to the catalyst system (not shown) and a greater conversion of ammonia in the ASC, as there is less diffusion resistance for the ammonia to reach the lower platinum layer. As a result, more ammonia and NO_x can also react in the lower platinum layer to increase the selectivity to N_2O. Higher SCR washcoat loadings (i.e., 120%) allow for a greater diffusion resistance

for the ammonia to reach the platinum layer. Therefore, slightly less ammonia is added to the system (not shown) and the ASC has a lower ammonia conversion and N_2O production. This also means that more NO_x reacts with ammonia in the upper SCR layer to allow for the same NO_x conversion to be achieved as the ASC with the low SCR washcoat loading. This ammonia conversion and N_2O selectivity trend agrees with the work of Scheuer et al. [3], who completed a similar parameter experiment and noticed that the ammonia conversion and N_2O selectivity decreased almost linearly with an increase in washcoat loading throughout the performed ammonia oxidation steady state experiments.

Overall, through this parameter study, it can be concluded that the upper SCR washcoat loading does not influence the catalytic converter NO_x conversion performance, but lowers the selectivity for N_2O, when an individually adjusted dosing strategy with fixed ammonia slip constraints is used during the WHTC.

4.5 Conclusions

In this simulation study, an 8" SCR design and a 6" SCR + 2" ASC design was compared in terms of system performance. In particular, it was investigated whether the ASC's ability to lower ammonia slip can result in a more aggressive dosing being applied during driving cycles, to increase the overall system's NO_x conversion while staying under ammonia slip constraints. To begin the investigation, the base performance of the two catalytic converter designs (SCR versus SCR with an ASC) was investigated and compared *via* steady state tests and a system response test to a sudden increase in temperature. The results demonstrated that when the same amount

of ammonia is added to the 8" SCR or 6" SCR + 2" ASC, that the system with the ASC had a lower ammonia slip, possibly at the cost of either increased N_2O formation or lower NO_x conversion. Additionally, the ASC was able to mitigate ammonia slip much better during sudden increases in temperature, which occur in driving cycles.

Since the ASC's ability to limit ammonia slip may allow for more ammonia to be added to the catalytic converter system, in a next step, comparisons of the catalytic converter designs with optimized ammonia dosing strategies for the WHTC were completed. The ammonia dosing strategy maximized the NO_x conversion while maintaining the ammonia slip under the user-defined constraints. Interestingly, although the ASC allowed for more ammonia to be added to the catalytic converter system compared to the SCR, it did not allow for a significantly higher NO_x conversion during the WHTC (< 2% increase). However, compared to an SCR-only system, the ASC allows for significantly less ammonia slip during over-dosing scenarios, while allowing for a higher NO_x conversion during under-dosing scenarios.

Finally, a parameter study was completed to observe the effect of the ASC catalyst length and its upper-SCR washcoat loading on the overall catalytic converter system performance. Through the sensitivity analysis on ASC length, it was concluded that although a longer ASC might allow for an increase in NO_x conversion during the WHTC, a significant amount of N_2O is also produced. No change in NO_x conversion was observed when varying the ASC's upper-SCR washcoat layer, but a decrease in N_2O produced was observed with an increase in the upper-SCR washcoat loading.

Overall, it can be concluded that the ASC is a positive addition to the SCR in meeting the exhaust emission regulations. Although it does not necessarily allow for a higher NO_x conversion, its ability to cope with under and over-dosing situations can be beneficial in catalyst aging and unpredictable driving conditions.

4.6 References

[1] M. Koebel, M. Elsener, M. Kleemann, Urea-SCR: a promising technique to reduce NOx emissions from automotive diesel engines, Catalysis Today 59 (2000) 335-345.

[2] I. Nova, E. Tronconi (Eds.), Urea-SCR Technology for deNOx After Treatment of Diesel Exhausts, Springer (2014).

[3] A. Scheuer, W. Hauptmann, A. Drochner, J. Gieshoff, H. Vogel, M. Votsmeier, Dual layer automotive ammonia oxidation catalysts: Experiments and computer simulation, Applied Catalysis B: Environmental 111–112 (2012) 445-455.

[4] A. Güthenke, D. Chatterjee, M. Weibel, B. Krutzsch, P. Kočí, M. Marek, I. Nova, E. Tronconi, Current status of modeling lean exhaust gas aftertreatment catalysts, in: Guy B. Marin (Ed.), Advances in Chemical Engineering, Academic Press (2007) 103-283.

[5] A. Schuler, M. Votsmeier, P. Kiwic, J. Gieshoff, W. Hautpmann, A. Drochner, H. Vogel, NH3-SCR on Fe zeolite catalysts – From model setup to NH3 dosing, Chem. Eng. J. 154 (2009) 333-340.

[6] M. Colombo, I. Nova, E. Tronconi, V. Schmeißer, B. Bandl-Konrad, L. Zimmermann, NO/NO2/N2O-NH3 SCR reactions over a commercial Fe-zeolite catalyst for diesel exhaust aftertreatment: Intrinsic kinetics and monolith converter modelling, Appl. Cat. B 111-112 (2012) 106-118.

[7] P. Metkar, M. P. Harold, V. Balakotaiah, Experimental and kinetic modeling study of NH3-SCR of NOx on Fe-ZSM-5, Cu-chabazite and combined Fe- and Cu-zeolite monolithic catalysts, Chem. Eng. Sci. 87 (2013) 51-66.

[8] M. Bendrich, A. Scheuer, R. E. Hayes, M. Votsmeier, Unified mechanistic model for Standard SCR, Fast SCR, and NO2 SCR over a copper chabazite catalyst, Appl. Catal. B 222 (2018) 76-87.

[9] M. Colombo, I. Nova, E. Tronconi, V. Schmeißer, B. Bandl-Konrad, L. Zimmermann, Experimental and modeling study of a dual-layer (SCR + PGM) NH3 slip monolith catalyst (ASC) for automotive SCR aftertreatment systems. Part 1. Kinetics for the PGM component and analysis of SCR/PGM interactions, Applied Catalysis B: Environmental 142–143 (2013) 861-876.

[10] M. Colombo, I. Nova, E. Tronconi, V. Schmeißer, B. Bandl-Konrad, L.R. Zimmermann, Experimental and modeling study of a dual-layer (SCR + PGM) NH3 slip monolith catalyst (ASC) for automotive SCR after treatment systems. Part 2. Validation of PGM kinetics and modeling of the dual-layer ASC monolith, Applied Catalysis B: Environmental 142–143 (2013) 337-343.

[11] S. Shrestha, M.P. Harold, K. Kamasamudram, A. Yezerets, Selective oxidation of ammonia on mixed and dual-layer Fe-ZSM-5 + Pt/Al2O3 monolithic catalysts, Catalysis Today 231 (2014) 105-115.

[12] S. Shrestha, M. P. Harold, K. Kamasamudram, A. Kumar, L. Olsson, K. Leistner, Selective oxidation of ammonia to nitrogen on bi-functional Cu-SSZ-13 and Pt/Al2O3 monolith catalyst, Catal. Today 267 (2016) 130-144.

[13] B. Opitz, M. Bendrich, A. Drochner, H. Vogel, R. E. Hayes, J. F. Forbes, M. Votsmeier, Simulation study of SCR catalysts with individually adjusted ammonia dosing strategies, Chem. Eng. J. 264 (2015) 936-944.

[14] W. Hauptmann, M. Votsmeier, H. Vogel, D.G. Vlachos, Modeling the simultaneous oxidation of CO and H2 on Pt - Promoting effect of H2 on the CO-light-off, Appl. Catal., A 397 (2011) 174-182.

[15] M. Votsmeier, A. Scheuer, A. Drochner, H. Vogel, J. Gieshoff, Simulation of automotive NH3 oxidation catalysts based on pre-computed rate data from mechanistic surface kinetics, Catalysis Today 151 (2010) 271-277.

[16] J. Rink, B. Mozaffari, S. Tischer, O. Deutschmann, M. Votsmeier, Real-time Simulation of Dual-Layer Catalytic Converters Based on the Internal Mass Transfer Coefficient Approach, Topics in Catalysis 60 (2017) 225-229.

[17] S. Samuel, L. Austin, D. Morrey, Automotive test drive cycles for emission measurement and real-world emission levels - a review, Proceedings of the Institution of Mechanical Engineers, Part D: Journal of Automobile Engineering 216 (2002) 555-564.

[18] W. Hauptmann, A. Schuler, J. Gieshoff, M. Votsmeier, Modellbasierte Optimierung der Harnstoffdosierung für SCR-Katalysatoren, Chemie Ingenieur Technik 83 (2011) 1681-1687.

[19] K. Kamasamudram, C. Henry, N. Currier, A. Yezerets, N2O Formation and Mitigation in Diesel Aftertreatment Systems, SAE Int. J. Engines 5 (2012) 688 - 698.

Chapter 5 – Summary and conclusions

In this work, a surface reaction mechanism was developed in Chapter 2 by integrating various mechanistic pathways proposed in literature. The presented, dual-site mechanism captures ammonia and nitrate storage, as well the main SCR reactions (Standard SCR, Fast SCR, NO_2 SCR) and side reactions. The reaction parameters were fit to steady state and transient behaviour for a Cu-CHA catalyst, and are shown to predict the catalyst behaviour during a driving cycle, without any refitting of kinetic parameters required. Analysis of the model demonstrated a significantly higher prediction of inhibitive ammonium nitrate during low temperature, high NO_2/NO_x steady state experiments, compared to the hot WHTC. Had the model neglected nitrate storage, and only captured ammonia storage and steady state data as usually completed in literature, the NO_x conversion for the low temperature, high NO_2/NO_x steady state data would have assumed a substantial amount of inhibitive ammonium nitrate. As a result, the model would have incorrectly predicted the driving cycle NO_x conversion.

To validate whether the minimal formation of ammonium nitrate during transient driving cycles holds true, Chapter 3 used an experimental method and simulations to compare and understand the amount of ammonium nitrate stored during steady state and transient tests over the Cu-CHA catalyst. Transient step changes fluctuating between 25% and 75% NO_2/NO_x highlighted the ability to buffer the NO_x conversion when the stored ammonium nitrate deviates from its steady state value. During the step change from 25% to 75% NO_2/NO_x, the ammonium nitrate storage was below its

corresponding steady state value, resulting in more NO_x being consumed due to its storage and greater availability of active sites, owing to less ammonium nitrate inhibition. During the step change from 75% to 25% NO_2/NO_x, the ammonium nitrate storage was above the corresponding steady state value, causing the ammonium nitrate to decompose and momentarily approach the Fast SCR conversion, owing to the availability of nitrates. An analysis of the ammonium nitrate formation during consecutive cold WHTCs with a high cumulated NO_2/NO_x ratio demonstrated that little ammonium nitrate inhibits the catalyst activity owing to its slow accumulation and the rapidly fluctuating inlet conditions.

Finally, Chapter 4 applied the Cu-CHA model and an Fe-zeolite model as the SCR washcoat to investigate the benefit of an ASC during stationary tests and transient driving cycles. More specifically, it was investigated whether the addition of the ASC would allow for a more aggressive ammonia dosing strategy to be implemented during driving cycles to boost the system's NO_x conversion while satisfying user-defined ammonia slip constraints. Comparisons of the catalytic converter designs (8" SCR versus 6" SCR + 2" ASC) with the different SCR washcoats demonstrated that the ASC allows for more ammonia to be added to the catalyst system, but may only allow for a slightly higher NO_x conversion (maximum 3%), which is partially owing to the formation of undesired N_2O on the platinum layer of the ASC. However, it was highlighted that the ASC is very beneficial for over-dosing situations, as it allows for less ammonia slip breakthrough, and under-dosing situations, as it allows for a greater NO_x conversion compared to the SCR without an ASC. A parameter study on ASC length demonstrated that a longer ASC during a colder driving cycle could allow for a

higher NO_x conversion, but with the tradeoff of more N_2O production. No change in NO_x conversion, but a decrease in N_2O selectivity, was observed when increasing the upper-SCR washcoat loading.

5.1 Outlook

Following this thesis, there are still many meaningful items to be addressed. From a mechanistic standpoint, it would be interesting to investigate and extend the mechanism presented in Chapter 2 to include the redox of copper *via* NO and O_2 as well as *via* NO_2, rather than only with O_2. The mechanism could also be extended to capture the low temperature ammonia oxidation or the high temperature N_2O formation during standard SCR. Additionally, the mechanistic effects (i.e., nitrate storage) could be investigated and the reaction mechanism could be implemented for the vanadium and Fe-zeolite catalyst. The importance of these effects on the catalysts' activity during driving cycles should be investigated.

To follow-up the ammonium nitrate study in Chapter 3, it would be beneficial to complete catalyst characterization experiments (i.e., DRIFTS) on the Cu-CHA catalyst and its zeolite. This would help understand the active sites and reaction mechanisms for ammonium nitrate formation, as well as the resulting N_2O decomposition dynamics, which may assist in describing less transient, cold driving cycles, where ammonium nitrate may play more of a role (i.e., for a bulldozer).

Finally, the implemented dosing strategy for the SCR + ASC configuration used for the simulation study in Chapter 4 should be validated *via* its implementation at a transient test bench. Factors that could lead to varying results from the simulation

study include the table's dependence on surface coverage and the sensitive desorption dynamics of the ammonia towards the end of the WHTC.

Bibliography

H. Klingenberg, Automobile Exhaust Emission Testing, Springer (1996).

S. Solomon, D. Qin, M. Manning, Z. Chen, M. Marquis, K. B. Averyt, M. Tignor, H. L. Miller (Eds.), Climate Change 2007: The Physical Science Basis, Cambridge University Press (2007).

J. L. Sullivan, R. E. Baker, R. H. Hammerle, T. E. Kennex, L. Muniz, T. J. Wallington, 2004. CO2 emission benefit of diesel (versus gasoline) powered vehicles. Environmental Science & Technology 38, 3217 – 3223.

T.J. Wallington, C.K. Lambert, W.C. Ruona, Diesel vehicles and sustainable mobility in the U.S., Energy Policy 54 (2013) 47-53.

I. Nova, E. Tronconi (Eds.), Urea-SCR Technology for deNOx After Treatment of Diesel Exhausts, Springer (2014).

A. Scheuer, W. Hauptmann, A. Drochner, J. Gieshoff, H. Vogel, M. Votsmeier, Dual layer automotive ammonia oxidation catalysts: Experiments and computer simulation, Appl. Catal. B 111–112 (2012) 445-455.

J. Jansson, Vanadia-Based Catalysts for Mobile SCR in Urea-SCR Technology for deNOx After Treatment of Diesel Exhausts, Springer (2014) 65-96.

M. P. Harold, P. Metkar, Lean NOx Reduction by NH3 on Fe-Exchanged Zeolite and Layered Fe/Cu Zeolite Catalysts: Mechanisms, Kinetics, and Transport Effects

in Urea-SCR Technology for deNOx After Treatment of Diesel Exhausts, Springer (2014) 311-356.

M. Colombo, I. Nova, E. Tronconi, A comparative study of the NH3-SCR reactions over a Cu-zeolite and a Fe-zeolite catalyst, Catal. Today 151 (2010) 223-230.

F. Gao, J. H. Kwak, J. Szanyi, C. H. F. Peden, Current Understanding of Cu-Exchanged Chabazite Molecular Sieves for Use as Commercial Diesel Engine DeNOx Catalysts, Top. Catal. 56 (2013) 1441-1459.

H.-Y. Chen, Z. Wei, M. Kollar, F. Gao, Y. Wang, J. Szanyi, C. H. F. Peden, A comparative study of N2O formation during the selective catalytic reduction of NOx with NH3 on zeolite supported Cu catalysts, J. Catal. 329 (2015) 490-498.

S. A. Bates, A. A. Verma, C. Paolucci, A. A. Parekh, T. Anggara, A. Yezerets, W. F. Schneider, J. T. Miller, W. N. Delgass, F. H. Ribeiro, Identification of the active Cu site in standard selective catalytic reduction with ammonia on Cu-SSZ-13, J. Catal. 312 (2014) 87-97.

J.-S. McEwen, T. Anggara, W.F. Schneider, V.F. Kispersky, J.T. Miller, W.N. Delgass, F.H. Ribeiro, Integrated operando X-ray absorption and DFT characterization of Cu-SSZ-13 exchange sites during the selective catalytic reduction of NOx with NH3, Catal. Today 184 (2012) 129-144.

F. Gao, E. D. Walter, M. Kollar, Y. Wang, J. Szanyi, C. H. F. Peden, Understanding ammonia selective catalytic reduction kinetics over Cu/SSZ-13 from motion of Cu ions, J. Catal. 319 (2014) 1-14.

F. Gao, D. Mei, Y. Wang, J. Szanyi, C. H. F. Peden, Selective Catalytic Reduction over Cu/SSZ-13: Linking Homo- and Heterogeneous Catalysis, J. Am. Chem. Soc. 139 (2017) 4935-4942.

C. Paolucci, I. Khurana, A. Parekh, S. Li, A. J. Shih, H. Li, J. R. Di Orio, J. D. Albarracin-Caballero, A. Yezerets, J. T. Miller, W. N. Delgass, F. H. Ribeiro, W. F. Schneider, R. Gounder, Dynamic multinuclear sites formed by mobilized copper ions in NOx selective catalytic reduction, Science 357 (2017) 898-903.

H. Zhu, J. H. Kwak, C. H. F. Peden, J. Szanyi, In situ DRIFTS-MS studies on the oxidation of adsorbed NH3 by NOx over a Cu-SSZ-13 zeolite, Catal. Today 205 (2013) 16–23.

I. Lezcano-Gonzalez, U. Deka, B. Arstad, A. Van Yperen-De Deyne, K. Hemelsoet, M. Waroquier, V. Van Speybroeck, B. M. Weckhuysen, A. M. Beale, Determining the storage, availability, and reactivity of NH3 within Cu-Chabazite-based Ammonia Selective Catalytic Reduction systems, Phys. Chem. Chem. Phys. 16 (2014) 1639–1650.

T. V. W. Janssens, H. Falsig, L. F. Lundegaard, P. N. R. Vennestrom, S. B. Rasmussen, P. G. Moses, F. Giordanino, E. Borfecchia, K. A. Lomachenko, C. Lamberti, S. Bordiga, A. Godiksen, S. Mossin, P. Beato, A Consistent Reaction Scheme for the Selective Catalytic Reduction of Nitrogen Oxides with Ammonia, ACS Catal. 5 (2015) 2832-2845.

M. P. Ruggeri, T. Selleri, M. Colombo, I. Nova, E. Tronconi, Identification of nitrites/HONO as primary products of NO oxidation over Fe-ZSM-5 and their role in the Standard SCR mechanism: A chemical trapping study, J. Catal. 311 (2014) 266-270.

A. M. Beale, F. Gao, I. Lezcano-Gonzalez, C. H. F. Peden, J. Szanyi, Recent advances in automotive catalysts for NOx emission control by small-pore microporous materials, Chem. Soc. Rev. 44 (2015) 7371.

M. P. Ruggeri, A. Grossale, I. Nova, E. Tronconi, H. Jirglova, Z. Sobalik, FTIR in situ mechanistic study of the NH3-NO/NO2 "Fast SCR" reaction over a commercial Fe-ZSM-5 catalyst, Cat. Today 184 (2012) 107-114.

M. Colombo, I. Nova, E. Tronconi, Detailed kinetic modeling of the NH3-NO/NO2 SCR reactions over a commercial Cu-zeolite catalyst for Diesel exhausts after treatment, Catal. Today 197 (2012) 243-255.

A. Güthenke, D. Chatterjee, M. Weibel, B. Krutzsch, P. Kočí, M. Marek, I. Nova, E. Tronconi, Current status of modeling lean exhaust gas aftertreatment catalysts, in: Guy B. Marin (Ed.), Advances in Chemical Engineering, Academic Press (2007) 103-283.

I. Nova, D. Bounechada, R. Maestri, E. Tronconi, Influence of the Substrate Properties on the Performances of NH3-SCR Monolithic Catalysts for the Aftertreatment of Diesel Exhaust: An Experimental and Modeling Study, Ind. Eng. Chem. Res. 50 (2011) 299-309.

P. Metkar, M. P. Harold, V. Balakotaiah, Experimental and kinetic modeling study of NH3-SCR of NOx on Fe-ZSM-5, Cu-chabazite and combined Fe- and Cu-zeolite monolithic catalysts, Chem. Eng. Sci. 87 (2013) 51-66.

B. Shakya, M. P. Harold, V. Balakotaiah, Simulations and optimization of combined Fe- and Cu-zeolite SCR monolith catalysts, Chem. Eng. J. 278 (2015) 374-384.

B. Opitz, M. Bendrich, A. Drochner, H. Vogel, R. E. Hayes, J. F. Forbes, M. Votsmeier, Simulation study of SCR catalysts with individually adjusted ammonia dosing strategies, Chem. Eng. J. 264 (2015) 936-944.

L. Olsson, K. Wijayanti, K. Leistner, A. Kumar, S. Y. Joshi, K. Kamasamudram, N. W. Currier, A. Yezerets, A multi-site kinetic model for NH3-SCR over Cu/SSZ-13, Appl. Cat. B 174-175 (2015) 212-224.

Y. Zha, Cummins Sustained Low Temperature NOx Reduction, https://energy.gov/sites/prod/files/2016/06/f33/pm068_zha_2016_o_web.pdf.

M. Bendrich, A Systematic Approach for Performance Comparisons of NO_x Converter Designs, University of Alberta Thesis (2014).

M. Koebel, M. Elsener, M. Kleeman, Urea-SCR: a promising technique to reduce NOx emissions from automotive diesel engines, Catal. Today 59 (2000) 335-345.

A. Schuler, M. Votsmeier, P. Kiwic, J. Gieshoff, W. Hautpmann, A. Drochner, H. Vogel, NH3-SCR on Fe zeolite catalysts -- From model setup to NH3 dosing, Chem Eng. J. 154 (2009) 333-340.

M. Colombo, I. Nova, E. Tronconi, NO2 adsorption on Fe- and Cu-zeolite catalysts: The effect of the catalyst red-ox state, Appl.Cat. B 111-112 (2012) 433-444.

D. W. Fickel, E. D'Addio, J. A. Lauterbach, R. F. Lobo, The ammonia selective catalytic reduction activity of copper-exchanged small-pore zeolites, Appl Catal. B 102 (2011) 441-448.

A. A. Verma, S. A. Bates, T. Anggara, C. Paolucci, A. A. Parekh, K. Kamasamudram, A. Yezerets, J. T. Miller, W. N. Delgass, W. F. Schneider, F. H. Ribeiro, NO oxidation: A probe reaction on Cu-SSZ-13, J. Catal. 312 (2014), 179-190.

S. Brandenberger, O. Kroecher, A. Tissler, R. Althoff, P. D. Schettler, The State of the Art in Selective Catalytic Reduction of NOx by Ammonia Using Metal-Exchanged Zeolite Catalysts Catalysis Reviews, Sci. Eng. 50 (2008) 492-531.

M. P. Ruggeri, I. Nova, E. Tronconi, J. A. Pihl, T. J. Toops, W. P. Partridge, In-situ DRIFTS measurements for the mechanistic study of NO oxidation over a commercial Cu-CHA catalyst, Appl. Catal. B 166-167 (2015) 181-192.

M. P. Ruggeri, T. Selleri, I. Nova, E. Tronconi, J. A. Pihl, T. J. Toops, W. P. Partridge, New Mechanistic Insights in the NH3-SCR Reactions at Low Temperature, Top. Catal. 59 (2016) 907-912.

J. H. Kwak, J. H. Lee, S. D. Burton, A. S. Lipton, C. H. F. Peden, J. Szanyi, A Common Intermediate for N2 Formation in Enzymes and Zeolites: Side-On Cu-Nitrosyl Complexes, Angew. Chem. Int. Ed. 52 (2013) 9985-9989.

C. Paolucci, A. A. Verma, S. A. Bates, V. F. Kispersky, J. T. Miller, R. Gounder, W. N. Delgass, F. H. Ribeiro, W. F. Schneider, Isolation of the Copper Redox Steps in the Standard Selective Catalytic Reduction of Cu-SSZ-13, Angew. Chem. Int. Ed. 53 (2014) 11828-11833.

T. Guenter and H. W. P. Carvalho and D. E. Doronkin and T. Sheppard and F. Glatzel and A. J. Atkins and J. Rudolph and C. R. Jacob and M. Casapu and J.-D. Grunwaldt, Structural snapshots of the SCR reaction mechanism on Cu-SSZ-13, Chem. Commun. 51 (2015) 9227-9230.

A. Grossale, I. Nova, E. Tronconi, D. Chatterjee, M. Weibel, The chemistry of the NO/NO2-NH3 “fast” SCR reaction over Fe-ZSM5 investigated by transient reaction analysis, J. Catal. 256 (2008) 312-322.

A. Grossale, I. Nova, E. Tronconi, Role of Nitrate Species in the “NO2 SCR” Mechanism over a Commercial Fe-zeolite Catalyst for SCR Mobile Applications, Catal. Lett. 130 (2009) 525-531.

E. Tronconi, P. Forzatti, Adequacy of lumped parameter models for SCR reactors with monolith structure, AlChE J. 38 (1992) 201-210.

K. E. Brenan, S. L. Campbell, L. R. Petzold, Numerical Solution of Initial-value Problems in Differential-algebraic Equations, Elsevier Science Publishing Co. (1989).

A. Grossale, I. Nova, E. Tronconi, Study of a Fe–zeolite-based system as NH3-SCR catalyst for diesel exhaust aftertreatment, Catal. Today 136 (2008) 18-27.

A. Grossale, I. Nova, E. Tronconi, Ammonia blocking of the ‘‘Fast SCR” reactivity over a commercial Fe-zeolite catalyst for Diesel exhaust aftertreatment, J. Catal. 265 (2009) 141-147.

F. Gao, E. D. Walter, E. M. Karp, J. Luo, R. G. Tonkyn, J. H. Kwak, J. Szanyi, C. H.F. Peden, Structure-activity relationships in NH3-SCR over Cu-SSZ-13 as probed by reaction kinetics and EPR studies, J. Catal. 300 (2013) 20-29.

L. Arnarson, H. Falsig, S. B. Rasmussen, J. V. Lauritsen, P. G. Moses, A complete reaction mechanism for standard and fast selective catalytic reduction of nitrogen oxides on low coverage VOx/TiO2(001) catalysts, J. Catal. 346 (2017) 188-197.

K. Hadjiivanov, J. Saussey, J. L. Freysz, J. C. Lavalley, FT-IR study of NO + O2 co-adsorption on H-ZSM-5: reassignment of the 2133 cm-1 band to NO+ species, Cat. Lett. 52 (1998) 103-108.

J. A. Loiland, R. F. Lobo, Oxidation of zeolite acid sites in NO/O2 mixtures and the catalytic properties of the new site in NO oxidation, J. Catal. 325 (2015) 68-78.

M. Bendrich, A. Scheuer, R. E. Hayes, M. Votsmeier, Unified mechanistic model for Standard SCR, Fast SCR, and NO2 SCR over a copper chabazite catalyst, Appl. Catal. B 222 (2018) 76-87.

L. Xie, F. Liu, K. Liu, X. Shi, H. He, Inhibitory effect of NO2 on the selective catalytic reduction of NOx with NH3 over one-pot synthesized Cu-SSZ-13 catalyst, Catal. Sci. Technol. 4 (2014) 1104.

J. Luo, Y. Tang, S. Joshi, K. Kamasamudram, N. Currier, A. Yezerets, The Impact of Ammonium Nitrate Species on Low Temperature NOx Conversion Over Cu/CHA SCR Catalyst, SAE Technical Paper, 2017-01-0953.

Ruggeri, M. P., J. Luo, I. Nova, E. Tronconi, K. Kamasamudram, A. Yezerts, Novel method of ammonium nitrate quantification in SCR catalysts, Catal. Today 307 (2017) 48-54.

N. Ottinger, Y. Xi, C. Keturakis, Z. G. Liu, Impact of Hydrothermal Aging on the Formation and Decomposition of Ammonium Nitrate on a Cu/Zeolite SCR Catalyst, SAE Technical Paper, 2017-01-0946.

F. Marchitti, E. Barker Hemings, I. Nova, P. Forzatti, E. Tronconi, Enhancing the Low-T NH3-SCR Activity of a Commmerical Fe-Zeolite Catalyst by NH4NO3 Dosing: an Experimental and Modeling Study, Emiss. Control Sci. Technol. 2 (2016) 1-9.

F. Adam, J. Schoenhaber, A. Wagner, Synthetic Gas Bench (SGB) Tests Simulating Real and Dynamic Driving Conditions: A New and Cost Attractive Method for TWC Evaluation, SAE Technical Paper, 2015-01-1066.

M. Colombo, I. Nova, E. Tronconi, V. Schmeißer, B. Bandl-Konrad, L. Zimmermann, NO/NO2/N2O-NH3 SCR reactions over a commercial Fe-zeolite catalyst for diesel exhaust aftertreatment: Intrinsic kinetics and monolith converter modelling, Appl. Cat. B 111-112 (2012) 106-118.

M. Colombo, I. Nova, E. Tronconi, V. Schmeißer, B. Bandl-Konrad, L. Zimmermann, Experimental and modeling study of a dual-layer (SCR + PGM) NH3 slip monolith catalyst (ASC) for automotive SCR aftertreatment systems. Part 1. Kinetics for the PGM component and analysis of SCR/PGM interactions, Applied Catalysis B: Environmental 142–143 (2013) 861-876.

M. Colombo, I. Nova, E. Tronconi, V. Schmeißer, B. Bandl-Konrad, L.R. Zimmermann, Experimental and modeling study of a dual-layer (SCR + PGM) NH3 slip monolith catalyst (ASC) for automotive SCR after treatment systems. Part 2. Validation of PGM kinetics and modeling of the dual-layer ASC monolith, Applied Catalysis B: Environmental 142–143 (2013) 337-343.

S. Shrestha, M.P. Harold, K. Kamasamudram, A. Yezerets, Selective oxidation of ammonia on mixed and dual-layer Fe-ZSM-5 + Pt/Al2O3 monolithic catalysts, Catalysis Today 231 (2014) 105-115.

S. Shrestha, M. P. Harold, K. Kamasamudram, A. Kumar, L. Olsson, K. Leistner, Selective oxidation of ammonia to nitrogen on bi-functional Cu-SSZ-13 and Pt/Al2O3 monolith catalyst, Catal. Today 267 (2016) 130-144.

W. Hauptmann, M. Votsmeier, H. Vogel, D.G. Vlachos, Modeling the simultaneous oxidation of CO and H2 on Pt - Promoting effect of H2 on the CO-light-off, Appl. Catal., A 397 (2011) 174-182.

M. Votsmeier, A. Scheuer, A. Drochner, H. Vogel, J. Gieshoff, Simulation of automotive NH3 oxidation catalysts based on pre-computed rate data from mechanistic surface kinetics, Catalysis Today 151 (2010) 271-277.

J. Rink, B. Mozaffari, S. Tischer, O. Deutschmann, M. Votsmeier, Real-time Simulation of Dual-Layer Catalytic Converters Based on the Internal Mass Transfer Coefficient Approach, Topics in Catalysis 60 (2017) 225-229.

S. Samuel, L. Austin, D. Morrey, Automotive test drive cycles for emission measurement and real-world emission levels - a review, Proceedings of the Institution of Mechanical Engineers, Part D: Journal of Automobile Engineering 216 (2002) 555-564.

W. Hauptmann, A. Schuler, J. Gieshoff, M. Votsmeier, Modellbasierte Optimierung der Harnstoffdosierung für SCR-Katalysatoren, Chemie Ingenieur Technik 83 (2011) 1681-1687.

K. Kamasamudram, C. Henry, N. Currier, A. Yezerets, N2O Formation and Mitigation in Diesel Aftertreatment Systems, SAE Int. J. Engines 5 (2012) 688 - 698.

Appendix A – Supplementary material for Chapter 3

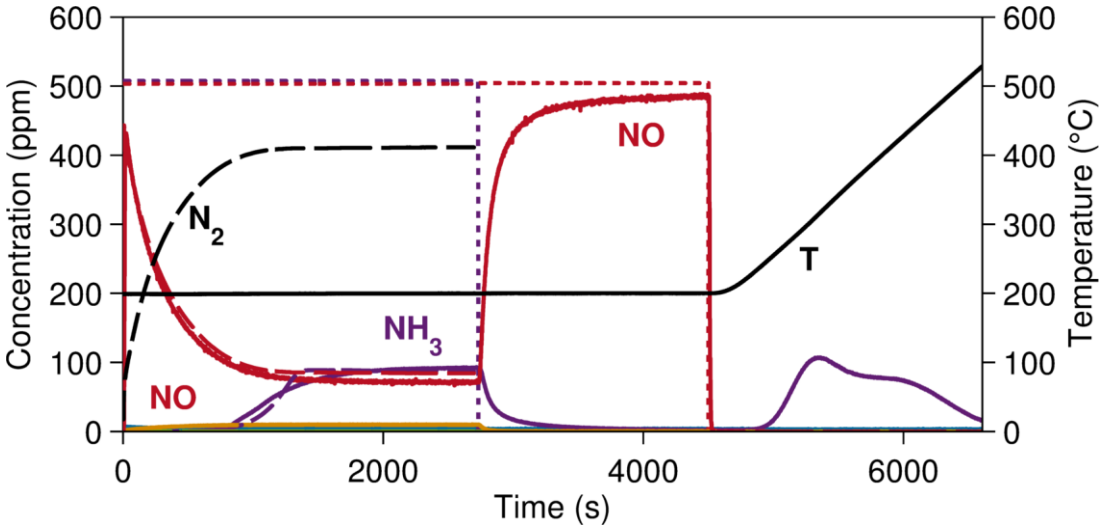

Figure S3.1 – Ammonium nitrate quantification experiment for a feed (dotted lines) of 500 ppm NH_3 and NO_x, NO_2/ NO_x = 0%, 5% H_2O, 6% O_2, and N_2 balance gas; GHSV at STP = 50,000 h^{-1}. Experimental outlet shown by solid lines.

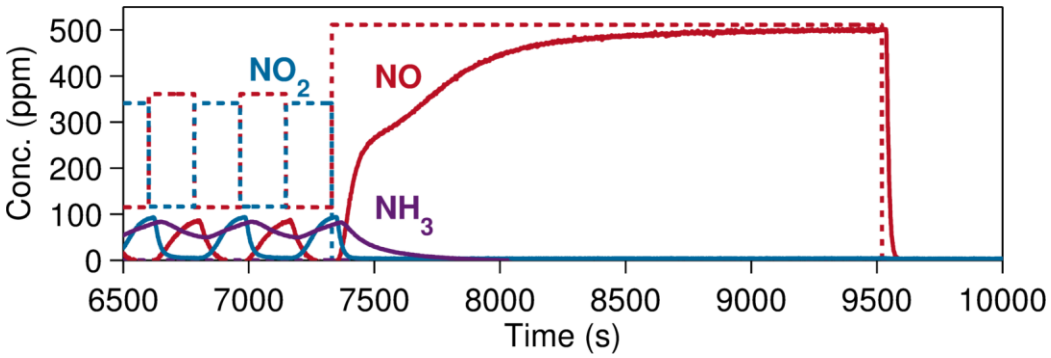

Figure S3.2 – Ammonium nitrate quantification experiment following the 75% NO_2/NO_x step change for the 3-minute step change experiment shown in Figure 5. Dotted lines represent feed setpoint whereas solid lines represent experimental output. Experiment conducted at 200 °C.

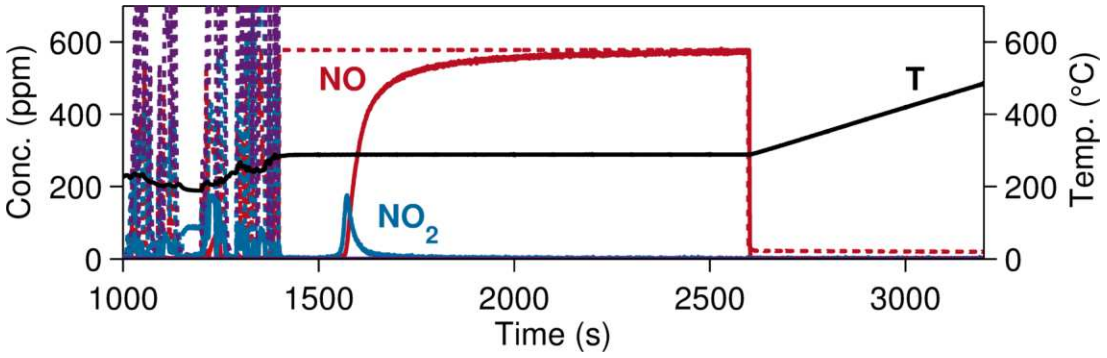

Figure S3.3 – Ammonium nitrate quantification experiment following 1400 s of the 1st cold 70% NO_2/NO_x WHTC shown in Figure 7. The dotted lines represent feed setpoint whereas the solid lines represent experimental output.